Design and Simulation of a New Generation Radiation Detector for Oil and Gas Exploration

Aliyu Bala

PhD

University of York

Physics

May 2021

Abstract

Radiation detection is extensively used in borehole logging — a technique widely employed in oil and gas, and mineral exploration. The workhorse of this detection application for many years has been traditional ^{3}He tubes in neutron porosity tool and NaI:Tl scintillators coupled with photomultiplier tube (PMT) in γ ray density tool. Although PMTs are a well proven technology which can operate in the high temperature conditions (typically of order 100℃) and pressures (10 MPa) encountered during logging activities, they are however fragile and have a large form factor and require a high-voltage power supply thereby occupying significant space within the borehole probe. However, to survey for oil and gas, γ ray density and neutron porosity tools must be used conjointly. Additionally, the demand for neutron detection technology is increasing while the supply of ^{3}He gas is extremely scarce. These issues have led to the characterisation of an alternative dual radiation detection technology based on ^{6}Li (GS20), which could replace ^{3}He tube and NaI:Tl crystal respectively. We have shown that GS20 is capable of measuring both electron density and hydrogen content, eliminating the need for two separate tools. Furthermore, we have evaluated CsI:Tl scintillators coupled to standard 6×6 mm^2 SiPMs from Hamamatsu and SensL as a function of temperature as an alternative to NaI:Tl scintillator coupled to PMT. In addition, we have shown that these prototypes operate effectively up to a temperature of 80℃ which could satisfy the requirements of some applications of borehole logging where the maximum temperature encountered is 75℃

Acknowledgements

"Feeling gratitude and not expressing it is like wrapping a present and not giving it." -William Arthur Ward.

Glory be to God almighty for giving me the ability and strength to get to this point. I want to express my gratitude and appreciation to the Petroleum Technology Development Fund (PTDF) and the Federal Republic of Nigeria at large for fully funding my PhD program at the University of York. A special thanks to my employer, Usmanu Danfodiyo University Sokoto for granting my study leave/fellowship.

My kind and sincere thanks goes to my PhD supervisor, Professor David Jenkins who has not only supported me academically, but has serves as a guardian who always listens to me and advise me accordingly. I will not forget to mention Dr Pankaj Joshi who was always there in the lab when I needed his help. It is not enough to say thanks to Dr Jamie R. Brown who has always sacrifice time to discuss problems relating to experiment and analysis. I also want to give a special gratitude and appreciation to Dr Julien Bordes, Dr Vahid Esmaeili Sani and Professor John Allison for their vast knowledge of Geant4 they shared with me.

Sincere appreciation to Paul Worthington and Robertson Geologging Company at large for sharing their expertise and allowing me to use their equipment and also hosting me for a 2 weeks placement to understand the principle and techniques used in nuclear well logging.

My appreciation also goes to all my colleagues in the Nuclear Physics group especially Dr Luke Morris for his continues support, Dr Rubena Binti Yusoff, Dr Faten A. Alsomali

and Rehab Yajzey for their encouragement and prayers.

Finally, my immeasurable appreciation goes to my parents, my eldest brother Dr Bala Bakwai, my other brothers and sisters, my beloved wife Bilqisu Idris Ibrahim, my second wife to be Sumayya Hussaini Waziri for their enormous prayers. Mr Surajo Namadi, Mr Sulaiman Ogunsina, Mr Ayuba Yusuf Lawal, Mr Aliyu Usman Abubakar, Flying Officer Abdulhamid Abubakar, Flying Officer Musa Muhammad and all other well wishers, thank you all for your support in your own ways.

Declaration

I hereby declare that this thesis is the result of my own work. The research here presented was carried out at the University of York between November 2017 and April 2021. Part of this research is the product of discussions with my research supervisor Professor David Jenkins, Dr Jamie Brown, Dr Pankaj Joshi, Dr Julien Bordes, Professor John Allison, Engr Paul Worthington from Robertson Geologging Company, Llandudno, Wales, UK.

Experiments, methods and ideas if not otherwise stated, originate from discussions, meetings with my research supervisor Professor David Jenkins.

As outlined in a later section (achievements), some part of this thesis have been published in the following journal articles and international conference proceedings:

- A. Bala, J.R. Brown, D.G. Jenkins and P. Joshi. "***Operation of scintillators and SiPMs at high temperatures and their application for borehole logging***" Nuclear Instruments and Methods Research Section A. February 2021. https://www.sciencedirect.com/science/article/pii/S0168900221001455

- A. Bala, J.R. Brown, D.G. Jenkins, P. Joshi and P. Worthington. "***Monte Carlo Comparison of Alternatives to He Thermal Neutron Detectors for Logging Applications***"
  In proceedings of the 2019 IEEE Nuclear Science Symposium and Medical Imaging Conference (NSS/MIC) Manchester, United Kingdom.
  https://ieeexplore.ieee.org/document/9059978

Date ..... Signature of candidate .....

I Professor David Jenkins, hereby certify that the candidate has fulfilled the requirements and regulations appropriate for the degree of Doctor of Philosophy at the University of York and that the candidate is fit to submit this research thesis for that degree in the University.

Date ..... Signature of Supervisor .....

How to read this thesis

This thesis is involves computer simulations and experiment. It is structured into six (6) chapters and an appendix. The first chapter provide the reader with some information to understand the basics, mechanisms and principle of of well logging. The motivations behind the project are also highlighted.

Chapter two (2) provides the background knowledge relevant to the research topic. The mechanisms through which neutrons and gamma-rays interact with matter are also presented in this chapter. Furthermore, the detection mechanism of slow and fast neutrons are presented. Finally, a detailed description and review of neutron detectors are also presented within this chapter.

Chapter three (3) discusses the Monte Carlo simulation software (GEANT4) used in the simulation part of research. An overview of the software is presented and a follow on how information can can be extracted out of it. A comparison is made between GS20 crystal and the conventional thermal neutron detector (^{3}He tube) as used in well logging activities within a logging tool. The results obtained are also presented. Part of it has already been publish in an international conference proceedings while the other part of it is also presented in a journal article which is ready for submission as at the time of submitting this thesis. Lastly a summary is provided to wrap up everything within the chapter.

Since this research involves the search for an alternative radiation detector that can serve dual purpose, chapter four (4) demonstrated how the pulses generated due to neutron and gamma-ray events can be differentiated using a pulse shape discrimination analysis

method. An overview of other pulse shape discrimination methods are also described and lastly a summary to wrap up the chapter.

As high is one limiting factor which needs to be overcome by any alternative detection system, more so light output is another important feature a detector should have since it decreases with temperature. Chapter five (5) compares the light output of different crystals and high temperature optimisation of CsI:Na doped coupled to silicon photomultiplier (SiPM). Results obtained are presented and discussed, which has also been published to Nuclear Instrument and Method Research: Section A. A summary and conclusion is presented at the end of this chapter. The appendix shows a copy of the published papers.

Achievements

Journal articles

- A. Bala, J.R. Brown, D.G. Jenkins and P. Joshi. "***Operation of scintillators and SiPMs at high temperatures and their application for borehole logging***" Nuclear Instruments and Methods Research Section A. February 2021. https://www.sciencedirect.com/science/article/pii/S0168900221001455

Conference proceedings

- A. Bala, J.R. Brown, D.G. Jenkins, P. Joshi and P. Worthington. "***Monte Carlo Comparison of Alternatives to 3He Thermal Neutron Detectors for Logging Applications***"
  In proceedings of the 2019 IEEE Nuclear Science Symposium and Medical Imaging Conference (NSS/MIC) Manchester, United Kingdom.
  https://ieeexplore.ieee.org/document/9059978

International conference contributions

- IEEE NSS MIC 2019, Nuclear Science Symposium and Medical Imaging Conference. Manchester, United Kingdom. 26 Oct - 02 Nov 2019.
  Poster Presentation: "*Comparison of Alternatives to 3He Thermal Neutron Detectors for Logging Applications*"

- Virtual IEEE NSS MIC 2020, Nuclear Science Symposium and Medical Imaging Conference. Buston, USA. 31 Oct - 07 Nov 2019.

  Oral Presentation: " *Monte Carlo approach to determine formation porosity and elemental composition using a GS20 crystal*"

  Poster Presentation: " *Operation of scintillators and SiPMs at high temperatures and their application for borehole logging*"

Local conference contribution

- University of York Physics Postgraduate Conference. York, United Kingdom. 20 - 21 September 2018.

  Poster Presentation: "*Design and Simulation of a New Generation Neutron Detector for Oil and Gas Exploration.*"

Workshops and short-courses

- International Workshop on Position Sensitive Neutron Detectors.
  Forschungszentrum Jülich GmbH, Germany. 15 - 17 May 2018.

- Geant4 training workshop.
  Department of Physics, University of Manchester, United Kingdom. 17 - 19 June 2019.

- Geant4 and ROOT training workshop.
  Department of Physics, University of York, United Kingdom. 10 - 15 June 2019.

- Machine Learning and Neuromorphic Computing in Nuclear Science.
  Virtual 2020 IEEE Nuclear Science Symposium and Medical Imaging Conference 31 Oct. – 7 Nov. 2020.

- Radiation Detection and Measurements.
  2019 IEEE Nuclear Science Symposium and Medical Imaging Conference Manchester, United Kingdom. 26 Oct – 02 Nov. 2019.

Contents

List of Tables

List of Figures

Chapter 1

Introduction

1.1 Background

The origin and science of well logging can be traced back to 1927 when Conrad Schlumberger measured the resistivity of the earth in a surface exploration application [1]. Generally, well logging refers to the characterisation of the subsurface rock formation using a measurement device (logging tool) in the well bore. The applications of borehole logging are invaluable to a large and diverse range of industries. For example, a petrophysicist sees it as a means to evaluate the hydrocarbon production potential of a reservoir, whereas to a geologist, it is a mapping technique for exploring the subsurface rock formation. Furthermore, a geophysicist and a reservoir engineer sees it as a source of data for surface seismic analysis and a way to get values for use in a reservoir modelling.

The choice of a logging prove depends on the intended purpose and the logging environment. Some of these tools are passive measurement devices (wireline logging) while others are active (logging while drilling). In passive measurements (wireline logging) technique, information is acquired after the borehole is drilled while the information is acquired as the borehole is being drilled in the case of active measurements (logging while drilling). Logging probes are commonly grouped into three categories: the lithology logs such as γ-ray logs, neutron-gamma logs, spontaneous potential logs; porosity logs such as neutron

porosity log, density logs, acoustic log; and resistivity logs such as electrode logs, induction logs.

Nuclear logging includes any technique that can either detect the presence of unstable isotopes, or that creates such isotopes in the logging environment. Nuclear logs are unique due to the penetrating capability of the particles and photons which makes them suitable for both cased or open boreholes. Moreover, they can be used regardless of the type of fluid in the borehole. Typical nuclear well logging measurements include but not limited to:

- Neutron porosity measurements
- Natural γ ray measurement
- γ ray density measurement
- Prompt γ ray neutron activation analysis (PGNAA)
- Prompt inelastic neutron activation analysis (PINAA)
- Delayed γ ray neutron activation analysis (DGNAA)
- Neutron porosity tool- A tool used for porosity measurement in order to estimate the amount of hydrocarbons available in the rock formation. This method is based on the interaction of fast neutrons with the nuclei present in the rock formation. The tool consist of a fast neutron source (AmBe, PuBe, ^{252}Cf, and PNG neutron source) and two ^{3}He thermal neutron detectors placed at two different position away from the neutron source [2–4]. The emitted fast neutrons penetrates the rock formation surrounding the borehole where the tool is used. The fast neutrons undergo scattering (elastic and inelastic) from nuclei of different elements in the rock formation. The thermal neutron flux will be dependent on the materials composition, in terms of it's isotopic abundances and density of the rock formation. These parameters will determine the rate of energy transfer and kinematics for inelastic scattering interactions of neutron with the rock formation. Nuclei with low mass numbers are most

effective for the slowing down of fast neutrons. Due to the conservation of energy and momentum, the reduction of neutron velocity takes place by transfer of energy to a material present in the rock formation. The energy transfer is much higher with hydrogen atoms due to mass similarity and therefore slows down fast neutrons in fewer interaction to thermal energies.

Measuring the neutron slowing down along the tool axes provide information about the fluid content (porosity) or hydrogen concentration in the rock formation as depicted in Figure 1.1. The measured concentration translates to the presence of water, hydrocarbons or other hydrogen rich materials like coal.

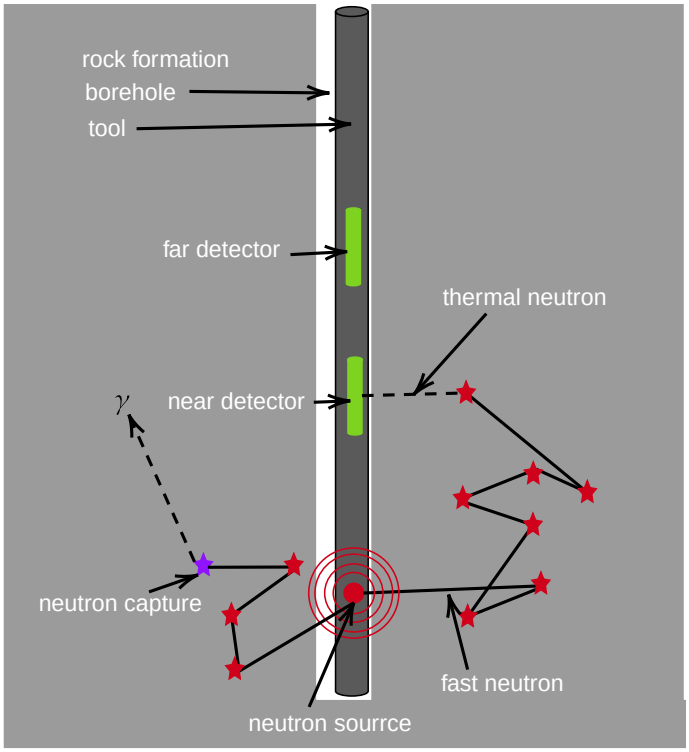

Figure 1.1: Schematic diagram of a logging tool inside an infinite volume of rock formation

^{3}He tubes are the conventional thermal neutron detectors used in neutron porosity tool for thermal neutron detection in well logging application, this is because of its tolerance to very high temperature, very high thermal neutron detection efficiency,

mechanically robust and reliability [5]. These advantages makes it the preferred choice to meet neutron porosity measurement requirements. Despite all the great advantages, ^{3}He gas which is the filled gas used in the detector has been depleting over the last two decades. Since 2008, the supply of this gas has come under strict control when it was realised that the supply was limited. It is produced as a byproduct from the decay of tritium used to maintain the nuclear stockpiles in the U.S and Russia [6]. It is cost inefficient to produce tritium just for generating ^{3}He gas with the estimated cost of ^{3}He production by making new tritium between $11 k - $18 k/liter [7].

- Neutron-γ-ray tool- The prompt production of γ rays as a result of the thermal neutron capture reaction (n,γ) and inelastic scattering (n,n$^{'}$ γ) by nuclei in the rock formation are the basis for prompt neutron activation and prompt inelastic neutron activation analysis respectively. The tool consist of a fast neutron source but with γ-ray detectors instead of neutron detectors as in the case of neutron porosity tool. As the emitted fast neutrons undergoes several elastic scattering, they can excite the nuclei present in the rock formation, which subsequently de-excite by emitting a characteristic γ rays. After several collisions, the fast neutrons lose a lot of energy and form a cloud of thermal neutrons. These low energy neutrons are absorbed by the nuclei present and a characteristic γ ray is emitted, these can be detected by a high resolution γ-ray detector to produce a spectrum. This type of measurement provides information about the lithology of the rock formation under investigation. A study of this type of tool is presented in [8].

- γ-ray tool- This technique does not require a dedicated radiation source, it relies on γ ray detection from naturally occurring sources to characterise the rock formation. It identifies the high energy γ ray peak from the decay of ^{40}K and a few gamma ray peaks from the daughter products of uranium and thorium which are well separated. This information helps to differentiate between shale and non-shale region.

- Density (γ-γ) tool- This tool consist of a γ ray source, usually ^{137}Cs and one or more γ-

ray detectors, commonly used is the NaI:Tl scintillator. The emitted γ rays enters the rock formation and interacts with the electrons in the atoms of the material present in the rock formation. When a γ ray undergo Compton scattering, it loses energy in a step-wise manner. The probability of Compton scattering is directly proportional to the electron density of the scattering material present in the rock formation. Photo-electric effect is also possible with the atomic electrons when the γ ray energy is below 0.5 MeV. The measured γ rays in both detectors is therefore attenuated by the rock formation, and the amount of attenuation depends on the density of the electrons present in the rock formation. A low γ ray count rate is recorded in rock formation with high bulk density which has a high density of electrons. Whereas, rock formation with low bulk density and hence low electron density attenuates the γ ray less thereby providing high count rate. The porosity of the rock formation, the density of the fluids in the pore space and the type of solid minerals determines the bulk density of the rock formation. Hence, the density tool is therefore useful in providing information about the porosity, evaluation of low density fluids and somewhat an aid to elemental identification.

1.2 Project Motivation

Currently, all logging tools designed to provide both neutron and γ ray detection capability in the oil and gas industry contain multiple radiation detectors, i.e. ^{3}He tubes and NaI:Tl crystals. Due to the very high cost associated with logging activity, there is a desire by the industry to significantly reduce logging cost but maintaining the performance of the logging tool. Any logging tool utilising single radioactive source and one type of radiation detection technology that is a capable of providing neutron and γ ray information will be advantageous as compared to the triple combo[1].

[1]A tool that acquires most of the basic petrophysical and lithological logs (density, porosity, and resistivity). This contains a neutron source, neutron detectors, γ ray source, γ-ray detectors, resistivity logs (induction logs and electrode logs

^{3}He gas has been the most popular material for the construction of high efficiency neutron detectors for this application, national security and safeguards [9], neutron scattering science [10], nuclear waste repositories, medical neutron imaging, nuclear physics research among others since it becomes available in large quantities in 1980s [11]. The scarcity of ^{3}He gas in conjunction to the high demand for neutron detection systems in the above mentioned applications has mandated the search for alternative thermal neutron detection technologies [6]. The thermal neutrons reaction cross-section of ^{3}He gas is 5330 barn averaged over the thermal range. Any candidate competing to replace it should therefore have a comparable thermal neutron reaction cross-section. ^{6}Li and ^{10}B are the two neutron converting materials that have received significant attention due to their thermal neutron reaction cross-section of 940 and 3840 barn respectively. The lower reaction cross-sections of ^{6}Li and ^{10}B as compared to that of the conventional gas (^{3}He gas) is compensated by their large reaction Q values.

Boreholes can be several hundred metres to a few kilometres deep, yet only ∼10 cm wide. At these depths, temperatures in excess of 100 ℃ and pressures of 10 MPa are typical, hence the instrumentation used in borehole logging must be able to operate satisfactorily in this environment, meet the strict form-factor requirements, as well as to be sufficiently robust. Therefore, not all detectors types and converting material are suitable for borehole logging applications.

From the boron family, BF_3 (boron trifluoride) tubes [12] are a direct replacement of ^{3}He tubes. However, BF_3 gas is toxic unlike ^{3}He gas, and therefore is not very suitable within high pressure environments. ^{10}B lined proportional counters [13, 14] have overcome the toxicity problem as other non-toxic noble gases are used instead. This technology also has a drawback that only one out of the two charged particles created in the neutron absorption reaction enters the active proportional gas region due to their trajectories from momentum conservation. More recently, hexagonal boron nitride (h-BN) [15] and ^{10}B nanoparticle aerosol [16] have also been developed. In ^{10}B nanoparticle aerosols, B_4C particles are dispersed in the proportional gas, thereby directly replacing the conventional ^{3}He tube with no toxicity and avoiding partial energy deposition. The most promising lithium-

based alternatives are from scintillation detectors. The first lithium-based detector to be used for logging application were ^{6}Li-loaded glass scintillators [17–21]. GS20, a class of ^{6}Li-loaded glass scintillator has been reported to be suitable for the downhole neutron porosity tools due to its ability to withstand high temperature and high shock environments [22]. It can provide neutron γ ray discrimination between temperatures of 150℃-175℃. Other lithium based detection technologies include the elpasolites family: CLLB, CLLBC and CLYC. These detectors are known for their very good energy resolution, high scintillation light yield and fast decay times. A detailed description, review and physics of detectors that utilise one of these converting materials is presented later in Chapter 2.

Neutron porosity tool relies solely on neutron scattering reactions to measure the thermal neutrons that backscattered to the detectors. As explained above and illustrated in Figure 1.1, after many collisions, the thermal neutrons are absorbed and a characteristic γ ray is released by the absorbing nuclei upon de-excitation. However, not all the fast neutrons get moderated to thermal energy range, some epithermal neutrons often get back to the detectors and these epithermal neutrons go mostly undetected due to their lower interaction cross sections. Moreover, the emitted fast neutrons from the neutron source are also accompanied by high energy γ rays. These high energy γ rays interact with the rock formation through pair production, a process that strongly depends on the atomic number of the interacting material. Pair production is most probable interaction mechanism for high energy, but Compton and P.E are still possible but very unlikely. Since ^{3}He tubes are only sensitive to thermal neutrons, therefore this information is not utilised when neutron porosity tools are used to assess the fluid content of a rock formation.

Due to the very high cost associated with logging activity, a degree of reliability and efficiency is required for any logging system. A dual mode neutron-γ-ray scintillator can be used in place of a ^{3}He tube in neutron porosity tools and also as a replacement to NaI:Tl crystals used for γ ray detection in density and neutron-γ-ray tools.

The standard photo sensor that is used in the oil and gas industry is the photomultiplier tube (PMT). This photo sensor type is highly suitable for the borehole logging application and is widely used in many industrial and scientific applications. This is because of its

ruggedness and ability to detect radiation intensities of up to single photon [23]. However, in terms of borehole logging, it does have specific disadvantages. The restrictive dimensions of boreholes constrains the form factor requirements of the logging tool and it is common for several instruments (not necessarily radiation detection-related) to be mounted within the probe. PMT's themselves occupy significant space and require bulky high voltage power supplies. Due to the small form factor requirement, the active area of the detector is restricted and therefore so is its detection efficiency. An alternative photosensor which is more compact would be of high interest to this application. An alternative photosensor which is more compact would be of high interest in this application. An attractive replacement technology consists of silicon photomultipliers (SiPMs). These devices have been revolutionary in medical imaging applications [24–28] and are finding wider application in experimental nuclear physics as well as related societal applications. SiPMs are robust and have a small form factor. Unlike PMTs, they do not need a high voltage. In recent years, a number of manufacturers have made advances in this technology resulting in higher gain, lower Dark-Count-Rate (DCR), reduced cross-talk and after-pulsing, as well as reduced temperature sensitivity. These devices now present the possibility of creating a new generation of compact, low-voltage detectors for the borehole logging application.

1.3 Project Goal

The goal of this research was to design and simulate a new generation dual radiation detection system for the use in the oil and gas industry for exploration activities as depicted Figure 1.1. Specific goals are summarised below:

- Investigation of the feasibility of a dual neutron-γ ray detection technology to replace the conventional neutron detector (^{3}He tube) and γ-ray detector (NaI:Tl) crystal as used in the logging industry. This detector technology should:
  - have similar or better thermal neutron counting efficiency as compared to ^{3}He tube.

  - have a good γ ray energy resolution
  - be rugged enough to withstand the very high temperature and pressure in comparison to the conventional detectors (^{3}He tube and NaI:Tl crystal).
  - have a reasonable form factor to allow space for other devices within the logging tool.
  - have a good Figure of Merit in neutron-γ ray discrimination capability since the detector will be sensitive to both particles.
  - be commercially available and cost effective.

- Characterise the existing diagnostic technique using epithermal neutrons and high energy γ rays.
- To characterise an alternative photo sensor (SiPM) to PMT's in borehole logging application.

The entire research presented in this thesis is motivated by the scarcity of ^{3}He gas and the high demand for neutron detection systems in many applications. Moreover, surveying for the presence of hydrocarbons requires the use of multiple logging tools. In these regards, the use of dual neutron-γ-ray detector in a logging tool turns out to be the alternative for the ^{3}He scarcity and the need to use different tools for neutron and γ ray measurements in the oil and gas industries. Ideas and methods presented in this research work combine nuclear techniques for oil and gas and nuclear physics experiments.

Chapter 2

Fundamentals of Radiation Detection

Radiations are generally categorised into ionizing and non-ionizing radiations. Of interest to this research are the ionizing radiations which includes neutrons, γ rays, X-rays, alpha and beta particles. All these types of ionizing radiations are caused by unstable atoms with excess mass or energy (or both). They carry sufficient energy to cause ionization whenever they pass through a medium. Ionizing radiations are further categorised into charged radiation such as alpha, beta and proton, and uncharge radiations like the neutrons, γ rays and X-rays. These uncharged radiations are further classified according to their energies. Whilst the γ rays are classified as low and high energy γ rays, the neutrons are classified as ultracold, cold, slow (thermal, epithermal and resonant), intermediate, fast and superfast, the energy range will be presented later in this chapter. High energy γ rays, low energy γ rays, thermal neutrons, epithermal neutrons and fast neutrons are particular importance in borehole logging applications. This chapter focuses on nuclear techniques and physics of radiation interaction with matter.

2.1 Interaction of Neutrons with Matter

Neutrons are sub-atomic particles with no net charge and has a mass of 939.565 MeV/c^2 or 1.008 u. Neutrons and protons collectively make up the nucleus of an atom. While a

bound neutron in a nucleus is stable, a free unbound neutron is unstable and undergoes beta decay into a proton.

The nuclear force is responsible for all of the processes of neutron interactions with matter. Charged particles are produced when neutrons transfer their kinetic energy to the interaction medium through scattering or absorption.

2.1.1 Scattering Reactions

This occurs when a neutron collides with the nucleus of the target material and changes its path with less energy. This collision can be elastic or inelastic depending on whether or not the total kinetic energy of the system is conserved after the collision.

2.1.1.1 Neutron Elastic Scattering

Neutrons can undergo elastic scattering with surrounding nuclei at any kinetic energy range. When a neutron undergoes an elastic collision with a nuclide, it loses some of it's kinetic energy to the nuclide. Both the neutron and the target nuclide rebound with speeds different from their original speed, thereby making the kinetic energies before and after collision different. This mode of reaction plays a very important role in slowing down fast neutrons to thermal kinetic energy level. Neutrons can transfer energy upon elastic scattering with a nuclei sufficient enough to cause ionization as illustrated in Figure 2.1. The energy gained by the nucleus is given by [29]:

$$E_A = E_n \left[\frac{4A}{(A+1)^2} \right] cos^2\theta, \tag{2.1}$$

where E_A is the energy of the nuclei with atomic mass A and E_n is the energy of the neutron, assuming that the initial nucleus is at rest, that both the neutron and proton has equal mass and that the binding energy of the nuclei is neglected.

A nuclei with atomic mass A equals to 1, will receives and energy that correspond to:

$$E_A = E_n cos^2\theta \tag{2.2}$$

For a frontal collision, where θ is 0^o, the energy of the nucleus with mass A = 1 is the incoming neutron energy:

$$E_A = E_n \tag{2.3}$$

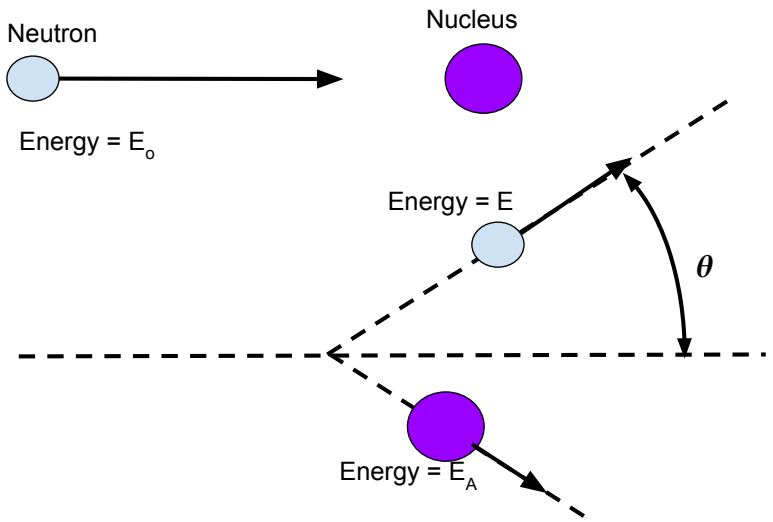

Figure 2.1: Neutron scattering and energy loss.

When fast neutrons are introduced into a medium, they undergo both elastic and inelastic collisions. During each elastic collision they are deflected through an angle, and subsequently lose energy. As each neutron travels in a unique path, a statistical approach is required to quantify their average energy loss per interaction, given by:

$$\Delta E = \frac{1}{2}(1-\alpha)E \tag{2.4}$$

where α is the collision parameter which depends on the atomic mass:

$$\alpha = \left(\frac{A-1}{A+1}\right)^2 \tag{2.5}$$

2.1.1.2 Neutron Inelastic Scattering

Another form of neutron scattering is the inelastic neutron scattering. This process occurs when the energy of an incoming neutron is absorbed by a nucleus and remains in an excited

state. While momentum is conserved, the kinetic energy of the system is not conserved. When the compound nucleus gives up it's excitation energy and returns back to it's ground state, one or more gamma rays are emitted. The average energy loss of inelastic neutron scattering depends on the energy levels found within the target nucleus. It is therefore, unlike the elastic scattering, very difficult to write the expression for the average energy loss. In a summary, the energy of the first excited state of the target nuclei decreases as a function of mass number. This type of scattering reaction is very important in the logging industry for elemental identification as will be seen in Chapter 3.

2.1.1.3 Radiative Capture Reaction

In this type of reaction, the incident neutron is completely absorbed by the target nucleus and a compound nucleus is formed. The produced compound nucleus decays back to it's ground state and one or more gamma rays are emitted. The probability of this reaction to occur strongly depends on the energy of the incident neutron as well as the temperature of the target, and the process can happen at all incoming neutron energy. Like the inelastic neutron scattering reaction, this type of reaction is also very useful for elemental identification.

2.1.1.4 Charge Exchange Reaction

Except for fast neutron detectors, all other neutron detectors operate based on this type of reaction mechanism. The neutrons interact with the converting material in the detector, resulting in a compound nucleus which end up breaking into two parts. For thermal neutrons, the energies are almost negligible as compared to the total reaction Q value, and therefore both the target nucleus and the neutron are considered to be at rest. The two decay products then emitted in opposite directions due to momentum conservation.

The probability of any of these mechanisms happening depend on the energy as well as on the type of material the neutron is interacting with.

Table 2.1: Classification of neutrons according to their energy groups [29].

Neutron Groups	**Energy, eV**
Ultracold	$< 10^{-7}$
Cold	$10^{-7} - 10^{-4}$
Slow (thermal, epithermal, resonant etc.)	$10^{-4} - 1$
Intermediate	$1 - 10^{4}$
Fast	$10^{4} - 10^{6}$
Superfast	$> 10^{6}$

2.1.2 Energy Classification of Neutrons

The binding energy of neutrons in a nuclei is some MeV, as a result are produced with high energies. However, most applications uses low energy neutrons because of their high detection efficiency. Table 2.1 shows how neutrons are grouped according to their energies.

These categories allows for the optimisation of detector designs for neutron detection. Since their designs can vary significantly for the detection of thermal neutrons compared to fast neutrons. The groups of neutron energies important to this work are fast, thermal and epithermal energy regime.

2.1.3 Neutron Reaction Cross Section

The microscopic cross section (σ) is a measure of the probability for a given reaction to occur between two particles. Cross sections are measured in units of barns, where 1 barn corresponds to 10^{-24} cm^2, a unit with dimension analogous to that of area. In other words, it is the area of an atomic nucleus which is exposed to a particular type of reaction. In the case of neutrons, cross section are classified into scattering and absorption cross sections. The total neutron scattering cross section is the sum of the elastic and inelastic scattering cross sections:

$$\sigma_s = \sigma_e + \sigma_i \tag{2.6}$$

While absorption cross section takes into account the contributions of all the individual absorption reactions (fission, radiative capture, charge exchange reaction, neutron producing reactions):

$$\sigma_a = \sigma_f + \sigma_\gamma + ... \tag{2.7}$$

The cross section for neutron absorption in any given material depends greatly on the target isotope as well as on the neutron kinetic energy. A thermal neutron energy of 0.0253 eV corresponds to a neutron velocity of 2200 m/s, which is the most probable speed of a neutron in thermal equilibrium at room temperature. [30].

Contribution from both the scattering and absorption cross sections leads to the total cross section:

$$\sigma_t = \sigma_s + \sigma_a. \tag{2.8}$$

Multiplying the microscopic cross section (σ) by the total number of nuclei N per cm^3 in a given volume, leads to macroscopic cross section (Σ):

$$\Sigma = N\sigma. \tag{2.9}$$

This quantity has a dimension of inverse length (cm^{-1}). It describes the probability per unit path length for a given reaction type. The total macroscopic cross section, which describes all the possible contribution is expressed as:

$$\Sigma_t = \Sigma_s + \Sigma_a + ... \tag{2.10}$$

2.2 Neutron Detection

As explained above, neutrons do not directly ionize the medium they traverse, their detection then is only possible through nuclear reactions with nuclei where the neutron produces secondary radiation (charged particles or photons) that are detectable by means of various sensors. The choice of detector depends on the neutron energy, the intended application and the characteristics of the neutron source use. Detailed explanations on neutron from μeV to GeV is available in the literature, see for example [31] and the references therein.

2.2.1 Gas-Filled Detectors

Gas-filled detectors operate based on ionisation of gas molecules within the detector by an incoming radiation. When an incoming particle ionises the gas, ion pairs are produced. These ions are charged particles, the are therefore collected by two electrodes (anode and cathode). The amount of ions produced is proportional to the energy of the incoming particle and the amount of voltage applied to the electrodes. It also depends on the pressure as well as the type of gas in the detector. The applied voltage causes the positive ions to drift towards the cathode while the negative electrons drift towards the anode, as can be seen in Figure 2.2.

When the applied voltage is very low, the ion pairs may combine together before reaching the electrodes due to low acceleration, and eventually form back the original molecule. If this happens, a region known as region of recombination (region A) is created as shown in Figure 2.3. As the voltage is increased, the measured current will be almost constant and only the ion pairs produced by the incoming radiation is collected by the electrodes. This region is referred to as the saturation region (region B). Increasing the voltage even higher will make the produced ion pairs accelerates towards the electrodes with high velocity, thereby causing further ionisation (secondary ionisation). The measured current will therefore arise from the contribution of both the primary and the secondary ion pairs, a region referred to as proportional region (region C). The process is referred to as gas amplification, which can be of the order of 10^6 depending on the detector and the type of incident particle.

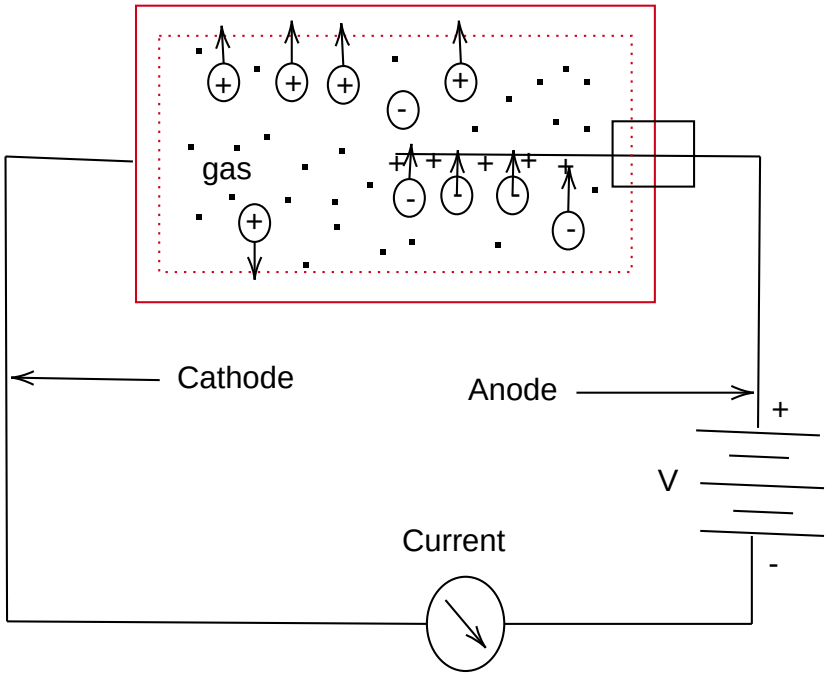

Figure 2.2: A neutron captured by ^{3}He gas produces an energetic triton and proton that are emitted in opposite directions and ionizes the gas, thereby producing free electron-ion-pairs.

Further increases in the applied voltage, regardless of the type of incoming particle, the produced current tends to be identical and a region of limited proportionality is approached (region D). Any further increase in voltage will result to identical current produced irrespective of the type of incoming particle. This region is referred to as the Geiger region (region E). In this region, ultraviolet light is produced when highly accelerated electrons strike the anode electrode, this eventually causes further emission of photoelectrons which will also strike the anode and lead to avalanche multiplication up to 10^{10}. Beyond the Geiger voltage, a region of continuous discharge (region F) is attained. In this region, one

event can lead to multiple repetitive discharge due to secondary electrons irrespective of the particle type. At this voltage, the gas may ionised even in the absence of incoming radiation.

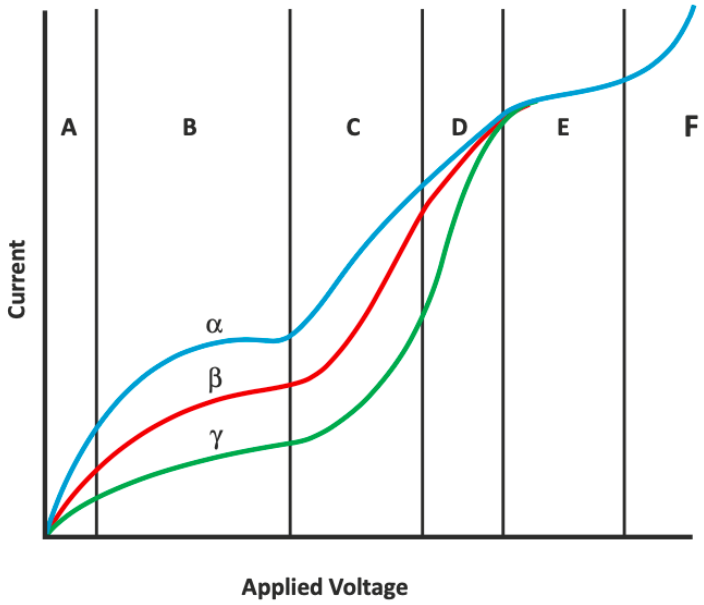

Figure 2.3: A composite curve illustrating the current output as a result of increasing voltages for different radiations. **A** Region of recombination, **B** region of saturation, **C** proportional region, **D** region of limited proportionality, **E** Geiger region, and **F** continuous discharge [32].

2.2.2 Scintillator Detectors

The use of scintillators to measure the light produced by ionizing radiation is one of the oldest techniques, which can be traced back to 1903 by Crookes [33]. This is because the scintillation process remains the most useful methods available for the detection of radiation. For any scintillation material to be considered as an ideal scintillator, it has to have the following properties as summarised by [33]:

- It should convert the kinetic energy of charged particles into detectable light with a high scintillation efficiency.

- The scintillation light yield should be linear with radiation energy over the range of interest.
- The medium should be transparent to the wavelength of its own emission.
- The decay time of the induced luminescence should be short so that fast signal pulses can be generated.
- The material should have good optical quality for it to be possible to manufacture to the required dimensions and shape.
- Its index of refraction should be near that of glass ($\sim$1.5) to permit efficient coupling of the scintillation light to a photomultiplier tube or other light sensor.
- They also need to be compounds that have stable properties over time.

There is no ideal scintillating material since no single material posses all of the above mentioned characteristics. The selection of the appropriate scintillator material has to be based on compromise, depending on the desired purpose.

The kind of detector used depends on the particles to be observed, whether electrons, gamma rays, neutrons, ions such as fission fragments. It also depends on the energy of the particles to be detected and on the radiation environment in which the detector is to be used

2.2.2.1 Organic Scintillators

In organic scintillators, the process of fluorescence originates from the transition of energy levels from a single molecule and hence the physical state of the system plays no role in the process [33]. This is to the contrary to inorganic scintillators in which a crystalline lattice is required to achieve scintillation process. Organic scintillators have energy levels that are represented by the π-electron structure. From Figure 2.4, S_0 is the ground state and is the lowest energy level any molecule can have. This state and all other higher energy levels can be divided into a set of vibrational states that are separated in energy by about

0.15 eV. S_{00}, S_{01} and S_{02} are the lowest vibrational state, first higher vibrational state and second higher vibrational state respectively, each relates to a spin of 0. A similar set of triplet energy levels are denoted as T_1, T_2 and T_3 with spin of 1 are also shown in Figure 2.5. Upon the absorption kinetic energy from a charged particle, a molecule can be excited into a higher state. However, if it gets excited into either S_{01}, S_{02}, S_{03}, it will de-excite via a process known as internal conversion which result in the emission of photon.

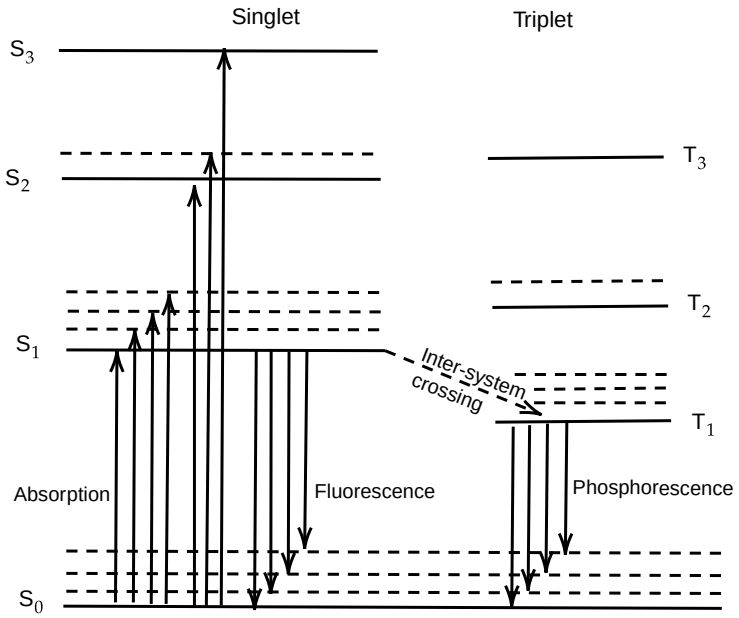

Figure 2.4: Diagram showing the scintillation mechanism in organic scintillators. Figure reproduced from [33].

The energy spacing between one state to another, say S_0 and S_1 is 3 to 4 eV. For higher-lying states, the spacing is somewhat smaller than 3 eV. Almost all molecules at room temperature are in S_{00} state, this is because the spacing between the vibrational states is larger than the average thermal energies (0.025 eV). The time it takes an excited state to decay back to the ground state is short, usually in the order of few nanoseconds, therefore this is classed as the prompt scintillation component. De-excitation from the S_{10}

to S_{00} produce the light emission that can be described by an exponential decay law. The light intensity i at a time t can expressed by equation 2.11:

$$i = i_o exp\left(\frac{-t}{\tau}\right) \tag{2.11}$$

where i_o represent the initial intensity and τ represent the time decay constant.

In organic scintillators, when the excitation centres are relatively spaced far apart, the interaction between them becomes minimal and a phenomenon known as *Quenching* occurs. For particles with low stopping power such as electrons above 100 keV [34], the light yield L produced by this particle is proportional to the deposited energy ΔE deposited within the crystal as expressed by:

$$L \propto \Delta E \tag{2.12}$$

This can further be expressed as:

$$\frac{dL}{dr} = S\frac{dL}{dr} \tag{2.13}$$

where S represents the scintillation efficiency. However, this is not always the case for heavy charged particles like protons and heavy ions where the light yield is quenched according to Birks' law [35]:

$$\frac{dL}{dr} = S\frac{\frac{dE}{dr}}{1 + kB\frac{dE}{dr}} \tag{2.14}$$

where kB is Birks' constant: k represent the energy transfer probability and B, is a constant of proportionality associated with the number of damaged molecules as described by [34] and the references content therein. This relationship does not hold for particles with a very high linear energy transfer (LET), because it fails to account for the for the spatial configuration of the fluorescence as well as the damaged molecules.

Equation 2.14 leads to the concept of electron equivalent energy which is used to described the Q value of any reaction within a scintillator, and is usually written as keVee, MeVee etc.

2.2.2.2 Inorganic Scintillators

Inorganic scintillators are crystals, which most commonly come in the form of alkalides, halides and pyrosilicates. Examples of inorganic crystals include but not limited to: NaI(Tl), CsI(Tl), CsI(Na), cerium-activated lithium glass scintillators (GS10 and GS20), noble gas scintillators or other cerium-activated crystals such as $CeBr_3$, $LaBr_3$ and crystals of BGO (bismuth germanate). They are insulators or semiconductors, therefore their light emission mechanism is based on the discrete bands of energy within their crystal lattice.

The scintillation mechanism within an inorganic material is determined by it's crystalline structure. These crystal have two energy bands known as valence and conduction band and are separated by a forbidden band gap region. The electrons in the valence band are bounded to the crystalline lattice and therefore can only leave this band upon gaining sufficient energy to the conduction band by creating a hole in the valence band. The electrons in the conduction band are free to move around, they are attracted to the holes in the valence band and de-excite by emission of a photon. The emitted photon has a discrete energy which is a representative of the band gap size. Figure 2.5 shows an electronic band gap structure of an inorganic crystal.

Activators such as Ce and Tl are used to ensure that the the emitted photons are not reabsorbed by changing the photon energy produced in the crystal. Without these activators, the crystal would be opaque.

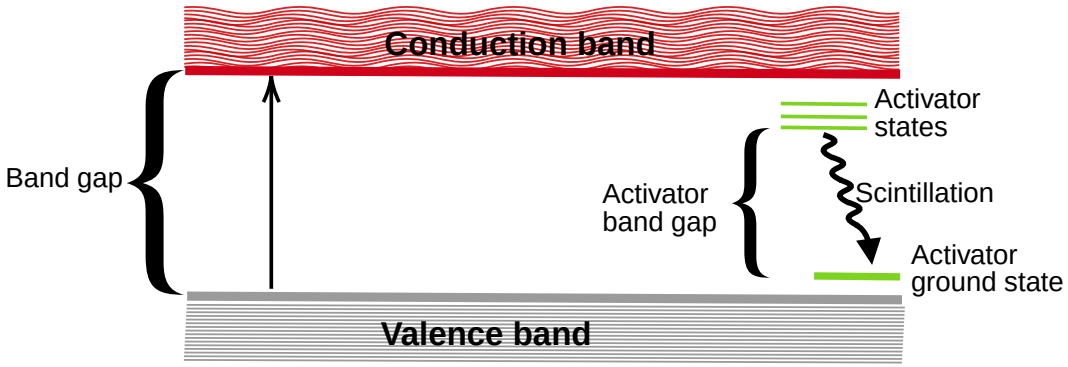

Figure 2.5: Diagram showing electronic band structure of an inorganic scintillator. When a particle deposit its energy within the scintillator, electrons from the valence band (grey) are excited to the conduction band (red). The electrons de-excite from the conduction band through near lying activator states (green) by the emission of photons. Figure from [36].

2.2.3 Photo-Detector

2.2.3.1 Photomultiplier Tubes

The most common photo-sensor in the oil and gas industry is the photomultiplier tube (PMT). This is due to its ruggedness and ability to detect radiation intensity up to single photon level. Figure 2.6 shows a schematic diagram and principle of operation of a photomultiplier tube. It is a vacuum tube that generate an electric signal in response to incoming electromagnetic radiation. A PMT contains a photocathode, multiple dynodes, and an anode which are all sealed in a glass envelope with high vacuum inside. They are very high gain light amplifiers. When a photon is incident on a PMT, it undergoes the following steps as summarised in [23]:

- The incident photon enters the tube via the input photocathode window.
- The photons excite the electrons of the photocathode, some of which are emitted from surface into the vacuum. These emitted electrons are referred to as photoelectrons.

- The focusing electrode focuses the photoelectrons onto the first secondary electron emission surface known as dynode. The number of photoelectrons is amplified through the secondary electron emission effect.
- The amplification process of the secondary electrons is repeated through several dynodes up to the last dynode where high electron number amplification is achieved.

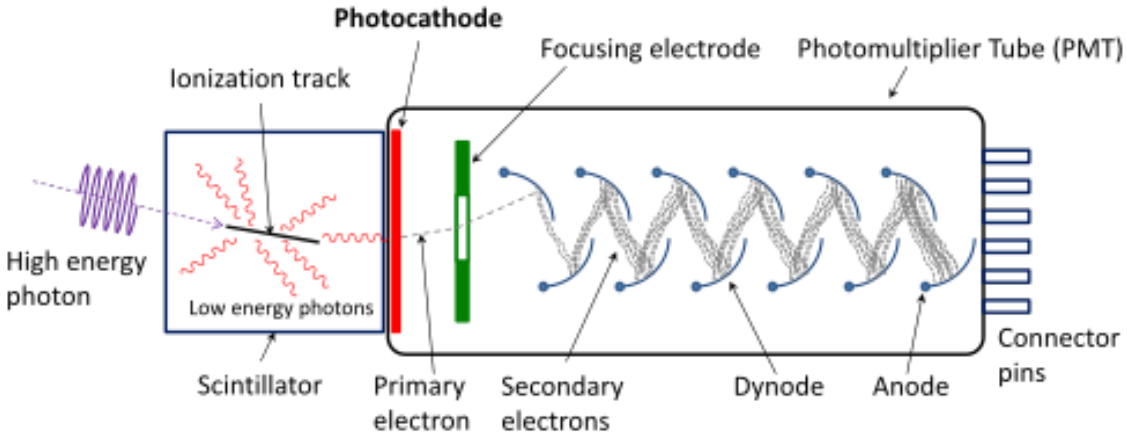

Figure 2.6: Schematic diagram illustrating the components and the basic working principle of a Photomultiplier [37].

Photomultiplier tubes are more widely accepted in the logging industry and other applications due to their very high temperature insensitivity, high gain, low dark current and good signal-to-noise ratio. Despite all these great advantages, PMTs also have some disadvantages which include bulkiness, susceptibility to magnetic fields, and high voltage requirements (typically $\geq$ 1000 V) [38].

2.2.3.2 Silicon photomultiplier (SiPM)

The silicon Photomultiplier (SiPM) was developed as an alternative to the conventional photo-sensor (PMT, as described in section 2.2.3.1). It is a novel semi-conductor photo-sensor operated in limited Geiger mode [39–41]. Unlike the PMT, SiPM requires very low operating voltage. It consist of an array of small (20-50 μm, depending on the manufacturer) microcells that are independently arranged on a 1 to 6 mm^2 substrate, overall

containing between 500 - 4000 microcells/mm^2, depending on the manufacturer. Each microcell, as shown in Figure 2.7 is operated with a bias voltage (V_{bias}), which is a few volts above the breakdown voltage, as expressed in equation 2.15. This enables the created photoelectron in the silicon, after reaching the high field region either through diffusion or drift initiates a Geiger discharge confined to the microcell. The discharge is quenched by the quenching resistor in each microcell by limiting the current. All the independent microcells are connected to a single readout channel; the summed output signal correspond to the sum of all fired microcells, which is measure of the light flux.

$$V_{\text{bias}} = V_{\text{br}} + \Delta V, \tag{2.15}$$

where Vbr is the breakdown voltage which is the minimum voltage required to generate high-enough electric field for to avalanche to occur. The ΔV is the applied overvoltage above the breakdown voltage (V_{br}) where measurable signals are observed.

Some important parameters that evaluate the performance of an SiPM [42] can be summarised as:

- Gain: This defines the amount of charge created for each detected photon, and is a function of overvoltage and microcell size.
- Photon detection efficiency (PDE): This is a measure of the sensitivity of an SiPM and is a function of wavelength of the incident light, the applied overvoltage and microcell fill factor.
- Dark count rate (DCR): This is primarily due to thermal electrons generated in the active volume. The DCR is a function of active area, overvoltage and temperature and is the main source of noise in an SiPM.
- Optical crosstalk: This occur when accelerated carriers in the high field region emit photons that initiate a secondary avalanche in a neighboring microcell. It is a function of overvoltage and is also affected by the fill factor of a sensor.

- Afterpulsing: This occurs when carriers get trapped in defects in the silicon, which after a delay of up to several ns, the trapped carriers are released, potentially initiating an avalanche and creating an afterpulse in the same microcell.

- Dynamic range and linearity: This defines the optical signal range over which the sensor provides a useful output. It is a function of the total number of microcells, the overvoltage used, and the wavelength of the incident photons.

- Temperature dependency which primarily depends on the change in the breakdown voltage and the dark count rate. The breakdown voltage of an SiPM changes linearly as a function of temperature.

Figure 2.8 shows an image of the SiPM (6×6 mm^2 Hamamatsu S14160-6050HS SiPM) used in this project.

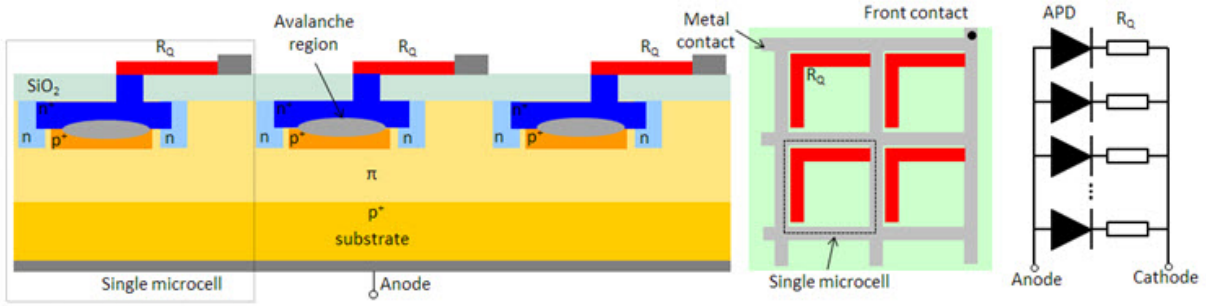

Figure 2.7: Schematic diagram illustrating the components and the structure of a SiPM. The quenching resistor (R_Q) controls the current to allow for resetting the bias while the SiO_2 provide electrical isolation. Taking from [43].

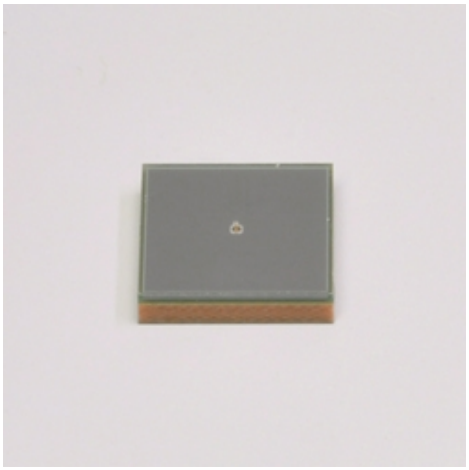

Figure 2.8: S14160-6050HS SiPM by Hamamatsu, it's one of the SiPM used for high temperature measurements in this research. Taken from [44]

2.3 Thermal Neutron Detectors

Thermal neutrons are detected via charge conversion since they are not by themselves ionising radiation. A good neutron converting material should have a large neutron absorption cross-section and the reaction between with such material should result in a large reaction Q value. Larger Q value and larger cross-section can allow for the production of small and efficient thermal neutron detectors. ^{3}He, ^{10}B and ^{6}Li are the most widely used neutron converting materials for thermal neutron detection. The thermal neutron absorption cross-section of ^{3}He, ^{10}B and ^{6}Li are 5330, 3840 and 940 barns respectively. Figure 2.9 shows the total neutron cross-section for ^{3}He, ^{10}B and ^{6}Li as a function of neutron kinetic energy. Before the resonance, in a region known as $\frac{1}{v}$ region, the absorption cross-section falls with increasing neutron energy according to $\frac{1}{v}$ law.

^{3}He tubes are the conventional detector type used for this application. A description of some alternatives detectors based on boron and lithium are reviewed below.

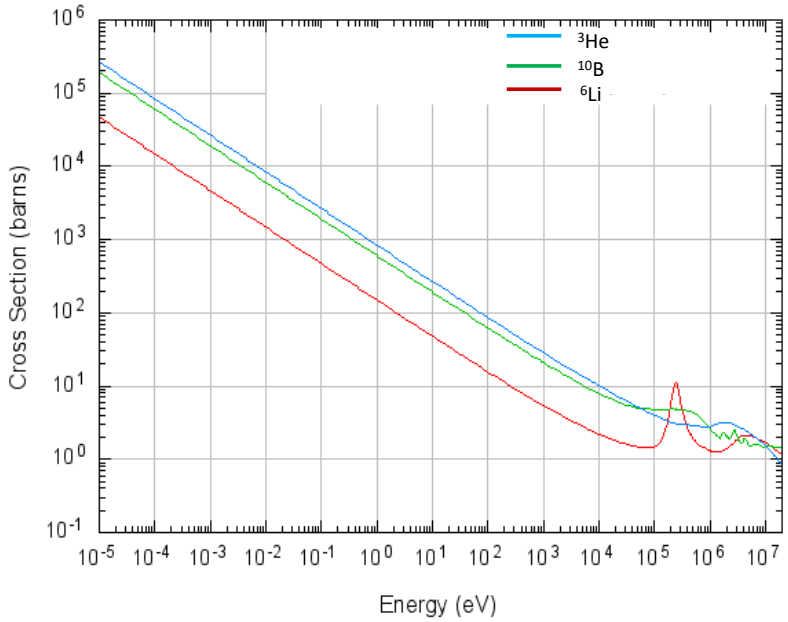

Figure 2.9: Dependence of cross-section on energy for ^{3}He (blue), ^{10}B (green), and ^{6}Li (red)[45]

2.3.1 ^{3}He Neutron Detector

The detector utilises the $^{3}He(n,p)^{3}H$ reaction as expressed in equation 2.16 which has a very high cross section at thermal neutron energies. ^{3}He proportional counters exploit this reaction to detect thermal neutrons, with a Q value of 0.764 MeV, the kinetic energy of the two decay products is deposited in the gas of the detector:

$$^{3}He + n \rightarrow {}^{3}H + p \tag{2.16}$$

The thermal neutron absorption cross section of ^{3}He is around 5327 barn. This property makes it the most common fill gas used in proportional counters for use in the oil and gas industries and other applications. As explained earlier, the scarcity and high demand for neutron detection technology has led to the search of other alternative thermal neutron detection technology.

2.3.2 ^{10}B Based Neutron Detectors

The $^{10}B(n,\alpha)^{7}Li$ reaction is one of the most common reactions used in the conversion of thermal neutrons into charged particles which can be detected directly. This reaction leaves ^{7}Li in either its ground state or in an excited state, with Q values of 2.79 MeV and 2.31 MeV, respectively. These are described in equations 2.17 and 2.18:

$$^{1}_{0}n+^{10}_{5}B \rightarrow ^{7}_{3}Li(1.78\ MeV)+^{4}_{2}\alpha(1.02\ MeV) \quad (ground\ state\ with\ Q = 2.79\ MeV) \quad (2.17)$$

$$^{1}_{0}n+^{10}_{5}B \rightarrow ^{7}_{3}Li^{*}(0.84\ MeV)+^{4}_{2}\alpha(1.47\ MeV) \quad (excited\ state\ with\ Q = 2.31\ MeV) \quad (2.18)$$

Below is a description of some of these ^{10}B based alternative technologies:

2.3.2.1 Boron trifluoride (BF_3) filled proportional counters

Boron trifluoride *(BF_3))* is a direct replacement of the conventional ^{3}He tube [9, 12]. The hazardous nature of the BF_3) gas combined with the need for high pressure tubes pose a great disadvantage compared to the conventional detector. Despite having a lower thermal neutron absorption cross section (3840 barn) as compared to ^{3}He, these detectors offer good neutron/γ separation with very high count rate capabilities. The hazardous nature of the gas limits the amount of gas to be pressurised into the detector, hence multiple *(BF_3)* tubes at a small pressure are required to provide a good thermal neutron detection efficiency. It was reported that two BF_3 tubes filled to $\approx$ 1 atm each can perform better than one ^{3}He tube filled to 3 atm [9].

2.3.2.2 ^{10}B lined proportional counters

^{10}B lined proportional counters are also a direct replacement of ^{3}He. Unlike BF_3 filled proportional counters, the safety-related limitation on high pressure tubes has been reduced. In this type of technology, ^{10}B is lined on the inner wall of the counter [13, 14], thereby allowing to use a less or non hazardous fill gas. They are very similar to the BF_3 tubes in design. Some limiting factors affecting this design is the inner surface area, the

accurate determination of the ^{10}B thickness as well as the special requirement for a specific sputtering technology.

2.3.2.3 ^{10}B lined high surface area detectors

The active surface area limitation of the ^{10}B lined proportional counters can be overcome by using a modified detector geometry. One such geometry employs multiple coated straw tubes which can be made from cheap materials like aluminium. A ^{10}B coated straw detector filled with $ArCo_2$ gas mixture that was optimised with respect to its straw geometry found improved gamma-ray rejection and observed faster electronic signals [13]. Furthermore, it provides safety advantages such as no requirement for pressurization and no toxicity or flammability.

This technology will especially be useful for applications that only require count rates. It was found to have 29 and 30 counts per second (cps) for a large and a small ^{252}Cf source with 85 straws respectively, the corresponding performance of ^{3}He based radiation portal monitor deployed by the US homeland security is at least 20 cps for design with single tube and 32 for design with two tubes [13]. In a more recent experimental study of ^{10}B-coated straws with a neutron source using the China Spallation Neutron Source (CSNS) commissioned in 2018 [14], the detector was tested at IHEP, and the measured spectrum shows a clear distinction between the neutron and γ events.

2.3.2.4 ^{10}B doped scintillators

In this type of detector, a conventional plastic scintillator is coated with a ^{10}B containing compound. Plastic scintillators have a very fast decay time which allows for high counting rates. These devices are economical to produce in large numbers and sizes. These detectors are suitable for fast neutron detection applications. The use of moderating material such as polyethylene can also make them suitable for thermal neutron detection.

Research into the efficiency of ^{10}B-lined NaI detectors [46] shown a good sensitivity to neutrons. In a more recent work, this technology demonstrated a good sensitivity

to changes in neutron flux [47]. The same work explains an added advantage of this technology, which is the ability to provide information about the characteristic γ rays originating from the samples as well as from any nearby material emitting γ rays. This is good news for applications needing to have a detector that is sensitive to both neutrons and γ rays.

2.3.3 ^6Li Based Neutron Detectors

Neutron detection using ^6Li as a converting material is based on the following reaction:

$$^1_0n + ^6_3Li \rightarrow ^3_1H(2.73\ MeV) + ^4_2\alpha(2.05\ MeV), Q = 4.78\ MeV. \tag{2.19}$$

^6Li has an absorption cross section of 940 barn. It has 1/v dependence except at the resonance region between around 0.15 MeV and 0.3 MeV. At this region, the absorption cross section of ^6Li is quite high.

2.3.3.1 ^6Li foil scintillator sandwich

^6Li foil scintillator sandwich is another ^{6}Li detection method where multiple layers of reactive film a and light guides are stacked together. Research that adopted this type of technology to detect thermal neutrons reported an intrinsic efficiency per layer between approximately 20% and 35% [48]. The detector also shows higher efficiency compared to ^3He.

Another form of this alternative is based on commercial solid state silicon detectors coupled with thin neutron converting layers of ^6LiF deposited onto carbon fiber substrates. In a recent work [49], ^6LiF was obtained as a powder and then evaporated under vacuum into substrates forming layers of different thicknesses. Measurements from such a detector showed a reasonable thermal neutron detection efficiency of $\approx 5.2\%$. In another research, a similar technology was adopted and the thermal neutron detection efficiency was found to be around 8% [50]. This efficiency, the γ rejection performance and the rather low cost as compared to ^3He tubes makes these detectors quite interesting for several applications.

2.3.3.2 ^6Li-loaded glass neutron detectors

After ^3He detectors, most commonly used thermal neutron detector by the oil and gas for neutron porosity measurements is the ^6Li-loaded glass scintillator. GS20 is a class of this detector that has been used in borehole logging applications [51, 52]. The lack of long-range order in the atomic structure of GS20 acts as a constraint to increase it's light yield. One way to overcome this constraint is by the use of dopants like Ce^{3+} ions. The heterovalent properties of cerium makes this technologically challenging. A study [53] showed how this limitation can be overcomed. Here, nanocrystals were incorporated into the glass matrix to synthesize glass ceramic scintillator by partial crystallization of Ce-doped lithium-silica glass scintillator (KGS3-3). Both GS20 and KGS3-3 were reported to have decay time constant of 70 ns with the measured light output from KGS3-3 crystal more than twice that of the pure GS20. A very recent work [54] compared the temperature dependence of GS20 and some lithium-calcium-aluminium-floride based scintillators. The measurements were made between 25℃ and 150℃. Even at the highest temperature, the light output was 42% as compared to the lowest temperature measurement. Another recent study [55] investigated the luminescent properties of GS20 at low temperature (between 37℃ and -213℃). The use of GS20 for other applications can be found in [56, 57].

2.3.3.3 $Cs_2LiYCl_6(Ce)$ ($CLYC$) Scintillators

CLYC scintillators are a type of detection technology that allows for both neutron and γ ray detection [58][59]. It relies on the fact that neutrons and γ rays produce scintillation light with different time profiles making it easier for pulse shape discrimination. CLYC samples enriched with ^6Li have over two times the absorption cross section of ^3He. This property makes it suitable for two in one applications. The emission in this type of technology consist of core-valence luminescence and cerium emission. In a research to find some selected properties of elpasolites, this detector was found to have an energy resolution of 3.9% for 0.662 MeV γ rays [60].

This detector has been used in borehole logging applications [61] to derive a new density

measurement method using fast neutron and γ ray counts only. This detector can provide porosity information with its thermal neutron detection capability. This method, not only replaced the conventional detector for neutron and gamma measurements, but also avoids the use of multiple detectors in a logging tool.

2.3.3.4 $Cs_2LiLaBr_6(Ce)$ ($CLLB$) Scintillators

This is also another class of elpasolite that also permits dual measurement with good energy resolution [62][63]. The only difference is through it's emission process, which unlike CLYC, doesn't exhibit core-valence luminescence, which is due to its low band gap. Its light yield has been measured to be as high as 6×10^4 photons/MeV. This leads to an excellent 2.9% energy resolution for 0.662 MeV γ rays [60]. In terms of detector geometry, this is almost, if not smaller, than ^{3}He tube.

2.3.3.5 $LiCAF$ Scintillator

Lithium calcium aluminium flouride (LiCAF) scintillator is a new form of ^6Li-based thermal neutron detector. It is available in two common known dopants, $Ce : LiCAF$ and $Eu : LiCAF$. Depending on the area of application, both dopants have their advantages and disadvantages. Overall, all of them are known to have great neutron detection efficiency. $Ce : LiCAF$ scintillator has a very fast decay time (40 ns) as compared to Eu:LiCAF scintillator (above 1000 ns). $Ce : LiCAF$ has low effective Z of 15, which also makes it less sensitive to γ rays [64][65]. On the other hand, the luminescent wavelength of $Eu : LiCAF$ as compared to $Ce : LiCAF$ is 360-390 nm and 280-320 nm respectively. Both scintillators are transparent and non-hygroscopic. In either dopant, the ratio of the scintillation efficiency for alpha particle to that for electrons is low. In a recent experiment, $Eu : LiCAF$/rubber [65] was evaluated and found to have excellent discrimination ability.

2.4 Fast Neutron Detectors

The absorption cross section is low within the fast neutron energy range (10^4-10^6 eV), as a result thermal neutron detectors are not suitable for fast neutron detection. The detection of fast neutrons relies on transferring some of the neutron's kinetic energy to a charge particle capable causing ionisation. For thermal neutron detectors to be suitable for fast neutron detection, a moderating material that slows down the neutron to thermal energy range is needed. From energy and momentum conservation, the largest energy transfer possible by a neutron is with a proton since they have nearly identical mass. Fast neutron detection is based on either proton or deuteron recoil, hence explains why neutrons scattering off heavy nuclei will only impart small amount of energy [34]. Unlike in thermal neutron detection mechanism where the information of the primary neutron is lost because the resultant Q value is larger than the energy of the neutron, information about the neutron is not lost in fast neutron detection mechanism. An ideal detector for fast neutron detection would be hydrogen rich scintillator in the class of organic scintillators as described in 2.2.2.1.

One unique characteristic of fast neutron detectors, compared to thermal detectors, is their sensitivity to g-rays. This enables the detection of g-rays that originate from neutron interactions with the rock material, increasing the analyzing power of the tool. As stated in the introductory chapter, one of the aim of this research is to characterise a dual detector for neutron and γ ray detection in the oil and gas industry. $CLLB$, $CLLBC$, $GS20$ and $LiCAF$ scintillators are selected in this research for the simulation and experimental analysis. Dual detection mediums require additional analysis techniques to distinguish between the signals produced via neutron and gamma ray detection, known as pulse shape discrimination. (see Chapter 4).

2.5 Interaction of γ with Matter

Photo-electric effect, Compton scattering and pair production are the three primary ways through which a photon (γ rays or X-rays) interact with matter.

2.5.1 Photo-electric Effect

The photoelectric effect is the most dominant interaction mechanism for low energy photons (0-0.5 MeV). It is characterised by the absorption of a photon by an atomic electron bounded to an atom, due to momentum conservation this process cannot occur with a free electron. After the absorption process, a photoelectron is ejected with energy:

$$E_e = hv - E_b \tag{2.20}$$

E_b is the binding energy (usually of the order of keV) of the electron in its bounded K shell, hv is the incoming photon energy where h and v are Plank constant and the photon frequency respectively. The probability of photoelectric effect happening is directly proportional to the atomic number Z of the material and inversely proportional to the incoming photon energy as described by

$$\tau_f \approx \frac{Z^n}{E_\gamma^{3.5}}, \tag{2.21}$$

n is an index which depends on the energy of the incoming photon, it's usually between 4 and 5.

2.5.2 Compton Scattering

Figure 2.10 illustrates the process of Compton scattering where an incoming photon with energy hv interacts with an electron in the external shell of an atom contained in the interacting material, thereby transferring some of it's energy. After the interaction, the electron is deflected through an angle ϕ while the photon of energy hv$'$ is deflected through an angle θ. Applying the laws of energy and momentum conservation, the scattered photon

energy E$'$ and the electron energy can be related to the scattering angle by equations 2.22 and 2.23 respectively.

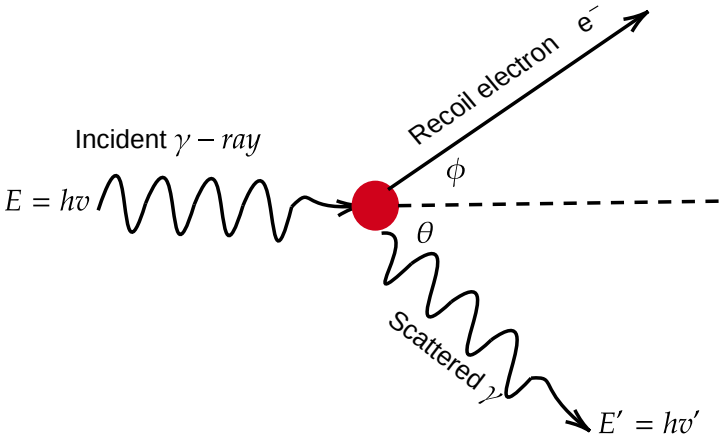

Figure 2.10: Illustration of incoming γ ray Compton scattering off a nucleus.

$$hv' = \frac{hv}{1 + \frac{hv}{m_o c^2}(1 - cos\theta)} \tag{2.22}$$

$$E_{e^-} = \frac{\frac{hv}{m_o c^2}(1 - cos\theta)}{1 + \frac{hv}{m_o c^2}(1 - cos\theta)} \tag{2.23}$$

2.5.3 Pair Production

The pair production process occurs when an incoming photon is converted into electron-positron pair. The probability of this interaction is large for high energy photons. Only when the g-ray energy is twice the electron mass, 1.022 MeV, can this process occcur. Any excess energy above this threshold is converted to kinetic energy of the electron-positron pair. Since this process is caused by an interaction with the electromagnetic field of the

nucleus, its probability increases with increasing atomic number as expressed in equation 2.24:

$$\tau_{pp} \propto Z^2 \tag{2.24}$$

Chapter 3

Geant4 Monte Carlo Simulation

This chapter presents the simulation work that was performed to evaluate the performance of alternative thermal neutron detectors compared to the conventional ^3He tube detector as used in the oil and gas industry. In section 3.2, the geometry of all the simulated detectors are presented and discussed. Section 3.3 compares the counting efficiency of the detectors. Section 3.4 presents the simulation of nuclear well-logging environment with different logging tools.

3.1 Overview of Geant4

For cost effectiveness, almost all experiments use Monte Carlo simulation to solve problems that are very difficult to achieve analytically. Like other applications, nuclear well-logging uses a lot of scientific and engineering concepts to design and build logging tools. These tools need to meet some environmental, mechanical and physical requirements for efficiency. The oil and gas use simulation to design and evaluate the performance of a logging tool prior to its fabrication. Repeated simulations improves the statistical significance of it's predictions by reducing the fractional statistical error.

GEANT4[66] Monte-Carlo toolkit is developed by CERN, which is universally available and is open source. It allows a user to design and build a simulation of the passage of

particles through matter and its interactions. The toolkit was initially intended to simulate particle and nuclear physics experiments, it has however spanned to other applications such as homeland security, oil and gas logging and medicine. It has help in understanding the physical processes in existing experiments, it has has also become almost mandatory in prototyping and designing new experiments. Other Monte-Carlo simulation packages such as MCNP[67] and FLUKA[68] also exist and can be used for a similar purposes. However, the versatility of GEANT4 gives it an advantage over these alternatives. GEANT4 is scripted in the c++ programming language, which is a more modern and widely accepted programming language as compared the FORTRAN which is the language used by FLUKA. Unlike to GEANT4, MCNP requires a license and is a trade mark of Los Alamos National Laboratory.

3.2 GEANT4 Application and Implimentation

3.2.1 Physics Lists

In GEANT4, physics processes are taken care of by different physics lists. In this work, neutrons and γ rays are the primary particles of interest. While the neutrons are handled by hadronic process, the γ rays are handled by electromagnetic process physics list. The neutron interactions are either classified into elastic, inelastic, radiative capture, charge exchange reaction or fission. The *G4NeutronHPElastic* package has been set up as the harmonic elastic scattering physics list in the earlier versions of GEANT4. The *G4ParticleHPElasticData* package has replaced the earlier package in the recent versions of GEANT4. High precision package is used by GEANT4 based on the evaluated data library (G4NDL)[69] of reaction cross sections to describe other neutron reactions (radiative capture, inelastive, charge exchange reaction, and fission) below 20 MeV.

3.2.2 Primary Particle Generation

Primary particles are defined and generated within the *G4VUserPrimaryGenerationAction* class reference. The *G4GeneralParticleSource* and *G4GeneralParticleGun* based classes allows each particle to be defined by specifying it's type (neutron, proton, electron, positron, γ, etc.) and assigning it's momentum, position, energy, direction, angular distribution, etc. Ions are created using their atomic number (Z), mass number (A) and excitation values. These particles or ions are then propagated into the simulated geometry. In this study, the general particle source is used to simulate the full energy spectrum of AmBe fast neutron source and the 662-keV γ ray from a ^{137}Cs source.

3.2.3 Recreating the Geometry

In GEANT4, geometries are recreated as accurate as possible for optimum accuracy. Simple geometries are created using the *G4VSolid* class reference (G4Box, G4Tubs, G4Cons, etc.) which handles the shape and size of a geometry; *G4LogicalVolume* class reference (G4Material, G4SensitiveDetector and G4VisAttributes) which handles the daughter volume of the geometry, and the sensitive part of the geometry; and *G4VPhysicalVolume* class reference (G4PVPlacement and G4PVParameterised) which determines the position and rotation of the geometry. Complex geometries can be recreated by the use of one or more of the Boolean solids (G4UnionSolid, G4SubtractionSolid and G4IntersectionSolid). Very complex geometries are simulated in GEANT4 using the Geometry Description Markup Language (GDML) [70]. Complex geometries are easier drawn using computer-aided design (CAD). The CAD geometry is then converted into GDML using an external tool like SW2GDML [71] and tihonav [72]. The converted GDML file will then finally be imported into GEANT4 using the *G4GDMLParser* class reference.

Regardless whether the geometry is simple or complex, every simulated geometry is placed in a mother volume. This was defined to be air as this is the environment where all the physics process will occur. Simulated geometries are placed inside the logical mother volume and no physics processes can be tracked or recorded outside of the mother volume.

The second stage is to define the detectors shapes and sizes which must be smaller than the mother volume. The detectors and other geometries materials can be defined manually using isotopes, elements, molecules, compounds and mixture. *G4Isotope* and *G4Element* describe the properties of atoms such as the atomic number, number of moles, number of nucleons, cross sections etc. The macroscopic properties like pressure, temperature, density, state, radiation length etc are described by *G4Material*. One can also make use of *G4NistManager* to include a user defined isotopes, elements and materials. Finally, the type, position, direction, angular distributions and energy distributions of the radiation source is specified.

3.2.4 Extracting Information from GEANT4

GEANT4 does an excellent physics simulation when geometry, physics processes and primary particle informations are accurately given. The user however, may have to perform additional analysis outside of Geant4 using its output to achieve increased predictive power. There are three methods commonly in use to extract information out of GEANT4. The first method is by the use of a scoring functionality to assign sensitivity to a logical volume of a geometry. Sensitivity is added to a logical volume using an abstract base class (*G4VSensitiveDetector*). The sensitive detector constructs a hit object using information from the steps along a particle track. The ProcessHits() method of *G4VSensitiveDetector* performs this task using G4Step objects as it's input. The second method is a macro based scoring, which is a command-based functionality that provides a built-in scoring mesh and various scorers for commonly-used physics quantities such as dose and flux. A third method is the use of user hooks (*G4UserTrackingAction*, *G4UserSteppingAction*, etc.). The user can specify the physics process, volume of interest, particle of interest, thresholds, etc. of the required particle. The information obtained using any of the three method can be written to a file for further analysis. Due to the vast applications of GEANT4, it doesn't provide an analysis tool. Each user chooses a format that suits their application. Commonly used tools are Python and ROOT. In this work, all analysis was carried out using

ROOT.

The third method was used for entire simulations in this thesis. The type of particle tracked, the physics quantities recorded from the particle, the physics process, the energy deposited, the energy threshold, the volume of interest were all defined in *G4UserSteppingAction*. The energy recorded by GEANT4 is a delta energy with exact resolution, a Gaussian function is used to smear the delta energy to correspond to real energy resolution.

3.3 GEANT4 Simulation of the Logging Environment

A logging environment consist of the rock formation under investigation, a drilled borehole into the rock formation and a nuclear log which consist of one or more radiation detector(s), radiation source and other read-out electronics. Fast neutrons and γ rays are the two radiations used for logging purposes. These radiations interact with the surrounding materials, and therefore contribute to the tool response. It is therefore useful to simulate the tool as accurately as possible to account for any contribution from other materials in the tool other than the rock formation. Therfore, a CAD diagram of the tool in .STL file format was obtained from Robertson Geologging Company, a company specialised in the kdesign and maintenance of logging tools, and converted into GDML using tihonav code. This was then converted into a tessellated GDML file and imported into GEANT4 using *G4GDMLParser* as described in subsection 3.2.3. While GDML file format allows for the simulation of the exact geometry as drawn with CAD, it also created the problem of dealing with hundreds of individual components that makes up the bulk geometry. Figure 3.1 shows the logging tool after importing into GEANT4. Another problem encountered using GDML is of it's large memory requirement, as the files are usually large in size. This also leads to very long simulation running times and limited events per simulation run. In this application, high statistics is very important. Due to this requirement and limitations, a

simplified geometry was used throughout the simulation.

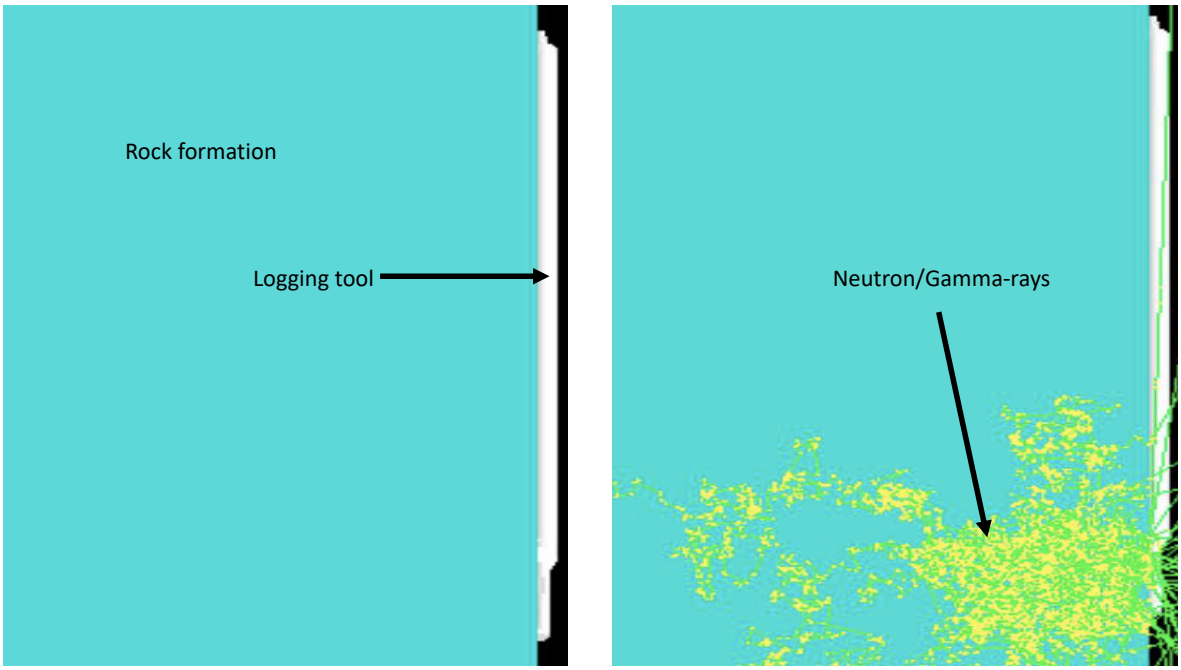

Figure 3.1: The left geometry shows the GDML logging tool imported into GEANT4 with zero events simulated. The right shows similar tool with 500 fast neutrons events fired into the rock formation.

3.3.1 Thermal Neutron Detectors Simulation

3.3.1.1 ^3He Proportional Counter

A standard ^3He tube commonly used in the oil and gas industries was simulated. It was designed to be a cylinder with 2.54 cm diameter and a total active length of 12.7 cm. ^{3}He and CO_2 gas mixture was used as the fill gas at a ratio of 99% to 1% respectively. The detector container was defined to be be an iron cylinder of thickness 1.25 cm. This thickness is thin enough to allow the passage of thermal neutrons and also thick enough to withstand the typical pressure used, 4 atm. This gas mixture serves both as a target for the incoming neutrons and an ionisation medium for the proton and triton produced via $^3He(n,p)^3H$ as described in chapter 2.

3.3.1.2 Lithium-based Detectors

Two lithium-based scintillation neutron detectors were simulated. Both detectors have the same active area to the conventional ^3He detector. Lithium calcium aluminum fluoride doped with europium ($Eu : LiCAF$) and lithium aluminum silicate loaded glass ($GS20$) are both scintillation detectors. $Eu : LiCAF$ composed of 6.6 % lithium enriched to 5%^7Li and 95%^6Li, 32% aluminum, 18.4% calcium, 33% fluoride and doped with 10% europium. The GS20 also contains 6.6% lithium enriched to 95%^6Li and 5%^7Li, 31.95% dialuminum, 47.34% silicate and doped with 14.11% dicerium.

3.3.1.3 Boron-based detector

^{10}B-based star straw tube detector was also simulated. The thickness of the detector container and the active length are similar to that of the conventional ^3He detector. The detector contains 37 star straws with a 1μm thick boron carbide ($^{10}B_4C$) coated on the inside wall of each star straw. The cross-sectional view of the star straw boron coated detector is shown in Figure 3.2. The coating serves as the converting material to the incoming neutrons to charged particles. The thickness used is the optimum thickness as available in the literature [73]. The thickness is large enough to stop the incoming neutrons and also thin enough to allow the charged particles into the fill gas. A mixture of argon and carbon dioxide at a ratio of 90:10 [73] respectively was the fill gas at a pressure of 4 atm. Other configurations of the boron coated straw tube detectors are also available in the literature, see for example [74].

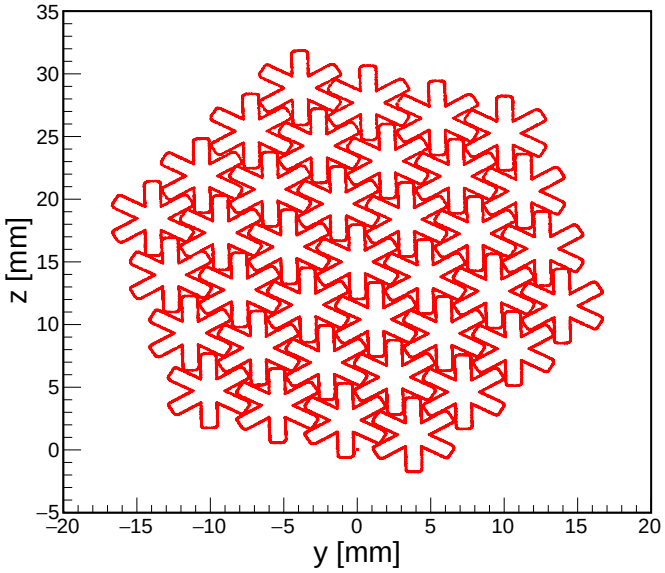

Figure 3.2: Showing the cross sectional view of the interaction points in a star straw boron coated detector.

For a valid comparison, the simulated ^{3}He, ^{10}B and ^{6}Li based detectors were used in a standard logging tool as shown in Figure 3.4. For each tool, two detector volumes were defined, referred to as *near* and *far* detectors. Material composition and other dimensions are presented in table 3.1. The near detector and far detector had their centres placed at 40 cm and 60 cm away from the centre of an $AmBe$ fast neutron source respectively. After recreating all the geometries, the Q value of each reaction process associated to each material with a thermal neutron was reproduced. The full energy spectrum of $AmBe$ fast neutron source as shown in Figure 3.3 was used in a macro based file as the primary particle generator which produces fast neutrons of energy range between 0.1 MeV and 10.8 MeV. This source was treated as a point source in the simulation and is reported to emit averagely 2.2×10^{6} neutrons per second per curie [75]. To compare the counting efficiency of the simulated detectors, 5×10^{6} neutrons, corresponding to the number of fast neutrons emitted from a 92 GBq $AmBe$ source per second were simulated in each case. This neutrons were emitted isotropically into a limestone rock formation serving as a moderator.

To survey for the presence of hydrocarbons, neutron porosity tool (neutron-neutron tool), density tool (gamma-gamma tool), lithology tool (neutron-gamma) and other complementary tools are required. These tools consist of radiation sources and radiation detectors. Any technology that combines multiple purpose will not only reduce the logging cost, but also the safety related issues attributed to the radiation sources. Here, the capability of $GS20$ as thermal neutron detector to be used in neutron porosity tool and a gamma-ray detector for use in lithology and density log is investigated. The obtained results will be compared with the conventional neutron detector (^{3}He) as well as the conventional gamma-ray detector ($NaI:Tl$) as used by the oil and gas industries. The specifications of all modelled tools are as follows:

- The rock formation is a homogeneous mixture between limestone and water with a volume of 12,000,000 cm^3. The amount of water (porosity) is control with the code.
- The borehole is set to be a cylinder with a height and a radius of 200 cm and 5 cm and filled with fresh water.
- The neutron porosity (neutron-neutron tool) tool is a cylinder of iron with a height of 200 cm and a radius of 2.15 cm. It contains two (2) cylindrical ^3He thermal neutron detector of height and radius 12.7 cm and 1.18 cm each respectively. Both detectors are placed at different distance away from an isotropic point AmBe neutron source.
- The neutron-gamma tool has the same dimensions as the neutron-neutron tool. It contains two (2) NaI detector of similar dimensions to the ^3He thermal neutron detectors. Both gamma-ray detectors are placed at two different distance away from the $AmBe$ neutron source.
- The density logging tool is also of similar dimensions to the neutron porosity tool. A ^{137}Cs gamma-ray source is placed in a similar position to the $AmBe$ neutron source.

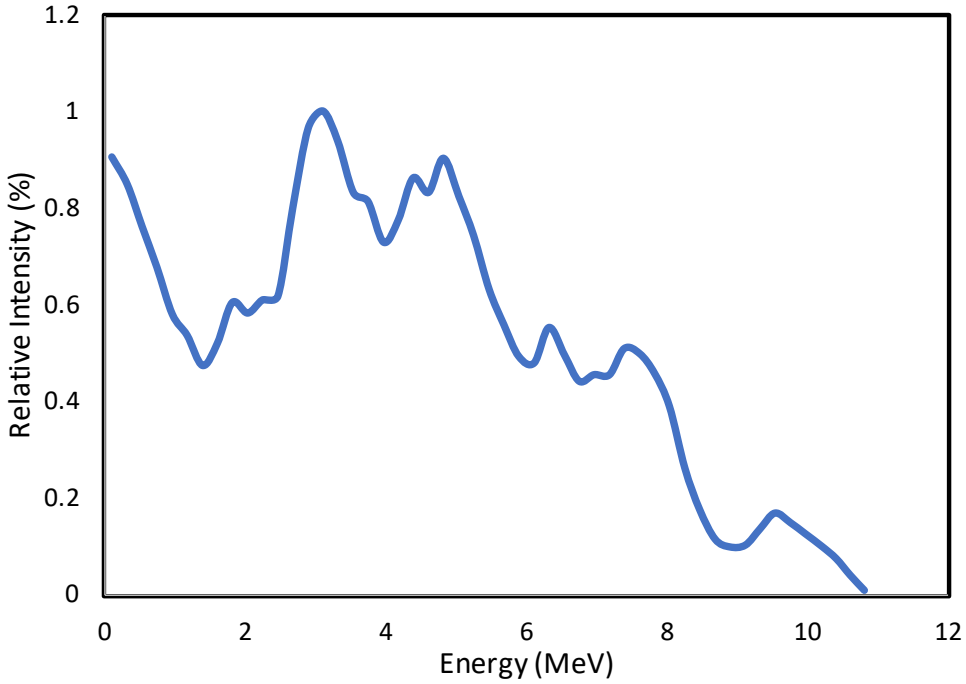

Figure 3.3: Full energy spectrum from $AmBe$ fast neutron source [76].

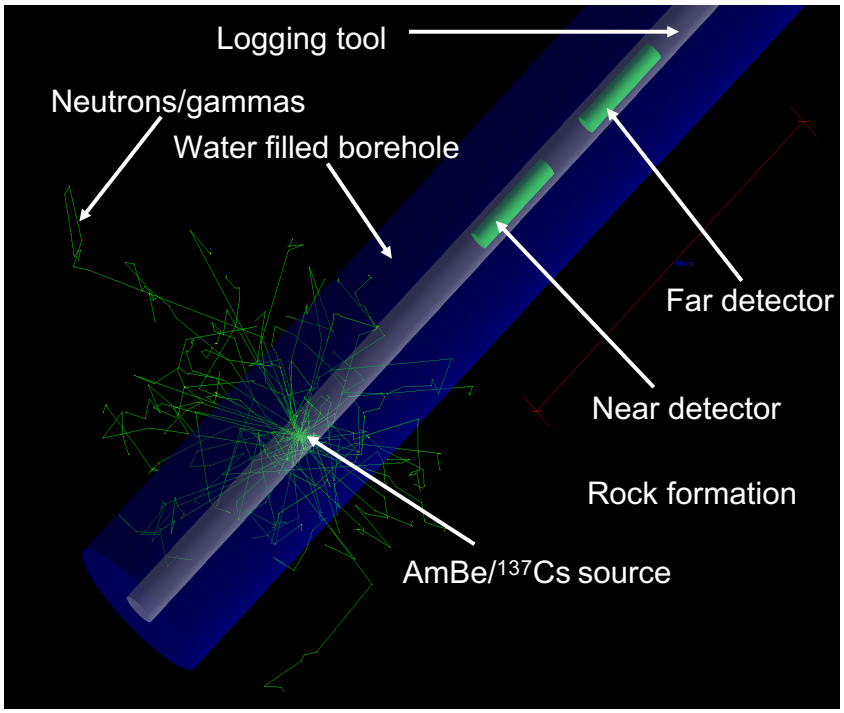

Figure 3.4: Simulated diagram of a logging tool inside an infinite volume of rock formation

Table 3.1: Detectors geometry description and materials

	^{3}He tube	^{10}B-coated straw	^{6}Li-loaded glass	$Eu:LiCAF$
Diameter (cm)	2.54	2.54	2.54	2.54
Tube thickness (cm)	2.54	0.1	2.54	2.54
Converting material	^{3}He	B	Li	Li
Enrichment	99% ^{3}He 1% CO_2	78% B 95% ^{10}B	6.6% Li 95% ^{6}Li	6.6% Li 95% ^{6}Li

3.4 GEANT4 Simulation Results

3.4.1 Detectors Counting Efficiency Comparison

In any of the compared detectors, an event is recorded as a count when both secondary charged particles deposit their total energy within the active volume of the detector. Any event that results in wall effect are ignored. Figure 3.5 shows the total energy deposited in all the four (4) detectors simulated. All the three (3) alternative detectors shows more counting efficiency than the conventional detector.

It worth to note that all spectra presented in this chapter don't incorporate the real energy resolution coming from the number of charge carriers or optical photons produced within the detectors. The delta energy from the simulation is convoluted with 76 keV energy resolution for all the detectors.

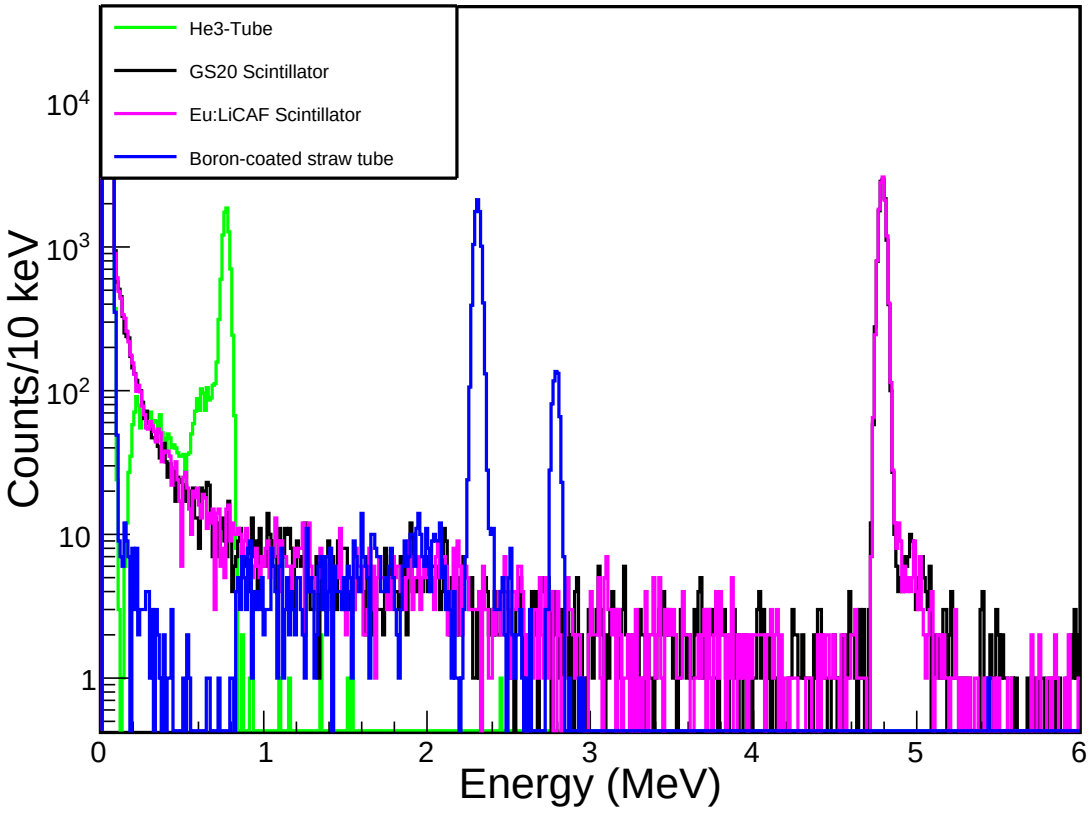

Figure 3.5: Simulated thermal neutron count rates for ^3He tube (green), $Eu : LiCAF$ (pink), ^6Li-loaded glass neutron detectors (referred to as $GS20$) (black) and ^{10}B-coated straw tube (blue) simulated with $AmBe$ fast energy source. Note that, due to having the same reaction mechanism, the $GS20$ data is partially obscured by the $Eu : LiCAF$.

3.4.2 Epithermal Neutrons Sensitivity of $GS20$ Crystal

As the fast neutrons from the AmBe transverse the rock formation volume, not all of it gets fully thermalised. Because the ^{3}He tube is not sensitive to other neutrons with energy greater than the thermal energy range, there will be no contribution from higher energies. Unlike the $^3He(n,p)^3H$ reaction, the $^6Li(n,\alpha)^3H$ reaction has its first resonance at 0.240 MeV. Epithermal neutron contribution will therefore have energy of 0.240 MeV higher than the reaction Q-value. Figure 3.6 shows the contribution due to epithermal neutrons in three different materials (limestone, sandstone and water). In water, because

of the high hydrogen index, nearly all the fast neutrons are slowed to thermal energy range, hence very little contribution from epithermal neutrons was observed. In the case of limestone and sandstone, the slowing down probability is low compared to water. For these materials, epithermal neutrons contribution is evident at 5.02 MeV. A ratio of the thermal to epithermal neutron contributions can translate to the porosity of the rock material under investigation.

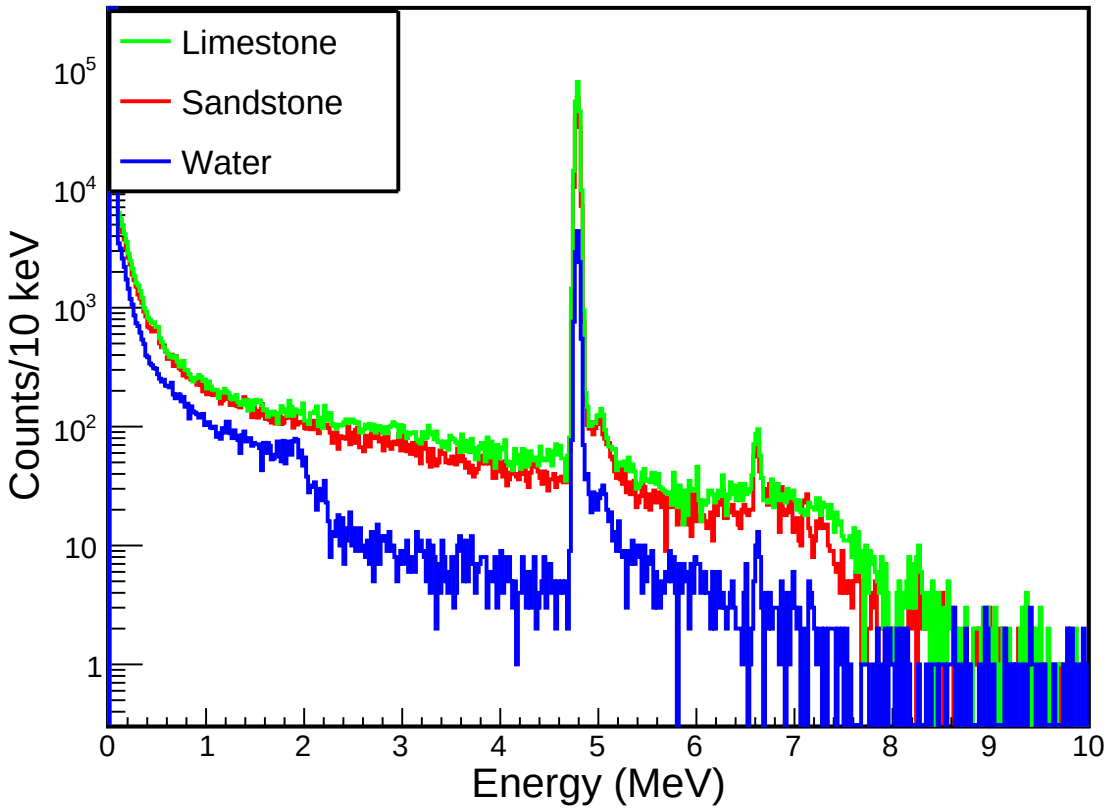

Figure 3.6: Epithermal neutron sensitivity of $GS20$ crystal in limestone (green), sandstone (red) and water (blue) rock formation.

A pronounced peak around 6.6 MeV was also observed although there is no information available in the literature for a second resonance peak from ^{6}Li(n,α)^{3}H reaction. Further simulation to investigate this phenomenon was carried out. As a first step, the near and far detectors were made of just lithium and that wasn't observed, see Figure 3.7. It's obvious

that other elements in the detector material composition such as silicon, aluminium, oxygen etc may be responsible for the observed peak.

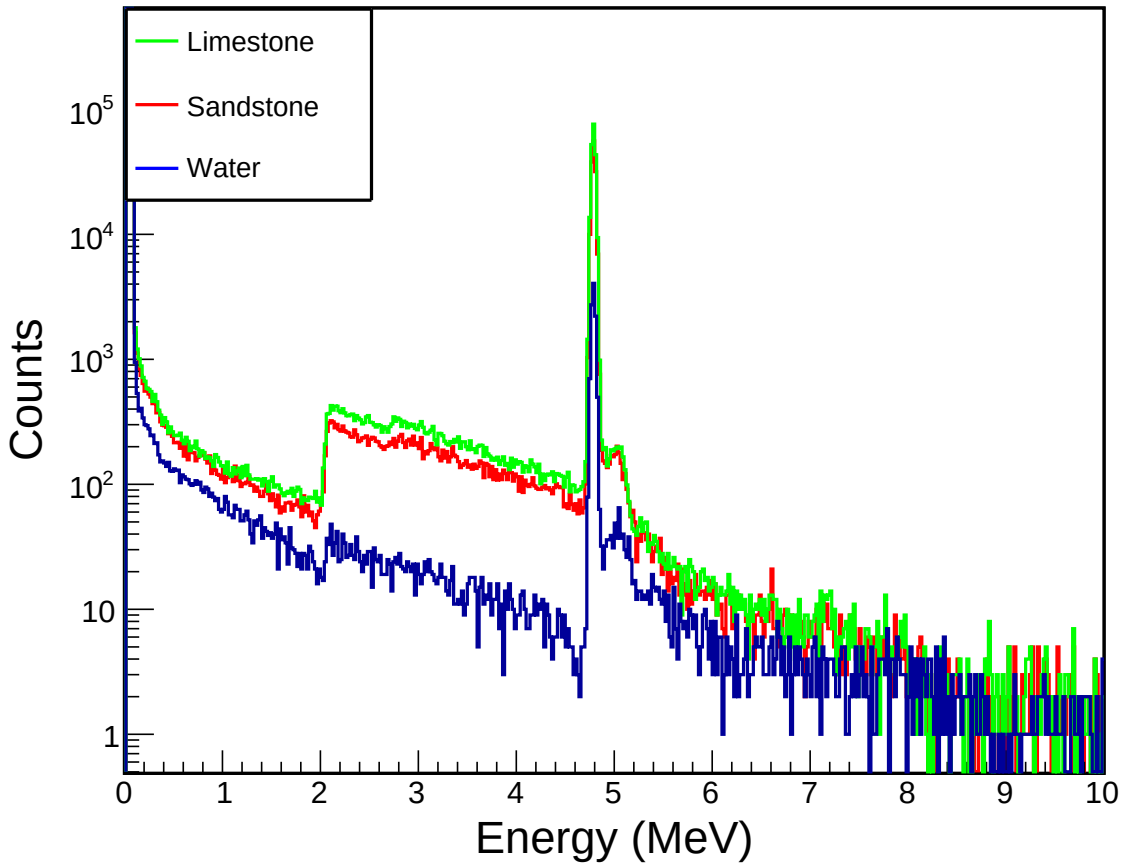

Figure 3.7: Epithermal neutron sensitivity of lithium material in limestone (green), sandstone (red) and water (blue) rock formation.

3.4.3 Pair Production Measurement with $GS20$ Crystal

Density tools utilise Compton scattering of low energy gamma rays produced by a radioactive source as described in chapter 1. During porosity measurements using a fast neutron source and ^{3}He tubes, the fast gammas are not utilised. This led to the use of two separate tools to measure porosity and density. However, the use of $GS20$ has the potential to eliminate the need for multi logging tools. When an $AmBe$ fast neutron source is used,

high energy gamma rays (4.5 MeV) are emitted at a gamma-neutron ratio of 0.575 [77]. Because of its high energy, the dominant interaction mechanism with the rock formation will be pair production. This process occurs when high energy gamma rays interact with matter. When it occurs, the gamma rays are transformed into matter by forming an electron-positron pair. The minimum energy required for it to occur is 1.02 MeV, which is twice the electron rest mass (0.511 MeV). The remaining energy of the gamma rays after creating the electron-positron pairs is giving to the particles in the form of kinetic energy. In most cases, the electron and the positron annihilate after interacting with the detector material and two gamma photons will be produced. When only one of the gamma photon escapes the detector geometry, a single escape peak is observed at 0.511 MeV below the full energy peak. In a situation where both gamma-ray photons end up exiting the detector, a double escape peak will be observed at 1.02 MeV below the full energy peak. Other electrons or positron that get to the detector and do not annihilate, deposit their 0.511 MeV within the detector.

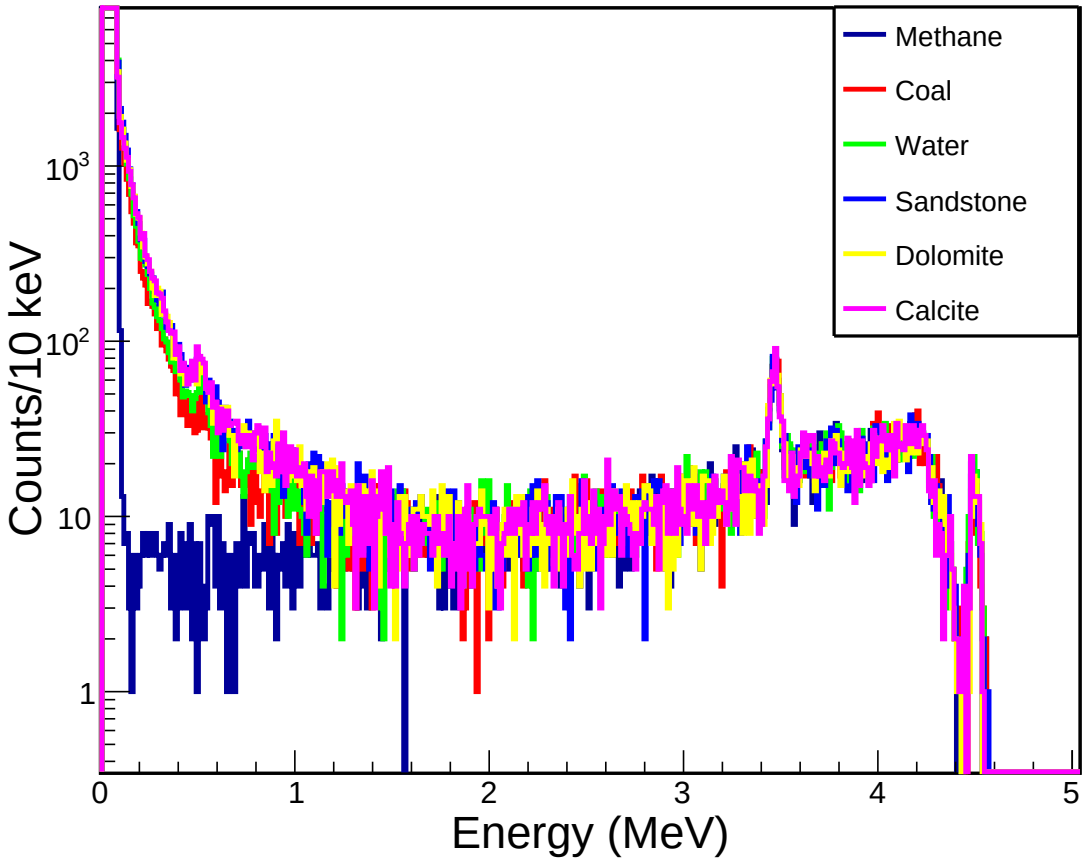

Figure 3.8: Escape peaks as a result of pair production caused by 4.5 MeV gamma rays measured with $GS20$ crystal in a limestone rock formation.

Figure 3.9 shows a spectrum recorded with $GS20$ crystal when a monoenergetic gamma rays of energy of 4.5 MeV are bombarded into coal, water, sandstone, dolomite and calcite materials with 7.09, 7.42, 15.08, 15.65 and 21.42 effective atomic number (effective Z) respectively. Figure 3.9 shows the recorded counts on the 0.511 MeV for each material is plotted as a function of its effective Z. It can be seen that the number of counts increases with increasing effective Z. The blue dots are the near detector counts while the orange dots are the far detector counts. This result shows that by using GS20 crystal only in a logging tool, information about the porosity and density of the rock formation can be estimated.

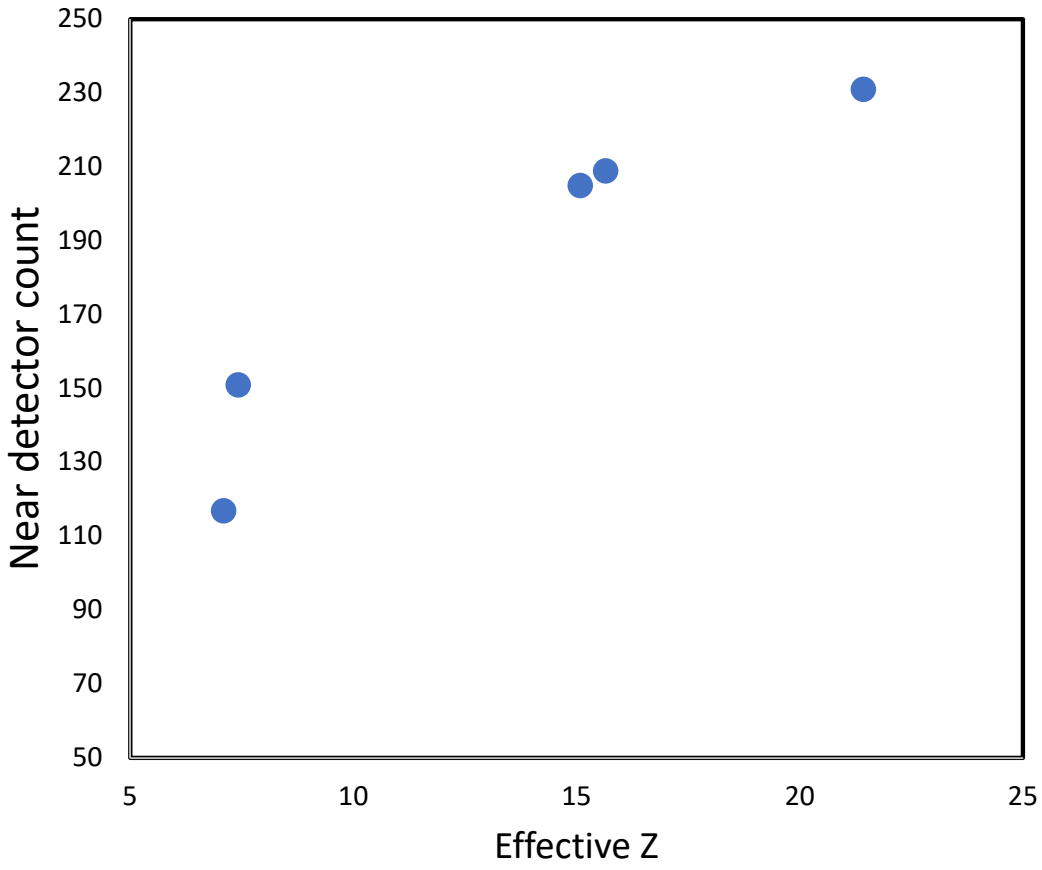

Figure 3.9: Near detector 0.511 MeV counts caused by 4.5 MeV gamma rays measured with $GS20$ crystal in coal, water, sandstone, dolomite and calcite rock formations. The counts increases with increasing effective Z.

3.4.4 Neutron Porosity Measurement

The fast neutrons emitted from the $AmBe$ neutron source undergo scattering with the nuclei of the atom present in the rock formation. The distance travelled by a neutron depends on its energy and the type of material present in the rock formation. Low-Z materials like hydrogen slows down fast neutrons more rapidly. Several elastic collisions will get the fast neutrons to thermal and epithermal energy regime. These low energy neutrons eventually diffuse back into the detector(s). The count rates recorded by each detector depends on the volume of water or hydrocarbon in the rock formation pore spaces (regions occupied by fluid). High count rates are recorded in less porous rock formation, while

rock formation with more pore spaces provide low count rates. This is because hydrogen atoms present in the water or hydrocarbons absorbs most of the thermal neutrons. These phenomena is illustrated in Figure 3.10. This figure presents count rates recorded with ^3He thermal neutron detector and GS20 crystal of similar geometry in a limestone formation with the porosity varied from 0-50% porosity unit (a unit equal to the percentage of pore space in a unit volume of rock). Porosity is derived from the ratio of counts between the near and far detector. Environmental effect such as salinity, mud composition and temperature are reduced by the taking the ratio between the two detectors.

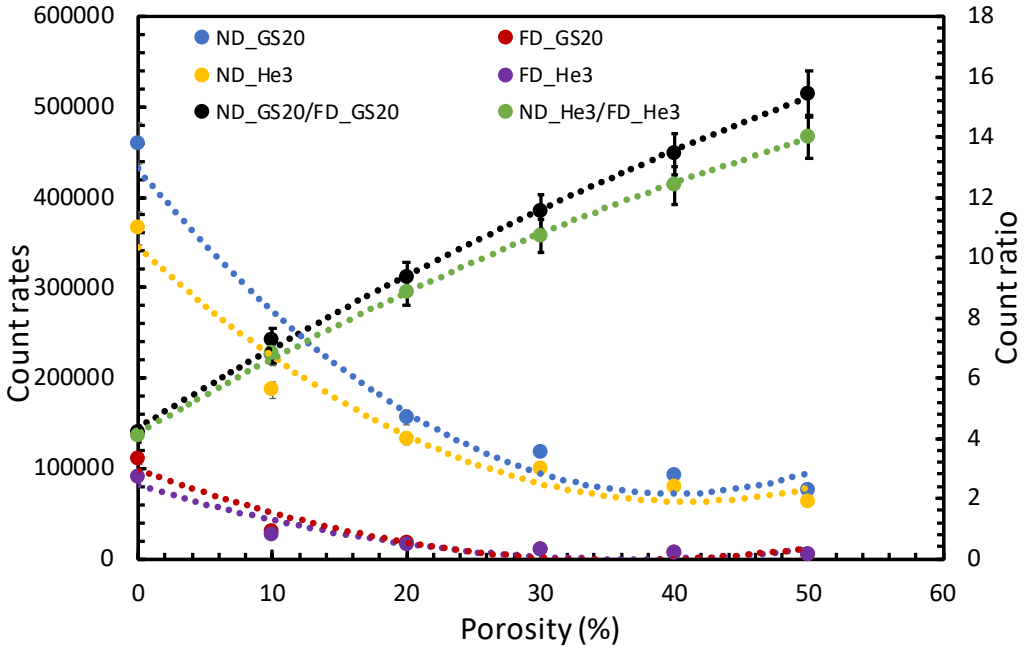

Figure 3.10: Simulated near and far detectors count rate as a function of the porosity (%) with ^3He detector (yellow and purple dots) and $GS20$ (blue and and red dots. The secondary axis shows the near and far detector count ratios in black and green dots for $GS20$ and ^3He respectively. The dotted lines are 2nd order polynomial fit to the data

3.4.4.1 Effect of Borehole Size

Boreholes are usually filled with fresh water, the size of the borehole will therefore have a greater impact on the tool response. The impact borehole size on count ratio decreases with increasing porosity. To study this effect, the borehole size was varied between 2.5

cm to 17.5 cm in radius in a homogeneous mixture of limestone rock and water formation for each porosity unit (0-50%). Figures 3.11 and 3.12 show the effect borehole size as a function of porosity for ^3He and $GS20$ respectively. At 100% porosity, all count ratios converge irrespective of the borehole size. The dotted lines on both plots are second order polynomial fits. The constants from these fits can be used to correct for the effect of borehole size.

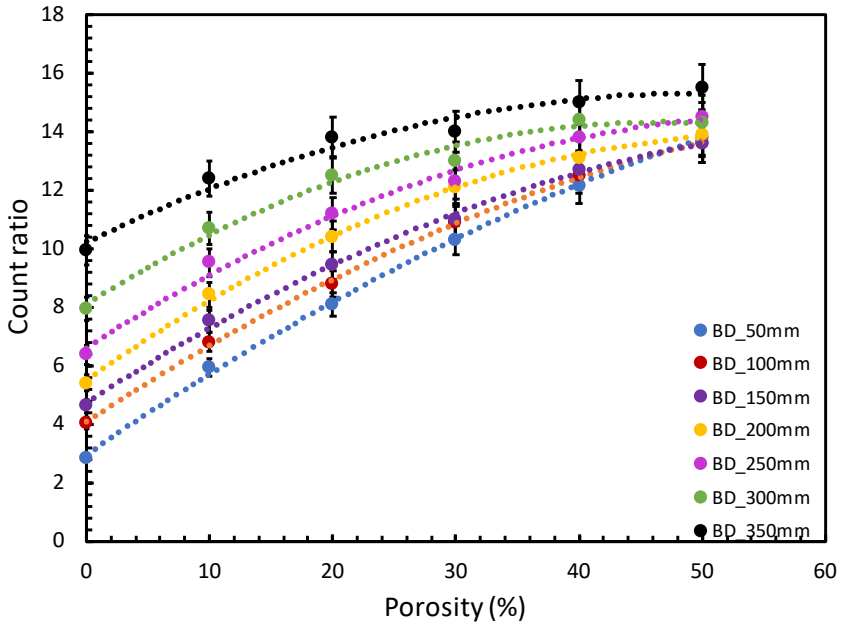

Figure 3.11: Effect of borehole diameter to the near and far detector count ratio as a function of the porosity (%) simulated with ^3He detector for a diameter range between 50 to 350 mm in limestone rock formation.

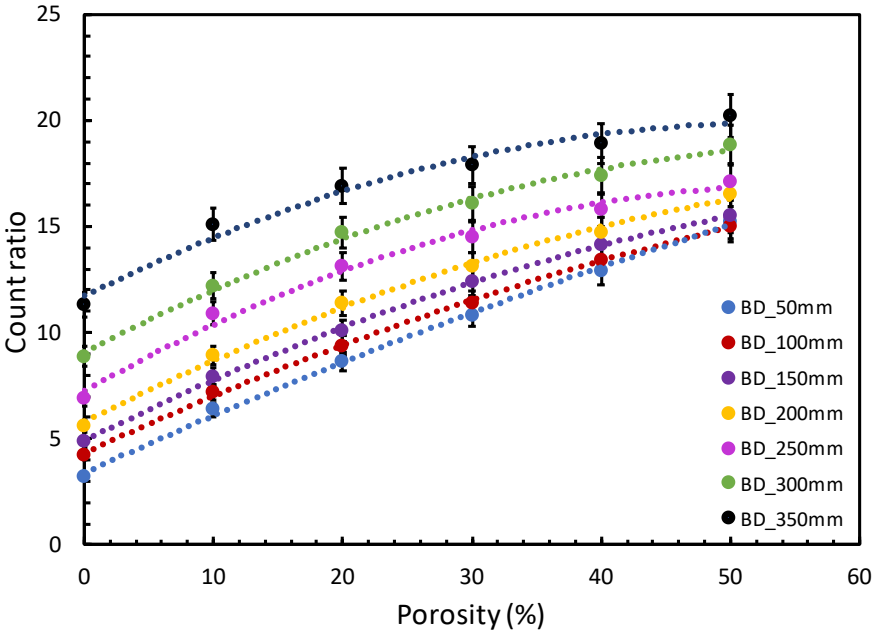

Figure 3.12: Effect of borehole diameter to the near and far detector count ratio as a function of the porosity (%) simulated with *GS*20 detector for a diameter range between 50 to 350 mm in limestone rock formation.

3.4.4.2 Effect of Lithology

Different materials have different densities and hence contribute differently to the detector response. In order to study the effect of rock formation materials on detector count rates, series of simulations were carried out with the rock formation material defined to be coal, limestone and sandstone. The simulations were made with both ^{3}He tube as well as the *GS*20 crystal. Figures 3.13a and 3.13b show the near and far detectors count ratios recorded with ^{3}He tube and GS20 crystal, respectively. Because of the very high hydrogen content in coal, the effect of porosity was minimal. The count ratio obtained with both detectors is almost linear as compared to the other materials (limestone and sandstone). Sandstone and limestone have similar density hence the similar count ratios. One important thing to note is the statistical fluctuation, which is more for the ^{3}He tube detector data in Figure 3.13a as compared to GS20 crystal measurements presented in Figure 3.13b.

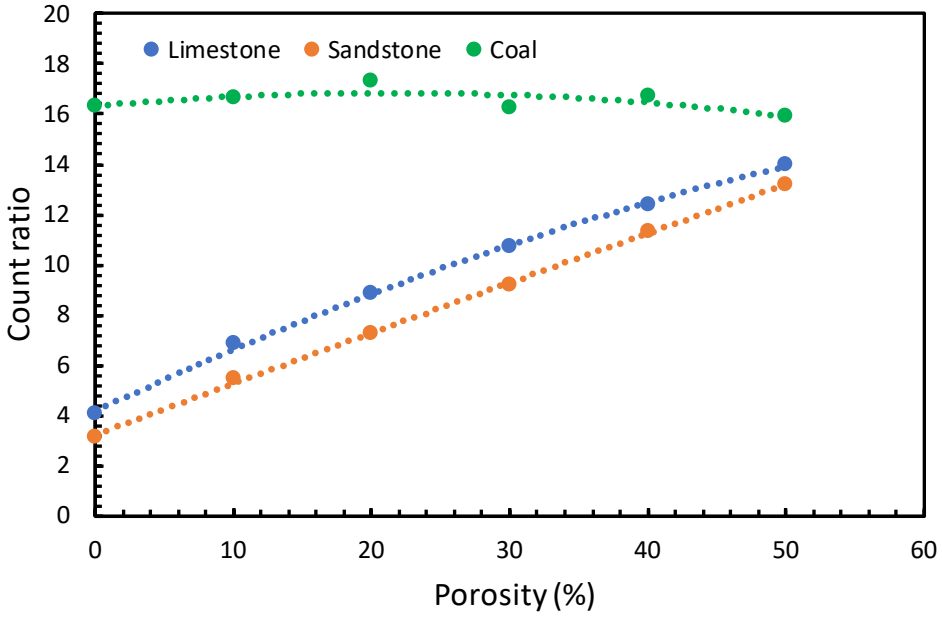

(a)

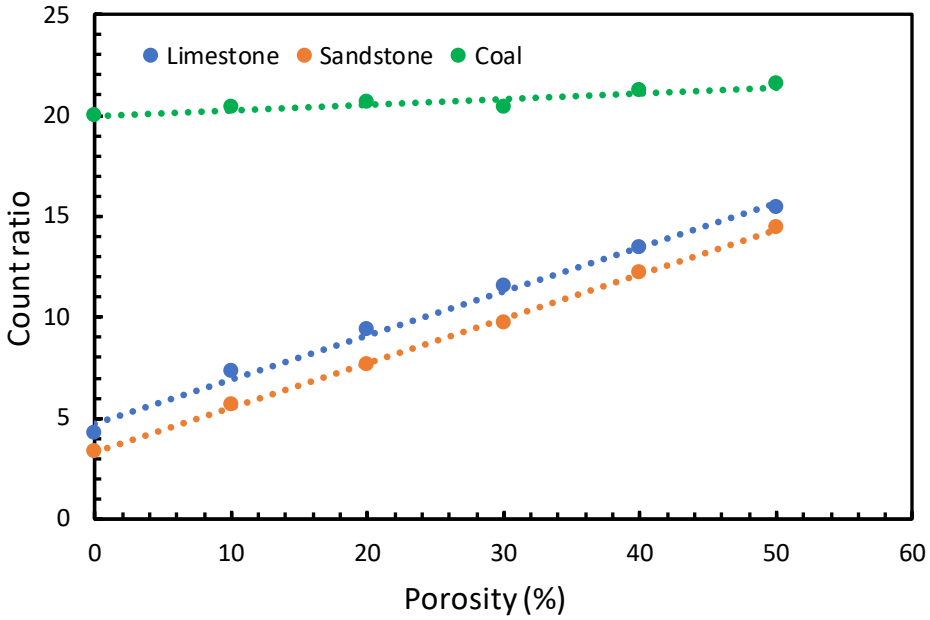

(b)

Figure 3.13: (a) Effect of lithology as a function of porosity with ^3He thermal neutron detector in a limestone formation. (b) Effect of lithology as a function of porosity with $GS20$ crystal in a limestone formation.

3.5 Neutron-gamma Measurements

In this type of measurement, the rock formation is bombarded by fast neutrons emitted from a fast neutron source. These fast neutrons undergo several inelastic interactions as a result excite the nuclei present in the rock formation which subsequently de-excite by emitting a characteristic γ rays. After several collisions, the fast neutrons lose a lot of energy and form a cloud of thermal neutrons. These low-energy neutrons are absorbed/-captured by the nuclei present and as a result, a γ ray of characteristic energy is emitted. The spectra from these interactions are recorded by a high precision γ-ray detector. Figure 3.14 present the simulated inelastic/captured γ rays in a porous (10% PU) limestone and a sandstone rock formation using a GS20 crystal. These low energy neutrons are captured not only by the rock formation and its pore fluids, but also the tool material. Both rock materials are simulated to contains 10% porosity, thereby increasing the hydrogen content which subsequently result in the release of 2.22 MeV captured γ rays following proton neutron interaction. The 0.5 MeV due to pair production by high energy γ rays and subsequent annihilation of positrons is also common to both rocks. The 7.64 MeV from iron of the tool body is clearly resolved. Neutron capture by silicon in the sandstone rock formation evident by the 3.54 and 4.93 MeV γ ray peaks. Although we couldn't resolve with certainty the carbon and calcium signatures in the limestone rock formation, which could be due to low statistics, however, one can see clear differences between both rock types. To study the sensitivity of GS20 to captured/inelastic γ rays, we compare the performance of this detector to that of the conventional γ-ray detector (NaI:Tl) in the oil industry. Figure 3.15 presents an overlaid spectra from GS20 and NaI in limestone rock formation with 10% porosity. Worth to know that the energy resolution of GS20 in reality is worst than that of NaI:Tl scintillator and that the light yield of GS20 is only about 20% of NaI:Tl.

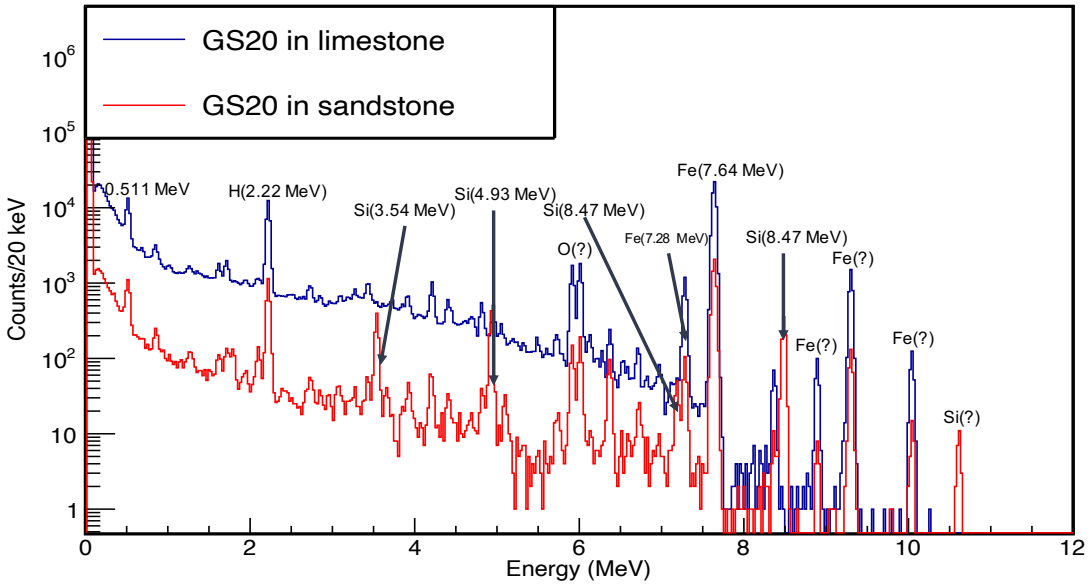

Figure 3.14: Captured/inelastic gamma rays from limestone and sandstone as simulated with $GS20$ crystal

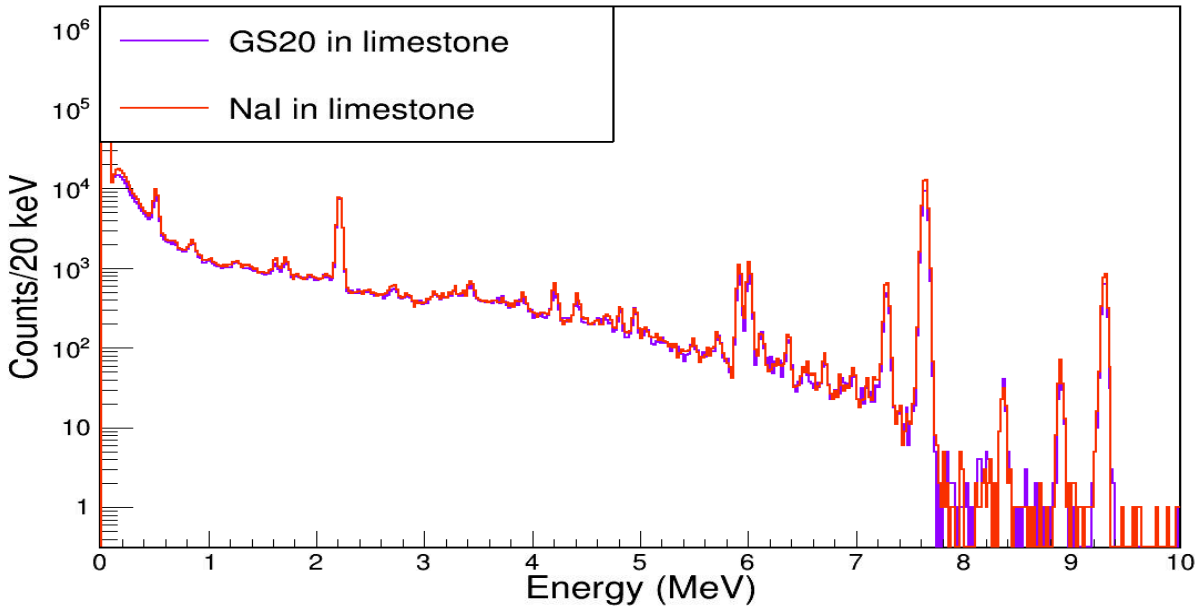

Figure 3.15: Captured/inelastic gamma rays from limestone as simulated with $GS20$ and NaI crystals. The energy resolution used for both detectors correspond to that of NaI. In reality the energy resolution of $GS20$ is worst.

The modelled tool and results presented in this chapter relates to a new neutron porosity tool to be used by Robertson Geologging Company and will be used for their data analysis such as borehole size corrections and tool calibration.

3.6 Conclusion

The simulation results presented above has demonstrated how an alternative radiation detector ($GS20$ crystal) can replace ^3He tube in thermal neutron detection and $NaI:Tl$ crystal in captured/inelastic gamma ray measurements for lithology identification during logging activities. The response of $GS20$ to effect of rock formation porosity, effect of borehole size and lithology effect has been compared to that of ^3He tube. In all of these, the $GS20$ crystal has shown to have a comparable response to ^3He tube. Additionally, the advantage of this crystal over the conventional neutron detector in epithermal neutron detection capability has also been presented. This capability also shows how epithermal neutron contributions can differentiate between hydrogen reach rock formation and non-hydrogen reach rock formation. Moreover, it has also been shown how the ignored high energy gamma rays from AmBe fast neutron source when used in neutron porosity tool can provide useful information about the density of the rock formation. Finally, the captured/inelastic gamma ray sensitivity of $GS20$ has been demonstrated in comparison to $NaI:Tl$.

Chapter 4

Neutron and Gamma ray Pulse Shape Discrimination

Many scintillation materials as described in Chapter 2 are sensitive to a mixed neutron and gamma-ray radiation fields. This chapter presents the thermal neutron, fast neutron and gamma ray pulse shape discrimination analysis using cesium lithium lanthanum bromide ($CLLB$), cesium lithium lanthanum bromide chlorine ($CLLBC$) crystals. The selection of these crystals was due to availability in the lab as at the time of this work. Section 4.2 provide an overview of pulse shape discrimination analysis. Section 4.3 describes the different methods used to achieve pulse shape discrimination. Section 4.4 provides details of the experimental setup and section 4.5 provide the results and discussion.

4.1 Introduction

Borehole logging like many other applications, is one in which mixed neutron and gamma-ray radiation fields is involved especially when AmBe neutron source is the source of fast neutrons. These applications have gained slow but steady development and interest starting with the investigation into the dual capability of organic scintillators in the 1950s [78–80] to glass scintillators and organic plastic scintillators 1960s [81–83] to the recent

semiconductor detectors [84] and more recent elpasolite and new generation detectors [85–87] in 2000s. CLLB and $CLLBC$ are elpasolites family of inorganic scintillators with the same crystaline structure. Elpasolites are unique radiation detection materials because of their dual capability, high light output and excellent proportionality which provide them with excellent spectroscopic abilities. They also have good thermal neutron detection efficiency via ^{6}Li(n,α)^{3}H capture reaction.

The main aim of this chapter is to demonstrate how neutron-gamma pulses could be distinguished when a dual particle detector is used in a mixed radiation field. Different types of pulse shape discrimination analysis method are used to achieve this.

4.2 Pulse Shape Discrimination Analysis

In inorganic scintillators, the electrons within the energy levels of the crystals are excited upon the the absorption of radiation energy as explained more detailed in Section 2.2.2.2. As reported by [88] and the references therein, impurities such as Ce and Tl are the main components in the scintillation process in inorganic scintillators through which self-absorption of emitted light can be minimized. The response of a scintillator depends on its type as well as the radiation it is measuring. This implies that different ionizing radiations have different rates through which they loss energy, this therefore makes their scintillation process different. This characteristics is the basis for pulse shape analysis which has been in use since 1950s as reported by [88] and the references therein.

4.3 Types Discrimination Method

4.3.1 Pulse Height Analysis (PHA)

The intensity of scintillation photons produced in either crystal is different depending on the interacting radiation (neutrons or gamma rays). Like many other elpasolites, the scintillation light produced by electrons as a result of gamma rays either crystal is less than

the the scintillation light produced by the charged particles produced as result of neutron interaction. Thus, one can easily discriminate between these two (2) types of radiation by comparing their generated electrical pulses [88].

4.3.2 Pulse Gradient Analysis (PGA)

Pulse gradient analysis (PGA) is a method used in discriminating between neutrons and gamma rays which utilises the principle that the scintillation light produced as a result neutron and gamma ray interactions decays differently depending on the interacting material. In CLLB and $CLLBC$, the neutron interaction has a faster decay time as compared to the interaction caused by gamma rays. In other scintillating materials like organic liquid scintillator, the situation is reversed with the the gamma ray having faster decay time [89]. The peak amplitude in comparison to the amplitude of a sample occurring a specified time later is used as a means of pulse discrimination using this method.

4.3.3 Charge Comparison Method (CCM)

While the pulse height analysis (PHA) compares the height of the integrated generated electrical pulses, charge comparison method (CCM) utilises the fact that each pulse decay within a different time interval depending on the type of radiation that resulted in the production of such pulses. The time it takes for a pulse to be generated by gamma ray interaction to decay is longer in $CLLB$ and $CLLBC$ than the time it takes a pulse generated by neutron interaction to decay. Discriminating between neutron and gamma rays using this method can be achieved by setting two time gates. Here, the ratio between the integrated charge in the long component (Q_{long}) and the integrated total charge (Q_{total}) as shown in figure 4.2 is used to discriminate between neutrons and gamma rays. This can can be expressed as:

$$PSD = \frac{Q_{long}}{Q_{total}} \tag{4.1}$$

4.4 Experimental Setup

The $CCLB$ and the $CLLBC$ used in this experiment are both supplied by Kromek. The $CLLB$ has a dimension of 1" X 2" and is encapsulated in an 0.5 mm thick aluminium housing to shield it from moisture as it is hygroscopic. In between the housing and the crystal is filled with a diffusive material. A 5 mm window is coupled to a 1" PMT to collect the scintilation light produce in the crystal. The $CLLBC$ is a 0.5 cm cube which is also housed in an aluminium housing because it is also hygroscopic. The readout window of the $CLLBC$ was coupled to a 6 X 6 mm^2 SiPM. An AmBe fast neutron and ^{137}Cs gamma ray sources were used to produce fast neutrons and gamma rays respectively. The characteristics of the AmBe fast neutron source are presented in Table 4.1. The measurements were carried out in the neutron shade (a small room) located outside the main physics building at the University of York.

The $CLLB$ was powered by Ortec 556 power supply while the $CLLBC$ was powered by a CAEN DT5485P digital power supply. The anode of each detector is individually connected to an 8 channel, 14 bit at 500 mega sample per second digitizer to record the raw pulses with a wavedump software install on a laptop. 15000 raw pulses were recorded in each case at a trace length of 14000. The recorded pulses were transferred to a Linux based computer for pulse shape discrimination analysis. The setup is shown in figure 4.1

Table 4.1: Table of data for University of York AmBe neutron source.

Position description	**Neutron dose** ($\mu Sv/hr$)	γ **dose** ($\mu Sv/hr$)
In contact with the container (at port height)	6	2
In contact with top of the polyethylene lid	3	-
In contact with bean port (plugs in place)	6	-
Beam port (outer and inner plug removed) in contact	10	5
Beam port (outer and inner plug removed) at 50 cm	2	-
Beam port (outer and inner plug removed) at 100 cm	<1	-

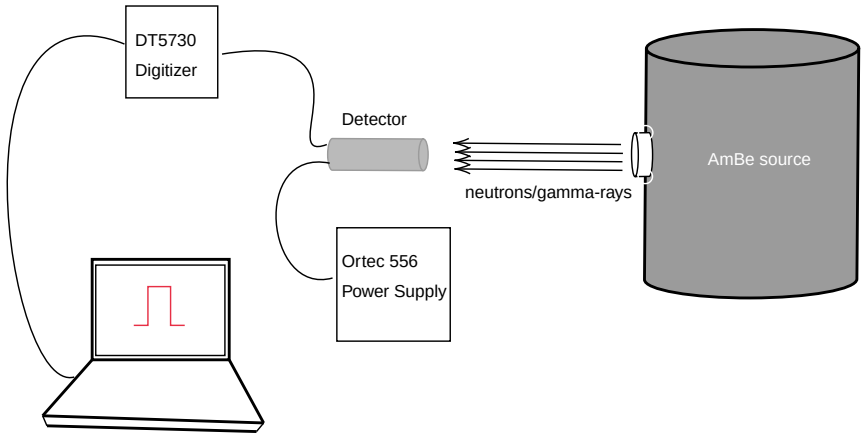

Figure 4.1: A schematic of the experiment setup and the AmBe fast neutron source.

4.5 Results and Discussion

A single raw pulse which could be due to either radiation interaction with the $CLLB$ crystal is shown in figure 4.2. As explained above, both pulses generated by either neutron

or gamma rays decays at a different time constant. The charge comparison method was used by setting a different time gates manually within my analysis code to discriminate between both particles. Both pulses have a similar rise time between 2-3 μs. Figure 4.3 shows the average pulse shapes measured for neutron and gamma rays using $CLLB$, normalised to an amplitude of unity. The figure shows the normalised average neutron neutron pulses in blue while the normalised gamma ray average pulses are seen in red.

The photons emitted by the $CLLB$ upon neutron absorption yield an electron equivalent energy of 3.2 MeVee, which correspond to the reaction Q value of 4.78 MeV. A measurement made in the presence of AmBe fast neutron source and a ^{137}Cs gamma ray source, as can be seen in the energy histogram presented in figure 4.5. The pulse shape discrimination parameter defined in equation 4.1 is plotted against the energy presented as pulse height in figure 4.4. The 662 keV gamma ray peak from ^{137}Cs and the 3.2 MeV electron equivalent energy are clearly distinguishable.

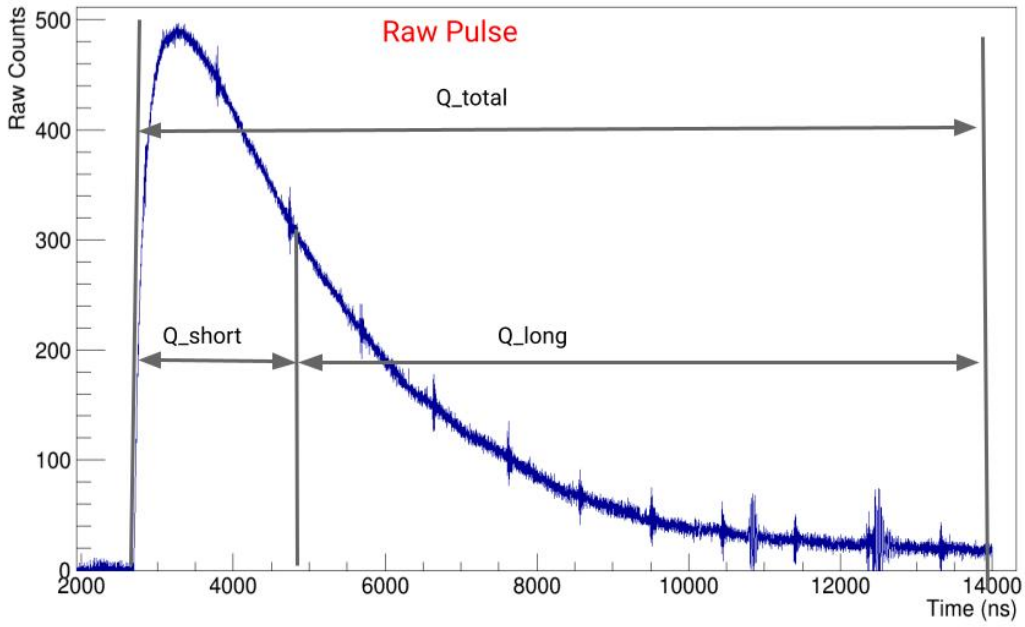

Figure 4.2: Raw waveforms pulses from gamma and neutron interactions in $CLLB$. The spikes at regular distance arise from the detector connector which grounding couldn't take care of.

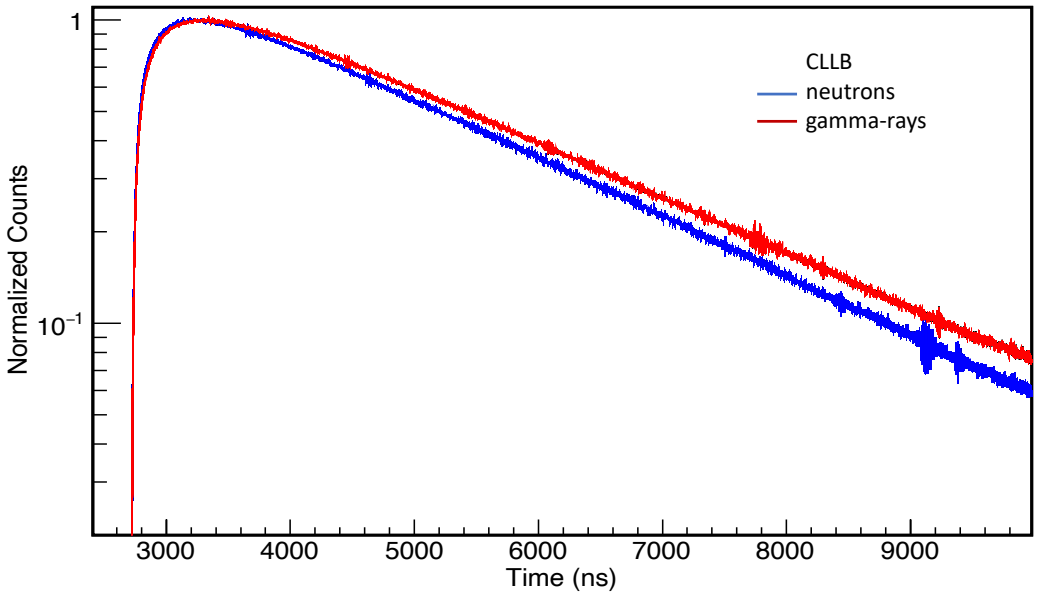

Figure 4.3: Normalised waveforms from gamma (red, top curve) and thermal neutron (blue, middle curve) interactions in $CLLB$.

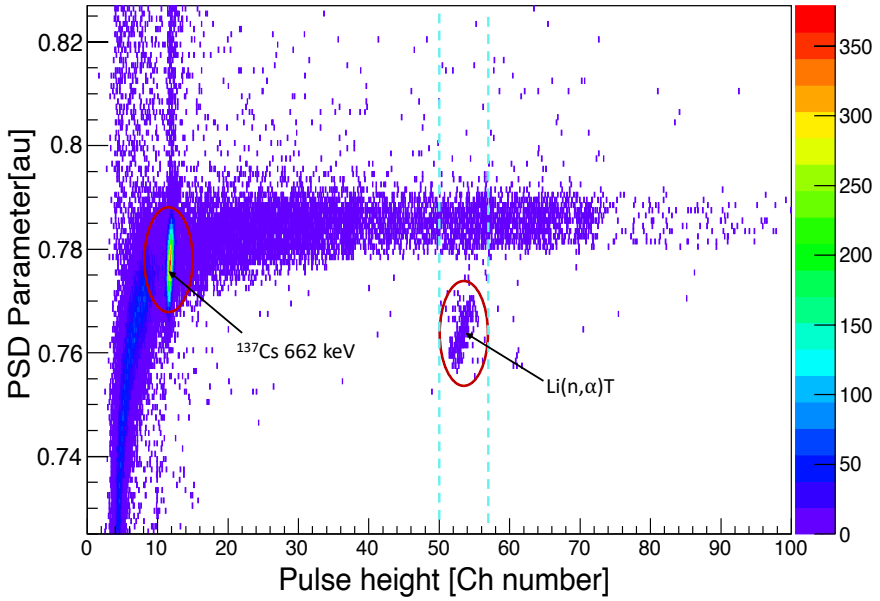

Figure 4.4: PSD in $CLLB$, showing a distinct gamma band with higher Q_delayed/Q_total ratio and thermal neutron interactions with lower ratios.

A common common method used to evaluate the discrimination capability of any dual detector is the Figure of Merit (FoM). It is obtained from the probability distribution of the PSD method adopted. It tells how well the two particles events under investigation are well separated. It takes the ratio of the separation between the centroid of the two peaks to the sum of the FWHM of both peaks as described illustrated by the below equation:

$$FoM = \frac{\Delta}{\Delta_\gamma + \Delta_n} \tag{4.2}$$

Where Δ is the separation between the centroid of the two peaks, Δ_n is the Full Width at Half Maximum (FWHM) of the neutron peak and Δ_γ is the FWHM of the gamma peak.

To evaluate the pulse shape discrimination ability of $CLLB$ crystal, an energy cut around the 3.2 MeVee and the low statistic tail of the high energy gamma rays is used as shown in cyan from figure 4.4 above. The resulting spectrum is presented in figure 4.6. A FoM of 1.4 is obtained, which is good separation. Alternatively, one could also set an energy cut between the 3.2 MeVee and the 662 keV which has more statistics.

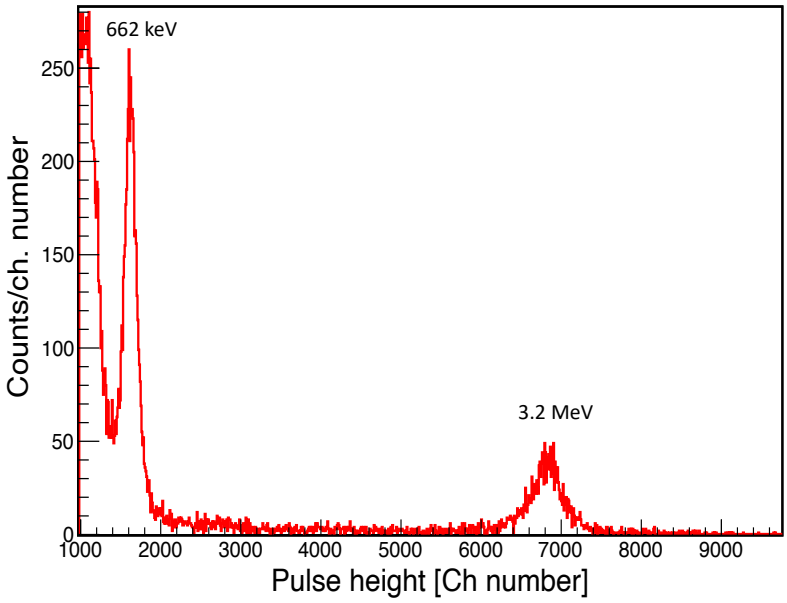

Figure 4.5: $CLLB$ energy spectrum showing gamma lines from ^{137}Cs and thermal neutrons from moderated ^{241}AmBe.

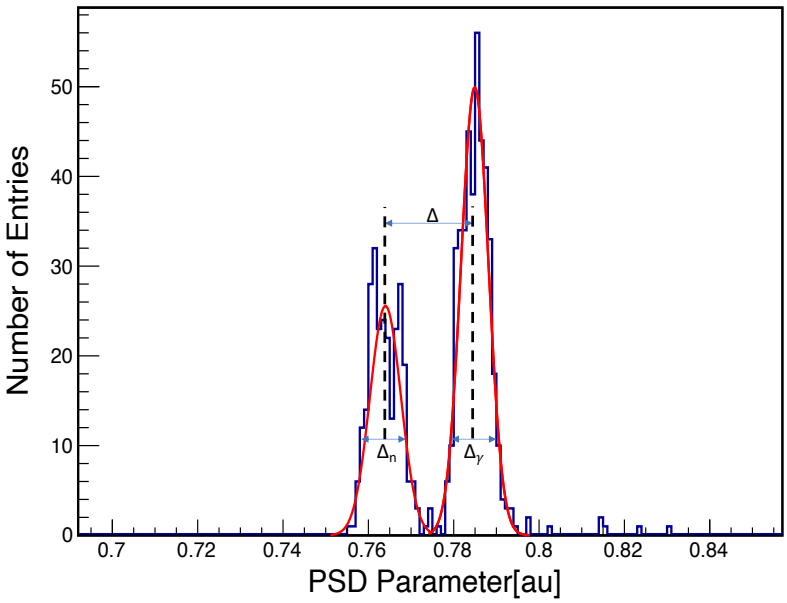

Figure 4.6: The distribution of PSD parameters for neutrons and gamma rays.

Another measurement made with a polyethylene (HDPE) cylindrical block placed in between the detector and the fast neutron source is shown in figure 4.7. The energy spectrum shows 662 keV from ^{137}Cs and 2223 keV from neutron capture on hydrogen in the moderating material (HDPE). A similar result was presented in [63] for comparison. The thermal neutron electron equivalent energy range and that of alphas can be seen to extend from 25000-37000 channel number which will roughly correspond to an electron equivalent energy between 2-4.2 MeVee.

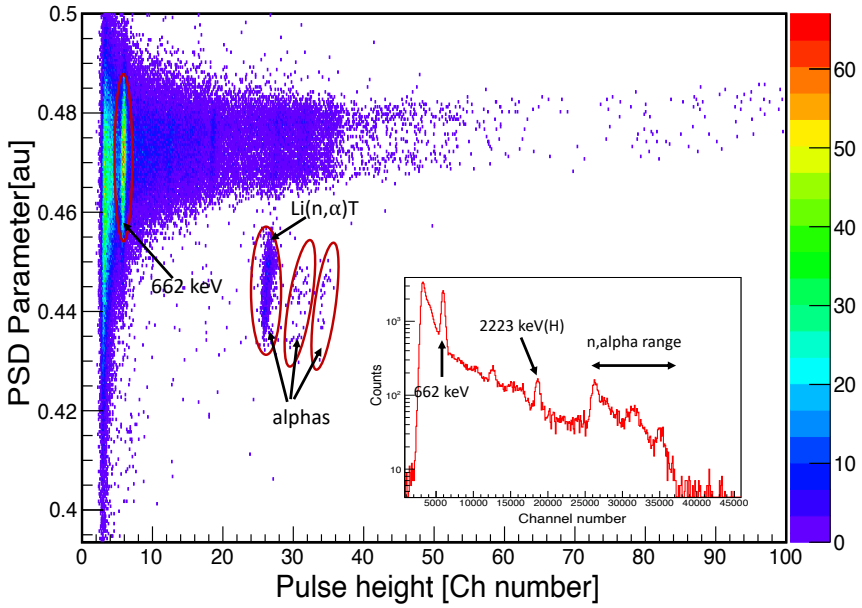

Figure 4.7: PSD in $CLLB$, showing a distinct gamma band with higher Q_delayed/Q_total ratio and thermal neutrons and alphas interactions with lower ratios.

Unlike $CLLB$, $CLLBC$ because of the presence of chlorine, is sensitive to fast neutron via $Cl(n,p)S$. Although we are limited to very high statistics because of the source strength, the contribution due to fast neutron interaction with chlorine in the $CLLBC$ is observed as can be seen in figure 4.8.

Recall, one of the specification as pointed in the project goal is for the dual detector to have a good pulse shape discrimination capability. Although GS20 was used in the simulation comparison, this was not possible for the experiment because the intended GS20 to be purchased by the University couldn't be achieved at the end. On note, CLLB and $CLLBC$ crystals were used to show how these particles can be discriminated. This is particularly useful for the logging industry as these crystals have the potential to be as dual particles detection technology, thereby eliminating the engineering and cost effect of having to design two separate tools for thermal neutron and gamma ray detection.

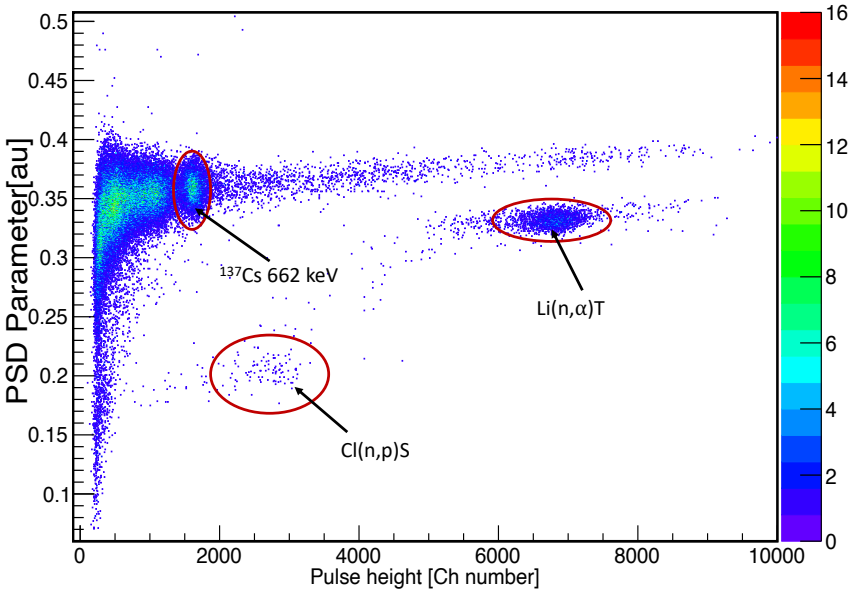

Figure 4.8: PSD in *CLLBC*, showing a distinct gamma band with higher Q_delayed/Q_total ratio and thermal neutron interactions with lower ratios.

4.6 Conclusion

The pulse shape discrimination capability of *CLLB* and *CLLBC* crystals using charge comparison method has been demonstrated. It has been shown that the pulses generated due to gamma ray interaction decays at a later time compared to those generated due to neutron interaction. A FoM of merit of 1.4 was obtained from an energy cut around the 3.2 MeVee from neutron interaction and a cut from the low statistics gamma ray tail corresponding to similar electron equivalent energy.

Chapter 5

SiPM High Temperature Characterisation

Temperature sensitivity is a key parameter for photo-sensors which might be coupled toscintillators and used in borehole logging. This chapter is aimed at demonstrating the suitability of modern silicon photomultiplier (SiPM) technology to replace the conventional photo-sensor (PMT). This will provide benefits like reducing the form factor as well as high voltage requirements. Section 5.1 briefly reintroduces the concept well logging. Section 5.2 describes the selection criteria of a detector material and choice of photo-sensor. Section 5.3 presents the results obtained and lastly, section 5.4 describes a temperature compensation power supply followed by a conclusion.

5.1 Introduction

High temperature encountered during borehole logging is one very important parameter that limits the performance of scintillators and a photo sensors. As explained in Chapter 1, due it's ruggedness, PMT is the conventional photo sensor used in this application and many other societal applications. Several disadvantages has however been pointed out in the same chapter. An alternative photosensor which is more compact would be of

high interest in this application. An attractive replacement technology consists of silicon photomultipliers (SiPMs). These devices have been revolutionary in medical imaging applications [24–28] and are finding wider application in experimental nuclear physics as well as related societal applications. SiPMs are robust and have a small form factor. Unlike PMTs, they do not need a high voltage. In recent years, a number of manufacturers have made advances in this technology resulting in higher gain, lower Dark-Count-Rate (DCR), reduced cross-talk and after-pulsing, as well as reduced temperature sensitivity. These devices now present the possibility of creating a new generation of compact, low-voltage detectors for the borehole logging application.

In this work, we report on efforts to develop a SiPM-based detector suitable for replacing existing PMT-based gamma detectors in use by the borehole logging industry. The initial focus is on a detector which is capable of operating at 75 ℃ which is the maximum temperature found in the least-demanding borehole operations and should be in reach of the stated maximum temperature range of commonly available SiPMs.

5.2 Choice of detector materials

Critical to this study is the choice of appropriate materials to form the prototype detector. Accordingly, we initially discuss the motivation for the selection of the scintillator crystals and SiPMs to be studied.

5.2.1 Choice of scintillator for high temperature operation

Inorganic scintillator crystals are generally robust materials which have a relatively high melting point far above temperatures considered in borehole logging. In this sense, a wide range of crystals might be suitable for the present application. The standard material currently in use is *NaI:Tl* which is the most commonly found inorganic scintillator in industrial applications, and is inexpensive. The crystal of choice should ideally have good proportionality, strong scintillation emission and a suitable wavelength matching to typical

SiPMs. One option would be the next-generation scintillators such as $CeBr_3$ and $LaBr_3$:*Ce* which have excellent proportionality and high light emission. However, these materials are prohibitively expensive making them unsuitable for such an industrial application, particularly when energy resolution is not of utmost importance. A more practical choice are cesium iodide-based scintillators which come in two common variants: *CsI:Tl* and *CsI:Na* having peak emission wavelengths of 550 and 420 nm, respectively. They are slightly more expensive than *NaI:Tl* and have similar light emission properties to to *NaI:Tl*, though with significantly longer decay times (1000 ns and 630 ns respectively, compared to 230 ns for *NaI:Tl*). *CsI:Tl* has the advantage of being only slightly hygroscopic so does not require the same canning necessary for many scintillator materials allowing direct coupling to SiPMs to be explored potentially leading to better scintillation light collection.

As the detectors are to be operated at elevated temperature, the change in their light output as a function of temperature becomes a relevant consideration. If such crystals become brighter at the temperatures considered in this application then the improved photon statistics may at least partially offset the disimprovement associated with the SiPM performance at elevated temperature — an issue to be discussed in more detail below. For many common scintillators, light output is known to decrease with increasing temperature, while for others, it increases, for example, some authors have reported an increasing light output for *CsI:Na* [90, 91] peaking at ∼80 ℃. This would be of particular interest for the borehole logging application as 80 ℃ is within the typical operating temperature range, however it should be noted that the data cited are at odds with contemporary data sheets from Saint Gobain Crystals which indicate that both *CsI:Tl* and *CsI:Na* exhibit maximum light output at ∼30 ℃ [92]. These considerations motivated the choice of *CsI:Tl* and *CsI:Na* as the crystals to be investigated in this study.

5.2.2 Choice of silicon photomultiplier

The success of silicon photomultipliers has resulted in a number of new manufacturers, namely KeteK, AdvanSiD, First Sensor and Excelitas, in addition to the more established

Hamamatsu and SensL. Though SiPMs exhibit significantly less temperature sensitivity when compared to photodiodes and avalanche photodiodes (APDs), they are far from immune to temperature effects. The principal effect is the increase in breakdown voltage with increasing temperature. If a constant bias voltage is used, this manifests as a reduction in peak height due to the reduction in over-voltage (i.e. $V_{over} = V_{bias} - V_{breakdown}$) which leads to a reduction in gain with temperature. For small temperature changes this will degrade the energy resolution as the photopeak is broadened, however, for large temperature changes a significant peak shift will be observed. This can be mitigated by adjusting the bias voltage as a function of temperature.

An additional concern is the increase in Dark-Count Rate (DCR) with increasing temperature characterised by the rule of thumb: *DCR roughly doubles for every 10℃ increase*, i.e. $R(T) = R_0 \cdot 2^{(T-T_0)/10}$, where R is the dark-count rate at temperature T, and R_0 is the dark-count rate at temperature T_0. DCR is a source of current noise and scales with the number of SiPMs used.

In this study, past experience coupling CsI crystals and SiPMs motivated the choice of the following SiPM models: SensL J-series and Hamamatsu S14160. SensL and Hamamatsu data sheets, as summarised in table 5.1, both quote maximum operating temperatures of 85 ℃ which is fully appropriate to the intended application. Both manufacturers refer to reflow soldering conditions exceeding 200 ℃ so it seems unlikely that these devices will suffer significant physical damage at temperatures up to 100 ℃. A recent publication [93] performed a comparison of SensL J-series and and an older generation of Hamamatsu SiPMs (S12642-0404PA) coupled to various scintillators including *CsI:Tl* and found very similar performance in terms of energy resolution, despite a number of different properties, e.g. breakdown voltage, micro-cell size, and photo-detection efficiency. However, the SensL device was found to be less sensitive to temperature and bias changes, and exhibited superior linearity due to the larger number of micro-cells.

Table 5.1: Characteristics of the SensL J-series and Hamamatsu S14160 SiPMs.

Characteristics	Hamamatsu	SensL
Technology	HWB (Hole Wire Bonding)	TSV (Through Silicon Via)
SiPM Type	S14160-6050HS	J-series
Effective area	6.0 × 6.0 mm^2	6.07 × 6.07 mm^2
Number of microcells	14,331	22,292
Breakdown voltage	37.0 V	24.5 V
Recommended overvoltage	2.7 V	2.5 V
Temperature coefficient	34 mV/℃	21.5 mV/℃
Gain	2.5×10^6	2.8×10^6
Crosstalk probability	7 %	8 %
Operating temperature	-40 to 85 ℃	-40 to 85 ℃

5.3 Results

5.3.1 Light output of *CsI:Tl* and *CsI:Na* as a function of temperature

Due to the confusion in the available literature on their light output as a function of temperature, the relative light output from *CsI:Na* and *CsI:Tl* crystals was investigated in the temperature range 20-80 ℃. Both crystals were 1" × 1" cylinders supplied by Hilger Crystals, wrapped with reflective wrapping and packaged within aluminium cans with optical windows on one face. Though this canning was not strictly necessary for *CsI:Tl* due to its minimal hygroscopicity, getting identically packaged crystals allows for a direct comparison of the two materials.

Measurements were performed by coupling each of the crystals to a 2×2 array of Hamamatsu SiPMs (S13361-6050NE-02). The SiPMs were biased to a nominal voltage of 57 V at room temperature and varied with temperature so as to maintain a constant over-voltage and hence gain, based on the manufacturers specifications (54 mV/℃). The peak position of the 662 keV photopeak was measured at temperatures ranging from 20-80℃ and used as a measure of light output. It is expected that the linear relationship between breakdown voltage and temperature may not hold at the highest temperatures encountered in this experiment, however as both scintillators were treated the same way, any change in SiPM

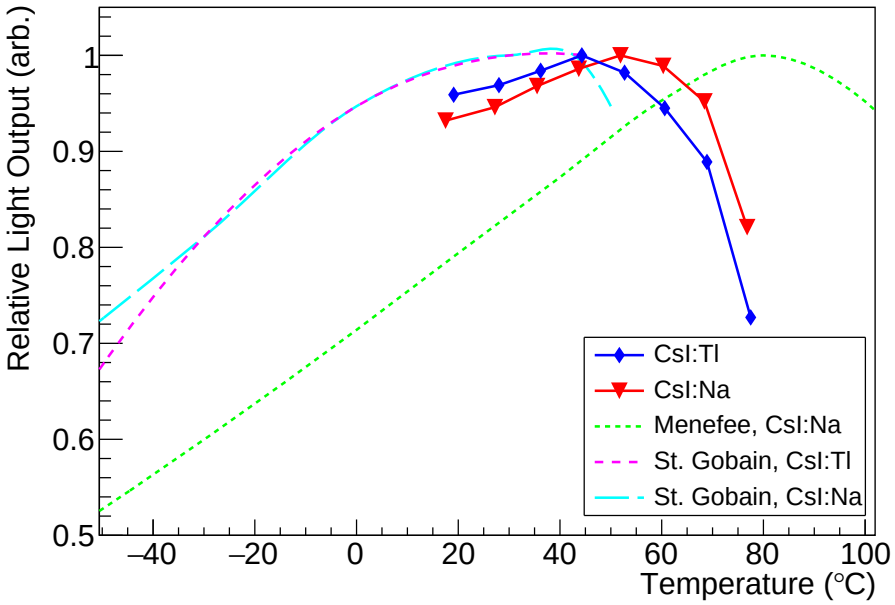

Figure 5.1: Relative light output as a function of temperature for *CsI:Tl* and *CsI:Na* crystals, as measured in this work, and compared to that reported in references [91] and [92]. The blue and the red are the experimental data.

gain will affect both measurements identically, hence will not influence the results reported here. A short shaping time was used so as to achieve the best possible performance at high temperature (see section 5.3.2).

The result of this investigation can be seen in figure 5.1, along with relative light outputs taken from [91] and [92]. In each case the light output has been normalised to the maximum to aid comparison. The results obtained here indicate that light output peaks at approximately 44 ℃ and 52 ℃ for *CsI:Tl* and *CsI:Na* respectively, as opposed to ∼80 ℃ as reported by Menefee et al. [91] or ∼30 ℃ as reported by Saint Gobain [92].

These measurements were performed by increasing the temperature of the chamber in stages and waiting until the temperature measured on the surface of the crystal became stable. It is possible that the wait time was not sufficient to allow the centre of the crystals to reach the measured temperature, in which case the temperatures reported in figure 5.1 would be artificially high. This effect could partially explain the discrepancy with the Saint Gobain data. The discrepancy with the Menefee et al. [91] result, indicating peak light

output at ∼80 ℃, could arise due to the fact that the PMT used was thermally isolated. Based on this result, (and bearing in mind that the absolute light output from *CsI:Na* is lower than that of *CsI:Tl*) we find no reason to favour *CsI:Na* over *CsI:Tl* for high temperature applications. Accordingly, unless otherwise stated, *CsI:Tl* is used throughout the remainder of this work.

5.3.2 Energy resolution vs shaping time at room temperature and high temperature

In order to evaluate the performance of prototype detectors coupiling *CsI:Tl* crystals to SiPMs, optimum operating parameters must be found, specifically bias and shaping time. The detector is ideally required to measure down to 60 keV so that it can be calibrated using a ^{241}Am source, hence there is a risk of the noise floor increasing beyond this signal level. As such, signal-to-noise ratio is an important figure-of-merit. Accurate measurement of the noise level is not straightforward hence the FWHM of the 662 keV photopeak is used as a proxy for this, despite energy resolution not being of critical importance for this application. FWHM at 662 keV is calculated following a quadratic energy calibration based on fits to peaks from 121 to 1408 keV from a ^{152}Eu source, in order to correct for any non-linearity.

Prototype detector assemblies were produced coupling a 7×7×25 mm^3 *CsI:Tl* crystal to either a 6×6 mm^2 SensL J-series SiPM or a 6×6 mm^2 Hamamatsu S14160-6050HS series SiPM. The scintillator crystals were wrapped with a minimum of eight layers of 0.2 mm PTFE tape and coupled to the photosensors using silicone-based optical grease (EJ-550). The nominal biases applied to the SensL J-series SiPM and Hamamatsu S14160-6050HS series SiPM were 29 V and 41 V, respectively. Detector readout was performed using an Ortec 571 shaping amplifier (with shaping times ranging from 0.5 to 10 μs) and a multi-channel analyser (Ortec EASY-MCA). Gamma-ray spectra were acquired using ^{137}Cs and ^{152}Eu sources to allow for energy calibration, linearity correction and measurement of energy resolution. Measurements were performed within a temperature controlled chamber,

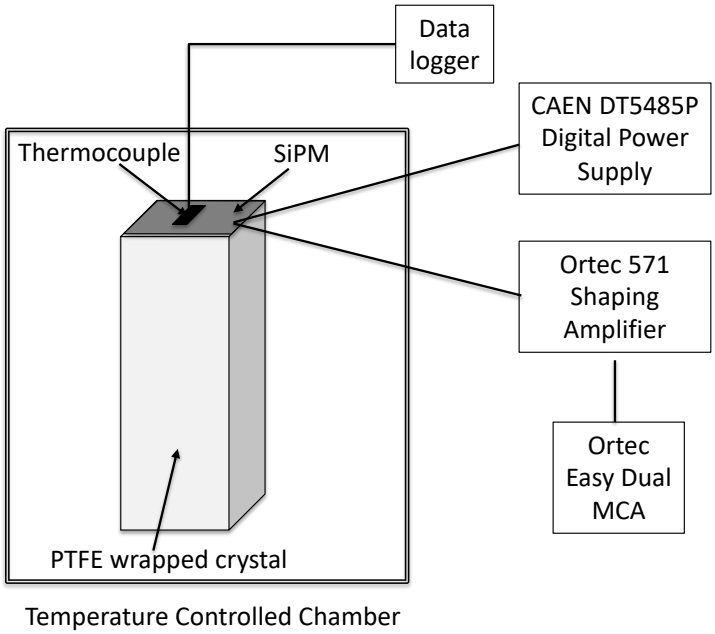

Figure 5.2: Schematic of the experimental setup used throughout this work.

with a thermocouple placed in close proximity to the SiPM board to allow monitoring of the temperature. A schematic of this set up is shown in Figure 5.2.

In figure 5.3, the linearity-corrected FWHM of the 662 keV photopeak is plotted as a function of shaping time. For all the measurements, the best resolution is observed at longer shaping times, which can be understood due to the long decay time of *CsI:Tl*. However, as can be seen from figure 5.4, when these measurements are repeated at high temperature (70℃) this situation changes dramatically. This can be explained when we consider that the noise is the sum of series and parallel noise. The low temperature curves are consistent with a standard noise model with negligible current noise (the curve forms a shallow minimum, not reached within this range of shaping times). When the temperature is increased the dark-count rate increases, which can be treated as a source of current noise, thus is more significant for longer shaping times [33]. We should also note here that

the decay time of *CsI:Tl* is known to reduce with increasing temperature [94], which may contribute to the shift to lower optimal shaping time at higher temperatures. Nevertheless, it is clear from figure 5.4 that shorter shaping times (2 μs or less) should be used at high temperature so as to minimise the contribution of this increased parallel noise. Accordingly, 2 μs shaping time is used as the optimum setting at high temperature with the standard electronics setup for the rest of this work.

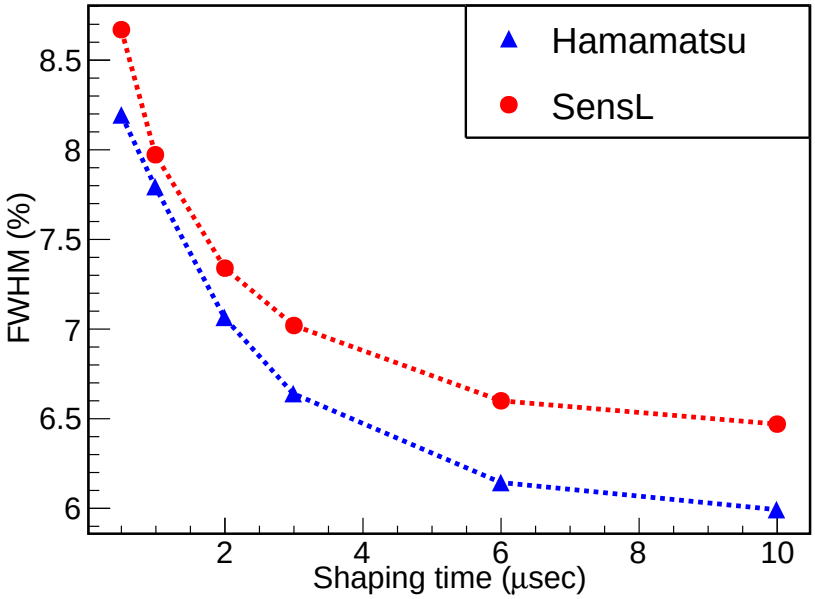

Figure 5.3: Linearity corrected energy resolution (at 662keV) as a function of shaping time for 6×6 mm^2 SensL J-series SiPM (red) and Hamamatsu S14160-6050HS (blue) each coupled to a 7×7×25 mm^3 *CsI:Tl* and operated at 29 V and 41 V respectively at room temperature.

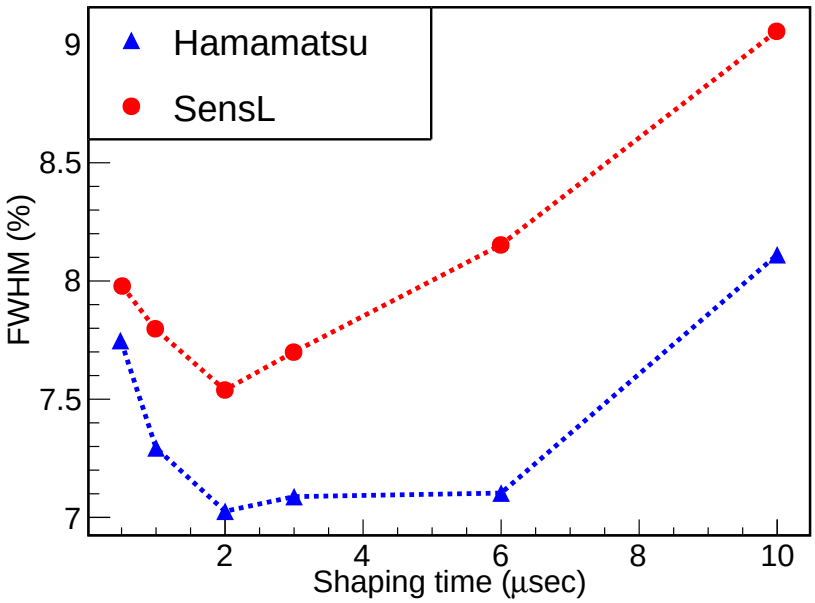

Figure 5.4: Energy resolution as a function of shaping time for SensL J-series (red) and Hamamatsu S14160-6050HS (blue) SiPM at a bias voltage of 29 V and 41 V respectively, with temperature measured at 70℃.

5.3.3 Energy resolution vs bias at room temperature and high temperature

Figures 5.5 and 5.6 show the bias optimisation of 6 × 6 mm^2 Hamamatsu S14160-6050HS and SensL J-series SiPMs respectively at room temperature and high temperature. The optimum operating voltages at room temperature are found to be 27.8 V and 41.0 V for SensL and Hamamatsu SiPMs: the corresponding ^{137}Cs and ^{152}Eu spectra can be seen in figures 5.7 and 5.8.

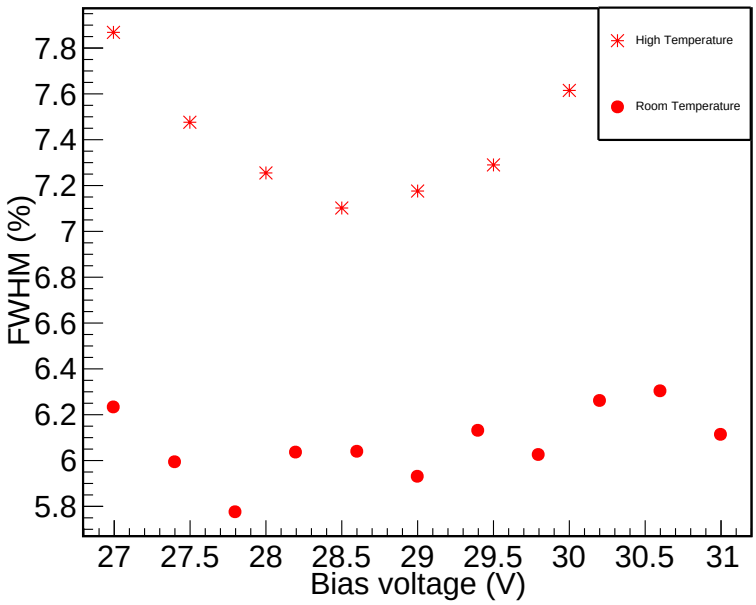

Figure 5.5: Linearity corrected energy resolution (at 662keV) as a function of bias voltage for 6×6 mm^2 SensL J-series SiPM coupled to a 7×7×25 mm^3 *CsI:Tl*, at room and high temperature (high temperature chamber set to 70 ℃)

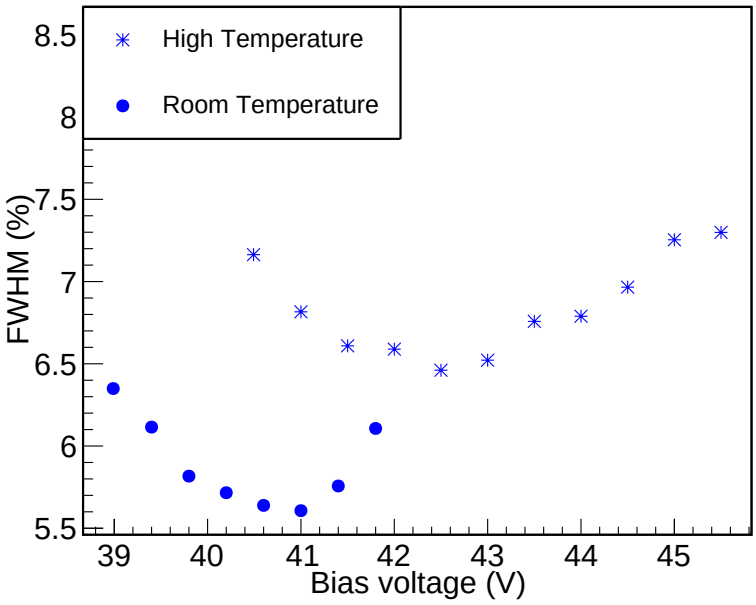

Figure 5.6: Linearity corrected energy resolution (at 662keV) as a function of bias voltage for 6 ×6 mm^2 Hamamatsu S14160-6050HS SiPM coupled to a 7×7×25 mm^3 *CsI:Tl*, at room and high temperature (high temperature chamber set to 70 ℃)

As was found for the shaping time, optimum operating conditions at high temperature differ significantly from those found at room temperature. This can be explained via similar arguments to those used in Section 5.3.2. As the dark count rate increases exponentially with temperature, a bias voltage chosen to maximise the signal-to-noise ratio at room temperature will not be optimal at higher temperatures.

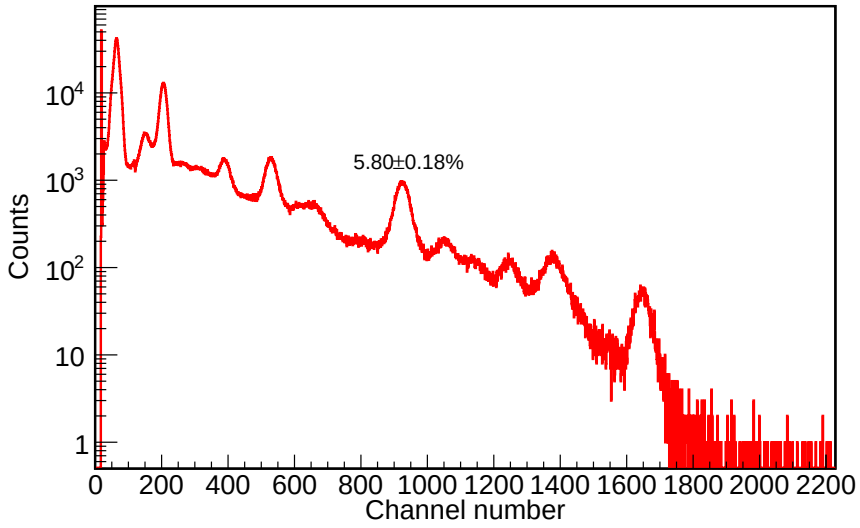

Figure 5.7: Energy spectrum for ^{137}Cs and ^{152}Eu radioactive sources, measured with a 6×6 mm^2 SensL SiPM coupled to a 7×7×25 mm^3 *CsI:Tl* at room temperature using 10 μs shaping time and a bias voltage of 27.8 V. The FWHM of the 662-keV peak was 5.80(18) %.

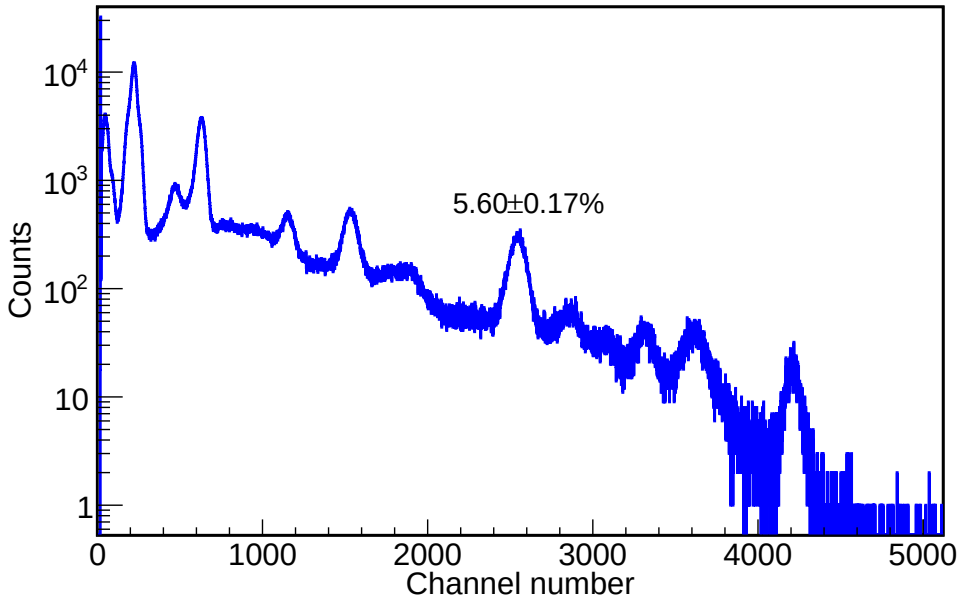

Figure 5.8: Energy spectrum for ^{137}Cs and ^{152}Eu radioactive sources measured with a 6×6 mm^2 Hamamatsu SiPM coupled to a 7×7×25 mm^3 *CsI:Tl* at room temperature using 10 μs shaping time and a bias voltage of 41 V. The FWHM of the 662-keV peak was 5.60(17) %.

A summary of the results obtained in terms of energy resolution and the optimised detector parameters such as bias voltage and shaping time is presented in table 5.2.

Table 5.2: Optimum characteristics of the SiPMs tested.

Characteristics	6×6 mm^2 Ham.	6×6 mm^2 SensL
Optimum shaping time (22℃)	10 μsec	10 μsec
Optimum shaping time (70℃)	2 μsec	2 μsec
Optimum bias voltage (22℃)	41.0 V	27.8 V
Optimum bias voltage (70℃)	42.5 V	28.5 V
Breakdown voltage	38.2 V	25.3 V
Energy Resolution (662 keV) at (22℃)	5.6%	5.8%
Energy Resolution (662 keV) at (70℃)	6.5%	7.1%

5.3.4 Temperature dependent gain stabilisation

In order to operate an SiPM over the large range of temperatures encountered during a well-logging measurement the bias must be adjusted to maintain a constant gain. Using the optimum settings found for our high temperature measurements, spectra were obtained at 80℃ with a ^{137}Cs source and the centroid of the 662 keV peak was noted. Spectra were then taken over a range of temperatures from 20-80℃, at each point adjusting the bias to match the peak position at 80℃. These spectra are shown in Figures 5.9 and 5.10. The increasing noise is evident on the left-hand-side of these spectra, with the 32 keV X-ray becoming obscured at the highest temperatures. In the case of the SensL SiPM at 80℃, this noise is sufficient to conflict with the requirement to detect gamma rays below 100 keV.

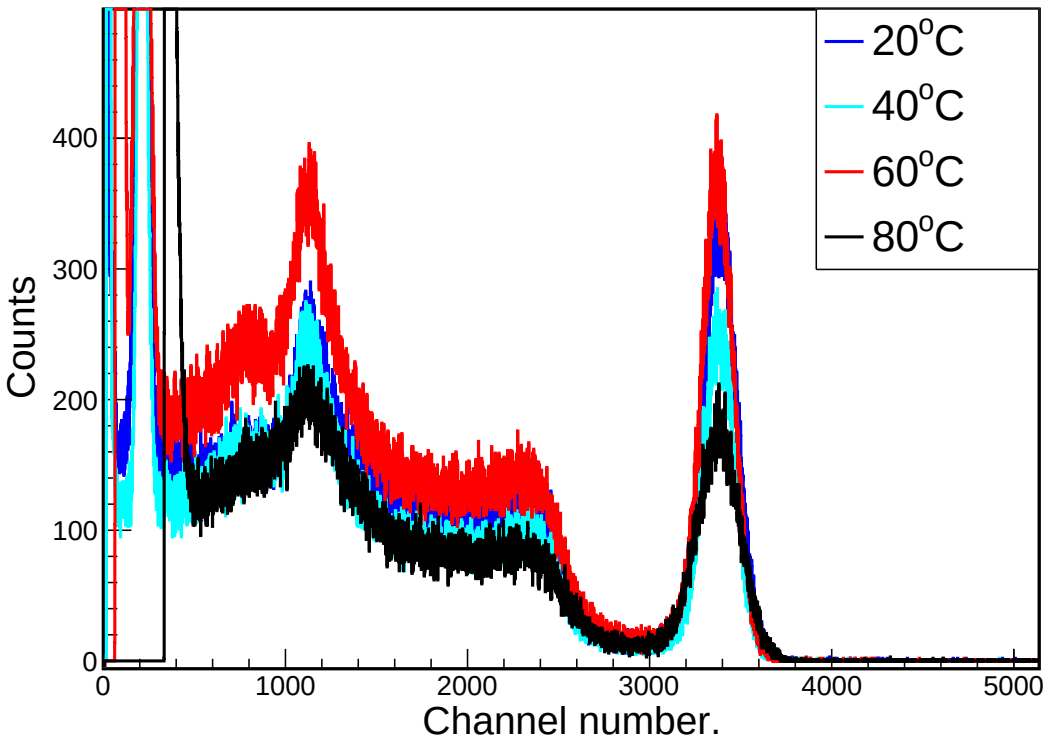

Figure 5.9: Spectra obtained with the SensL SiPM at 20℃ (blue), 40℃ (cyan), 60℃ (red) and 80℃ (black), manually adjusting the bias voltage to achieve the same 662-keV peak position (see text).

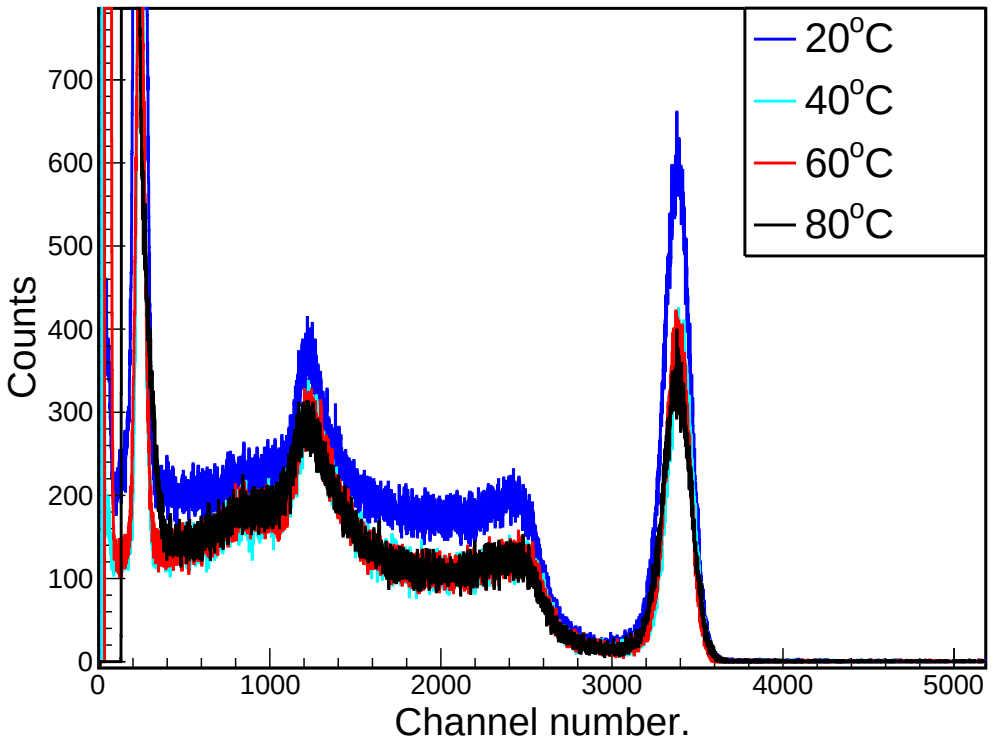

Figure 5.10: Spectra obtained with the Hamamatsu SiPM at 20℃ (blue), 40℃ (cyan), 60℃ (red) and 80℃ (black), manually adjusting the bias voltage to achieve the same 662-keV peak position (see text).

The bias voltages required to maintain the 662-keV peak position are plotted as a function of temperature in figures 5.11 and 5.12 for the Hamamatsu and SensL SiPM respectively. From linear fits to these data we find average temperature compensation coefficients of 38.6 mV/℃ and 27.4 mV/℃ for the Hamamatsu and SensL SiPMs respectively, somewhat different to the values of 34 mV/℃ and 21.5 mV/℃ quoted in the respective data sheets as can be seen in table 5.1 above. Furthermore, it is clear from the fits presented in figures 5.11 and 5.12 that a purely linear temperature compensation is not sufficient to stabilise the peak position over the large temperature range investigated here. Quadratic fits to these data were also performed and found to better reproduce the observed behaviour.

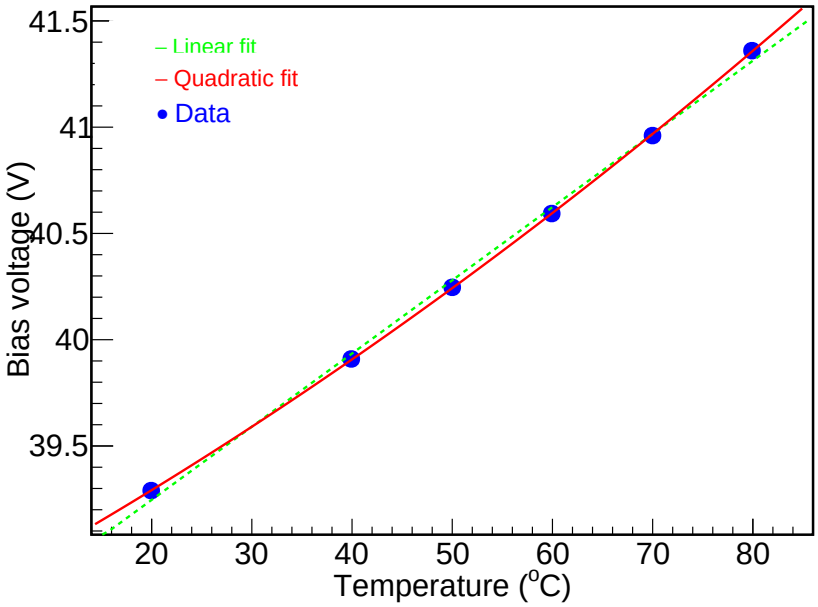

Figure 5.11: Bias required to maintain a constant 662-keV peak position, as a function of temperature for Hamamatsu SiPM, along with linear and quadratic fits to the data.

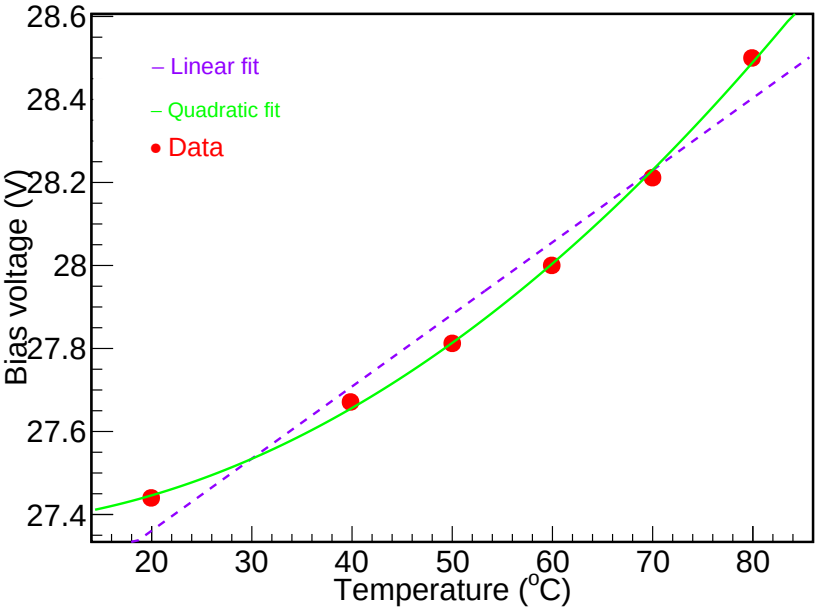

Figure 5.12: Bias required to maintain a constant 662-keV peak position, as a function of temperature for SensL SiPM, along with linear and quadratic fits to the data.

In figure 5.13, we present the energy resolution for the (linearity corrected) 662 keV peak, obtained from these spectra. Unsurprisingly, because the system has been optimised for the high temperature case, the resolution achieved at low temperatures is significantly worse than was achieved in sections 5.3.2 and 5.3.3. Furthermore, although there is some variation of FWHM across the temperature range and, notably, the strong disimprovement of performance of the SensL SiPM at the highest temperature considered, the variation is not large enough to conflict with the modest resolution requirements of this application.

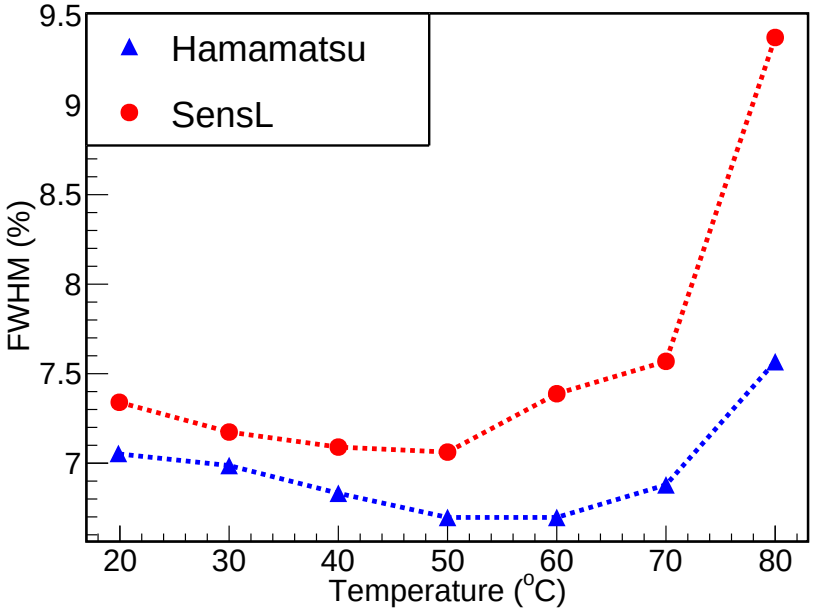

Figure 5.13: Corrected energy resolution (at 662keV) as a function of temperature for 7×7×25 mm^3 CsI:Tl coupled to a 6×6 mm^2 Hamamatsu S14160-6050HS (blue) and SensL J series SiPMs (red) respectively, with varying bias voltage.

5.4 Temperature compensation bias supply

A prototype temperature-compensated power supply has been designed and built capable of supplying a bias voltage up to 30 V. The device is controlled by an Arduino board, allowing it to be programmed to deliver the output voltage as any function of temperature. A circuit

diagram of the device is shown in figure 5.14. The board interfaces with a daughter board which holds the SiPM array and a digital temperature sensing chip (ADT7310).

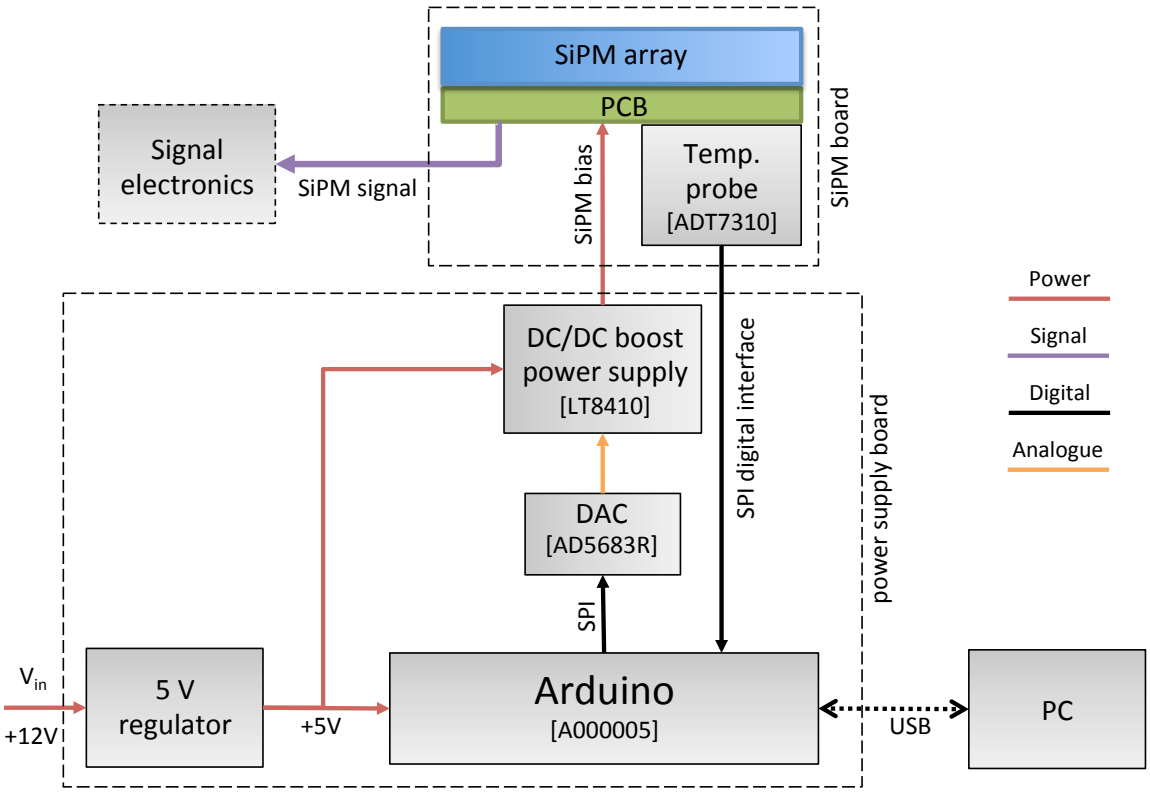

Figure 5.14: Schematic diagram of the temperature compensation power supply. The PC connection is only required whilst programming the supply.

The performance of the power-supply module can be seen in figure 5.15, for a 2×2 SensL J-series array, characterised from 20 to 80°C as described in section 5.3.4. Using a quadratic temperature compensation function, the module successfully stabilises the gain maintaining the peak position throughout the energy range up to 70°C. Beyond this temperature, the module was unable to deliver enough current to maintain the desired over-bias for this 2×2 array. A new version of the power-supply is being developed which will be able to deliver more current to allow gain stabilisation at higher temperature, as well as achieve higher bias voltages making it compatible with SiPMs from other manufacturers such as Hamamatsu.

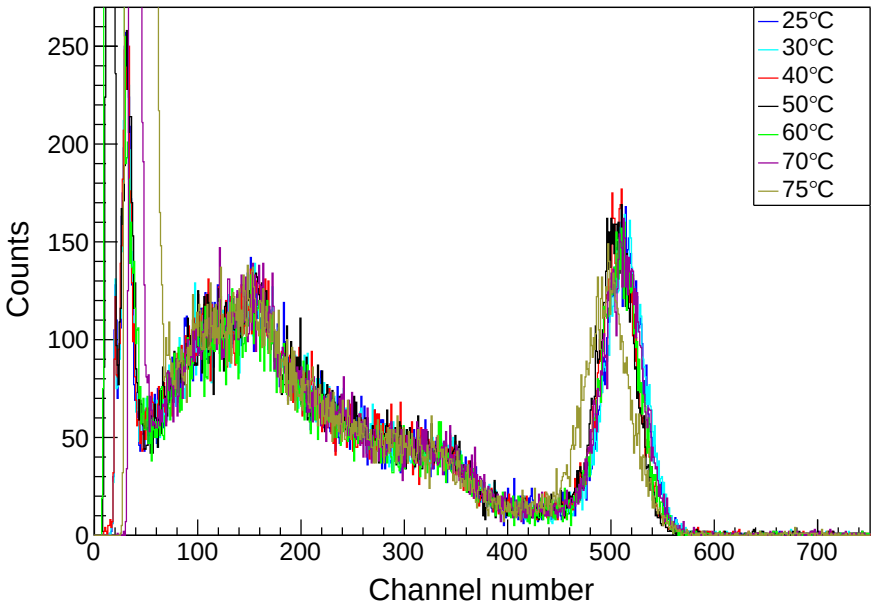

Figure 5.15: ^{137}Cs spectra obtained with a range of temperatures, with a variable bias supplied by a temperature compensation power-supply module.

5.5 Conclusion

Temperature sensitivity is a key parameter for photo sensors which might be coupled to scintillators and used in borehole logging. We have demonstrated the suitability of modern SiPM technology to replace the current standard PMT based instruments, providing benefits such as reductions in form factor and low voltage requirements. The characterisation carried out provides an indication of the performance that can be expected from an SiPM based detector system for a well-logging application and it is seen to be comparable to that from a standard *NaI:Tl* plus PMT solution. While we have demonstrated that both the SensL and Hamamatsu SiPMs are suitable in such an application, the superior energy resolution, smaller temperature dependence, and crucially, the lower noise at high temperatures, would make the Hamamatsu SiPM the preferred choice for this challenging environment. Furthermore, we have presented results on the performance of a prototype temperature compensating SiPM power supply suitable for use in such an application.

Chapter 6

General Conclusions

6.1 Discussion

High demands for neutron detection system in applications like the homeland security, nuclear waste repository, nuclear physics research, oil and gas exploration etc, coupled to the shortage of ^3He gas has led to the search of alternative detection technology to ^3He tube. The oil and gas industry, uses ^3He tube to investigate the presence of hydrocarbon. This method is complimented with a gamma ray measurement device that provide information about the density of the rock material under investigation. So, to understand the hydrogen content of the rock formation as well as the density of the material in the formation, two devices (neutron porosity and density logging tool) are required. Presently, both the ^3He tube for neutron porosity measurements and NaI:Tl crystal for density measurements are fitted with PMT as the photo-sensor. This photo-sensor, despite it great advantages, it also has its disadvantages which is centred to the fact that space is at a premium within the logging tool. This sensor occupy space and also requires very high voltage power supplier.

Due to the problems highlighted above, the research presented in this thesis has shown that other radiation detection technologies have the potential to address several fundamental problems and limitations in the oil and gas industry, with the aim to contribute and improve the conventional logging detection systems.

The results presented in Chapter 3 of this thesis is focused on simulating other alternative thermal neutron detection system in comparison to ^3He tube as used in neutron porosity tool to evaluate the hydrogen content of a logging formation. Geant4 was used as the simulation software to do these comparisons. Two lithium based detectors ($Eu : LiCAF$ and $GS20$) and one boron based detector (star straw detector) are simulated along side ^3He tube to compare their thermal neutron counting efficiencies. For a similar detector geometry, all the three (3) alternatives gave a better thermal neutron counting efficiency as compared to ^3He tube. The star straw detector can directly replace ^3He tube even with less high voltage requirement since both are only sensitive to thermal neutrons. However, the main motivation behind this research is the search of a dual neutron-gamma ray detection system. On this note, emphasis was given to the lithium-based detectors, in particular the lithium-loaded glass detector ($GS20$). Series of simulations ranging from effect of porosity to detector counting rate, effect of borehole size to effect of lithology were presented. In all these, the $GS20$ has demonstrated superior behaviour. In the same chapter, a simulation comparison on the gamma ray sensitive of $GS20$ to the conventional gamma-ray detector in the oil and gas industry (NaI:Tl crystal) was also presented. Nuclei that absorbs a thermal neutron de-excite by releasing what is known as characteristic captured gamma rays. Furthermore, when the fast neutrons emitted by the neutron source (AmBe) undergo inelastic scattering with the nuclei in the rock formation, another characteristic gamma ray known as inelastic gamma rays are released. Detection and and careful identification of each gamma ray line provides information about the elemental composition of the rock formation. From the results presented, the gamma ray sensitivity of $GS20$ is in comparison to that of the conventional gamma-ray detector.

Unlike the ^3He tube, $GS20$ crystal is not only sensitive to thermal neutrons, but also to epithermal neutrons with a resonance of 0.24 MeV above the reaction Q value. It was shown that, by measuring the contribution from epithermal neutrons, one can distinguish between hydrogen reach formations like water, coal and hydrocarbons and non hydrogen reach formations such as limestone, sandstone and dolomite. This feature gave $GS20$ a great advantage over ^3He tube.

When AmBe fast neutron source is used in a neutron porosity tool, the energetic gamma rays are not utilised in anyway. It has been demonstrated how the fast gamma rays from AmBe fast neutron source can provide useful information about the density of the material in the rock formation. Since for any gamma ray energy above 1.02 MeV, pair production happens to be the dominate interaction mechanism, we have shown how the use of a $GS20$ crystal can record the counts in the 0.511 MeV peak produced due to pair production. The result presented in figure 3.9 suggest that more counts are recorded in denser materials. When $GS20$ detectors are used with AmBe fast neutrons source, both neutron and gamma ray information can be recorded. This however, creates the difficulty of having to separate/discriminate between both particles to understand the contribution from each.

Chapter 4 focuses on the pulse shape discrimination analysis technique. Due to the lack large sized $GS20$ crystal in the laboratory, cesium lithium lanthanum bromide ($CLLB$) and cesium lithium lanthanum bromide chlorine ($CLLBC$) crystals were used instead to demonstrate how thermal neutrons, fast neutrons and gamma rays could be discriminated. Charge comparison method was used to achieve pulse shape discrimination analysis. This method relies on the principle that the scintillation light pulse produced in a scintillating material decays via different time constant depending on the type of interacting particle and the type of scintillating material. For elpasolites like $CLLB$ and $CLLBC$, the time it takes a pulse generated by gamma ray interaction to decay is longer than the time it takes a pulse generated by neutron interaction to decay. Discriminating between neutron and gamma rays using this method can be achieved by setting two time gates. The normalised pulse shapes were presented in figure 4.3 in chapter 4. The figure shows how both particles have similar rise time but entirely different decay time. The pulse shape discrimination ability of any detector is evaluated using figure of merit (FoM). A method that describes how well the energy peaks produced by multiple particles are separated. For the $CLLB$, a FoM of 1.4 was obtained for an energy cut around 3.2 MeVee and the low statistic high energy gamma rays.

The final result chapter (5 was devoted to addressing the detector specification re-

lated to high temperature and form factor as highlighted in the introductory chapter 1. Temperature sensitivity is a key parameter for photo-sensors which might be coupled to scintillators and used in borehole logging. We have demonstrated the suitability of modern SiPM technology to replace the current standard PMT based instruments, providing benefits such as reductions in form factor and low voltage requirements. The characterisation carried out provides an indication of the performance that can be expected from an SiPM based detector system for a well-logging application and it is seen to be comparable to that from a standard NaI:Tl plus PMT solution. While we have demonstrated that both the SensL and Hamamatsu SiPMs are suitable in such an application, the superior energy resolution, smaller temperature dependence, and crucially, the lower noise at high temperatures, would make the Hamamatsu SiPM the preferred choice for this challenging environment. Furthermore, we have presented results on the performance of a prototype temperature compensating SiPM power supply suitable for use in such an application.

6.2 Recommendations for Future Study

The sole aim of the research presented in this thesis is to provide a new ideas and ways of maximising the potential of a dual radiation detection technology in borehole logging applications.

In the future, it would be interesting to simultaneously record the information provided by both neutrons and gamma rays in the simulation presented in Chapter 3. It would also be interesting to reproduce all the results presented in Chapter 3 in real experimental settings. This couldn't be achieved in this research because the procurement of a large sized $GS20$ crystal as intended by the department couldn't be actualised. As the $GS20$ is sensitive to multiple radiations, it would be interesting to compare its discrimination ability to the elpasolites used as alternatives in this research. Because all evidence of the high temperature stability of $GS20$ provided herein is based on reported literature, as a future new generation dual radiation detector for logging application, it would be fascinating to test the temperature sensitivity of this crystal as well as its vibration tolerance.

Furthermore, it would be interesting to know how $CsI : Tl$ crystal coupled to SiPM performed as compared to $NaI : Tl$ coupled to PMT as used in density logging tool, although the idea of temperature compensation power supply is not a new concept. It would be fascinating to produce a bespoke, miniaturised temperature-compensated bias supply that would be appropriate to operate in the conditions experienced in borehole logging capable of temperature compensation beyond what was demonstrated in this thesis.

Finally, as machine learning is becoming very common in nuclear physics analysis, one interesting future research would be to adopt this method on the proposed dual radiation logging tool to discriminate between neutrons and gamma rays during real time logging activity.

Bibliography

[1] Hamilton M. Johnson. A history of well logging. *Geophysics*, 27(4):507–527, 08 1962.

[2] Cody R. Peeples, Medhat Mickael, and Robin P. Gardner. On replacing am–be neutron sources in compensated porosity logging tools. *Applied Radiation and Isotopes*, 68(4):926–931, 2010. The 7th International Topical Meeting on Industrial Radiation and Radio isotope Measurement Application(IRRMA-7).

[3] M. Oraby, K. Verghese, and R.P. Gardner. Investigation of an improved-sensitivity neutron-porosity oil-well logging tool. *Nuclear Instruments and Methods in Physics Research Section A: Accelerators, Spectrometers, Detectors and Associated Equipment*, 299(1):674–681, 1990.

[4] *A Comprehensive Neutron Porosity From a Pulsed Neutron Logging Tool*, volume Day 4 Tue, June 05, 2018 of *SPWLA Annual Logging Symposium*, 06 2018.

[5] Darwin V Ellis and Julian M Singer. *Well logging for earth scientists*, volume 692. Springer, 2007.

[6] Richard T. Kouzes et al. Progress in alternative neutron detection to address the ^{3}He shortage. *Nuclear Instruments and Methods in Physics Research Section A: Accelerators, Spectrometers, Detectors and Associated Equipment*, 784:172–175, 2015.

[7] Dana A Shea and Daniel L Morgan. The ^{3}He shortage: Supply, demand, and options for congress, 2010.

[8] Jihye Jeon et al. Optimization of gamma-ray detectors in neutron-induced gamma-ray spectroscopy for geophysical applications. *Nuclear Instruments and Methods in Physics Research Section A: Accelerators, Spectrometers, Detectors and Associated Equipment*, 954:162302, 2020.

[9] Richard T. Kouzes et al. Neutron detection alternatives to ^{3}He for national security applications. *Nuclear Instruments and Methods in Physics Research Section A: Accelerators, Spectrometers, Detectors and Associated Equipment*, 623(3):1035 – 1045, 2010.

[10] Richard T. Kouzes. The ^{3}He supply problem. *Pacific Northwest National Lab. (PNNL)*, 2009.

[11] Karl Zeitelhack. Search for alternative techniques to ^{3}He based detectors for neutron scattering applications. *Neutron News*, 23(4):10–13, 2012.

[12] Richard T Kouzes et al. BF_3 neutron detector tests. *Pacific Northwest National Laboratory*, 12 2009.

[13] Jeffrey L. Lacy et al. Boron-coated straws as a replacement for ^{3}He-based neutron detectors. *Nuclear Instruments and Methods in Physics Research Section A: Accelerators, Spectrometers, Detectors and Associated Equipment*, 652(1):359 – 363, 2011. Symposium on Radiation Measurements and Applications (SORMA) XII 2010.

[14] Zhaoyang Xie et al. Experimental study of boron-coated straws with a neutron source. *Nuclear Instruments and Methods in Physics Research Section A: Accelerators, Spectrometers, Detectors and Associated Equipment*, 888:235 – 239, 2018.

[15] A. Maity et al. High efficiency hexagonal boron nitride neutron detectors with 1 cm^2 detection areas. *Applied Physics Letters*, 116(14):142102, 2020.

[16] F. D. others Amaro. Novel concept for neutron detection: proportional counter filled with ^{10}B nanoparticle aerosol. *Scientific Reports*, 7(1), 2017.

[17] B. G. Hubner et al. A novel neutron detector for porosity logging. In *1990 IEEE Nuclear Science Symposium Conference Record*, pages 817–819, 1990.

[18] F.W.K. Firk et al. An improved ^{6}Li-loaded glass scintillator for neutron detection. *Nuclear Instruments and Methods*, 13:313–316, 1961.

[19] A.R. Spowart. Neutron scintillating glasses: Part 1: Activation by external charged particles and thermal neutrons. *Nuclear Instruments and Methods*, 135(3):441–453, 1976.

[20] A.R. Spowart. Neutron scintillating glasses: Part ii: The effects of temperature on pulse height and conductivity. *Nuclear Instruments and Methods*, 140(1):19–28, 1977.

[21] E.J. Fairley and A.R. Spowart. Neutron scintillating glasses part iii pulse decay time measurements at room temperature. *Nuclear Instruments and Methods*, 150(2):159–163, 1978.

[22] ^{6}Li Glass. `https://scintacor.com/products/6-lithium-glass/`. Accessed: 2020-07-30.

[23] Sergey V. Polyakov. Chapter 3 - photomultiplier tubes. In *Single-Photon Generation and Detection*, volume 45 of *Experimental Methods in the Physical Sciences*, pages 69–82. Academic Press, 2013.

[24] Maria Giuseppina Bisogni et al. Medical applications of silicon photomultipliers. *Nuclear Instruments and Methods in Physics Research Section A: Accelerators, Spectrometers, Detectors and Associated Equipment*, 926:118 – 128, 2019.

[25] G. Llosá. SiPM-based compton cameras. *Nuclear Instruments and Methods in Physics Research*, 926:148 – 152, 2019.

[26] Haewook Park and Jae Sung Lee. Highly multiplexed SiPM signal readout for brain-dedicated TOF-DOI PET detectors. *Physica Medica*, 68:117 – 123, 2019.

[27] J.A. Jeon et al. Fabrication and testing of a 1024-pixel SiPM camera. *Nuclear Instruments and Methods in Physics Research*, 958:162839, 2020.

[28] Kenji Shimazoe et al. Development of simultaneous PET and Compton imaging using GAGG-SiPM based pixel detectors. *Nuclear Instruments and Methods in Physics Research Section A: Accelerators, Spectrometers, Detectors and Associated Equipment*, 954:161499, 2020.

[29] Ilya Obodovskiy. Chapter 7 - interaction of neutrons with matter. In Ilya Obodovskiy, editor, *Radiation*, pages 151 – 160. Elsevier, 2019.

[30] M.M.R. Williams. Nuclear energy: An introduction to the concepts, systems, and applications of nuclear processes, fifth edition: Raymond l. murray, butterworth heinemann, pp 490, isbn 0 7506 7136 x. *Annals of Nuclear Energy*, 28(9):935 – 936, 2001.

[31] A. Pietropaolo et al. Neutron detection techniques from μeV to GeV. *Physics Reports*, 875:1–65, 2020.

[32] Saha G.B. *Gas-Filled Detectors*. Springer, New York, 2013.

[33] Glenn F Knoll. *Radiation Detection and Measurement*. Wiley, New York, NY, jan 2010.

[34] David Jenkins. *Radiation Detection for Nuclear Physics*. 2053-2563. IOP Publishing, 2020.

[35] J B Birks. Scintillations from organic crystals: Specific fluorescence and relative response to different radiations. *Proceedings of the Physical Society. Section A*, 64(10):874–877, oct 1951.

[36] Emil Rofors. *A Fast Pixelated Thermal-Neutron Detector*. PhD thesis, Lund University, 11 2020.

[37] Photomultiplier tube. `https://en.wikipedia.org/wiki/Photomultiplier_tube`. Accessed: 2021-02-18.

[38] Tyana Stiegler et al. Replacement of a photomultiplier tube with silicon photomultipliers for use in safeguards applications, 2020.

[39] B Dolgoshein et al. Status report on silicon photomultiplier development and its applications. *Nuclear Instruments and Methods in Physics Research Section A: Accelerators, Spectrometers, Detectors and Associated Equipment*, 563(2):368–376, 2006.

[40] G. Bondarenko et al. Limited geiger-mode silicon photodiode with very high gain. *Nuclear Physics B - Proceedings Supplements*, 61(3):347–352, 1998. Proceedings of the Fifth International Conference on Advanced Technology and Particle Physics.

[41] P. Buzhan et al. Silicon photomultiplier and its possible applications. *Nuclear Instruments and Methods in Physics Research Section A: Accelerators, Spectrometers, Detectors and Associated Equipment*, 504(1):48–52, 2003. Proceedings of the 3rd International Conference on New Developments in Photodetection.

[42] An Introduction to the Silicon Photomultiplier. `https://www.sensl.com/downloads/ds/TN%20-%20Intro%20to%20SPM%20Tech.pdf`. Accessed: 2021-03-17.

[43] Hamamatsu SiPM. `https://www.hamamatsu.com/eu/en/product/type/S14160-6050HS/index.html`. Accessed: 2021-03-17.

[44] Hamamatsu SiPM. `https://www.hamamatsu.com/eu/en/product/type/S13360-6050PE/index.html`. Accessed: 2021-03-17.

[45] Keiichi Shibata and others. Jendl-4.0: A new library for nuclear science and engineering. *Journal of Nuclear Science and Technology*, 48(1):1–30, 2011.

[46] Walid A. Metwally. Existing NaI detectors; an efficient alternative to he-3 detectors. *Nuclear Instruments and Methods in Physics Research Section B: Beam Interactions with Materials and Atoms*, 338:48 – 51, 2014.

[47] Walid A. Metwally and Amira G. Emam. Experimental validation and testing of a NaI boron-lined neutron detector. *Nuclear Instruments and Methods in Physics Research Section B: Beam Interactions with Materials and Atoms*, 422:7 – 11, 2018.

[48] K.D. Ianakiev et al. ^{6}Li foil scintillation sandwich thermal neutron detector. *Nuclear Instruments and Methods in Physics Research Section A: Accelerators, Spectrometers, Detectors and Associated Equipment*, 652(1):417 – 420, 2011. Symposium on Radiation Measurements and Applications (SORMA) XII 2010.

[49] A. Pappalardo et al. Characterization of the silicon+^{6}LiF thermal neutron detection technique. *Nuclear Instruments and Methods in Physics Research Section A: Accelerators, Spectrometers, Detectors and Associated Equipment*, 810:6 – 13, 2016.

[50] Paolo Finocchiaro et al. Absolute efficiency calibration of ^{6}LiF-based solid state thermal neutron detectors. *Nuclear Instruments and Methods in Physics Research Section A: Accelerators, Spectrometers, Detectors and Associated Equipment*, 885:86 – 90, 2018.

[51] A.R. Spowart. Neutron scintillating glasses: Part ii: The effects of temperature on pulse height and conductivity. *Nuclear Instruments and Methods*, 140(1):19 – 28, 1977.

[52] D. M. Schneider and B. G. Hubner. Neutron/gamma discrimination in a lithium-6 glass scintillator in an mwd tool. In *Conference Record of the 1991 IEEE Nuclear Science Symposium and Medical Imaging Conference*, pages 1113–1117 vol.2, 1991.

[53] A. Nikitin et al. Novel glass ceramic scintillator for detection of slow neutrons in well logging applications. *IEEE Transactions on Nuclear Science*, 60(2):1044–1048, 2013.

[54] Noriaki Kawaguchi et al. Temperature dependence of scintillation responses in rare-earth-ions-doped $LiCaAlF_6$ single crystals. *Nuclear Instruments and Methods in Physics Research Section A: Accelerators, Spectrometers, Detectors and Associated Equipment*, 954:161518, 2020. Symposium on Radiation Measurements and Applications XVII.

[55] Jinlu Ruan et al. Luminescent properties of lithium glass scintillator at low temperatures. *Nuclear Instruments and Methods in Physics Research Section A: Accelerators, Spectrometers, Detectors and Associated Equipment*, 953:163190, 2020.

[56] G.C. Rich et al. Fabrication and characterization of a lithium-glass-based composite neutron detector. *Nuclear Instruments and Methods in Physics Research Section A: Accelerators, Spectrometers, Detectors and Associated Equipment*, 794:15 – 24, 2015.

[57] M. Mayer et al. Development and characterization of a neutron detector based on a lithium glass–polymer composite. *Nuclear Instruments and Methods in Physics Research Section A: Accelerators, Spectrometers, Detectors and Associated Equipment*, 785:117 – 122, 2015.

[58] M.M. Bourne et al. Characterization of the CLYC detector for neutron and photon detection. *Nuclear Instruments and Methods in Physics Research Section A: Accelerators, Spectrometers, Detectors and Associated Equipment*, 736:124 – 127, 2014.

[59] A Mentana et al. Measurement of fast neutron detection efficiency with ^{6}Li and ^{7}Li enriched CLYC scintillators. *Journal of Physics: Conference Series*, 763:012006, 2016.

[60] Urmila Shirwadkar. Scintillation properties of $Cs_2LiLaBr_6$ CLLB crystals with varying Ce^{3+} concentration. *Nuclear Instruments and Methods in Physics Research Section A: Accelerators, Spectrometers, Detectors and Associated Equipment*, 652(1):268 – 270, 2011. Symposium on Radiation Measurements and Applications (SORMA) XII 2010.

[61] Quanying Zhang et al. A method for determining density based on gamma ray and fast neutron detection using a Cs_2LiYCl_6 detector in neutron-gamma density logging. *Applied Radiation and Isotopes*, 142:77 – 84, 2018.

[62] Richard S. et al. Characterization of the internal background for thermal and fast neutron detection with CLLB. *Nuclear Instruments and Methods in Physics Research*, 838:147 – 153, 2016.

[63] K.E. Mesick et al. Pulse-shape discrimination and energy quenching of alpha particles in cs2lilabr6:ce3+. *Nuclear Instruments and Methods in Physics Research Section A: Accelerators, Spectrometers, Detectors and Associated Equipment*, 841:139 – 143, 2017.

[64] T. Fujiwara et al. Study on ce:licaf scintillator for 3he alternative detector. *Neutron News*, 23(4):31–34, 2012.

[65] Michael A. Ford et al. Evaluation of eu:licaf for neutron detection utilizing sipms and portable electronics. *Nuclear Instruments and Methods in Physics Research Section A: Accelerators, Spectrometers, Detectors and Associated Equipment*, 908:110 – 116, 2018.

[66] S. Agostinelli et al. Geant4—a simulation toolkit. *Nuclear Instruments and Methods in Physics Research Section A: Accelerators, Spectrometers, Detectors and Associated Equipment*, 506(3):250 – 303, 2003.

[67] J F Briesmeister. Mcnp: a general Monte Carlo code for neutron and photon transport. version 3a. revision 2. ., 1986.

[68] A. Ferrari et al. Fluka: a multi-particle transport code, 2005.

[69] E. Mendoza et al. New standard evaluated neutron cross section libraries for the geant4 code and first verification. *IEEE Transactions on Nuclear Science*, 61(4):2357–2364, 2014. cited By 35.

[70] R. Chytracek et al. Geometry description markup language for physics simulation and analysis applications. *IEEE Transactions on Nuclear Science*, 53(5):2892–2896, 2006.

[71] C Vuosalo et al. A tool to convert CAD models for importation into Geant4. *Journal of Physics: Conference Series*, 898:042024, oct 2017.

[72] Andrii Tykhonov. A light-weight tool for converting cad drawings into the gdml format. *https://github.com/tihonav/cad-to-geant4-converter*, 2019.

[73] M. Klausz et al. Performance evaluation of the boron coated straws detector with Geant4. *Nuclear Instruments and Methods in Physics Research Section A: Accelerators, Spectrometers, Detectors and Associated Equipment*, 943:162463, 2019.

[74] J. L. Lacy et al. The evolution of neutron straw detector applications in homeland security. *IEEE Transactions on Nuclear Science*, 60(2):1140–1146, 2013.

[75] H Basiri and H Tavakoli-Anbaran. Investigation of some possible changes in Am-Be neutron source configuration in order to increase the thermal neutron flux using monte carlo code. *Journal of Physics: Conference Series*, 956:012010, jan 2018.

[76] J.W. Marsh, D.J. Thomas, and M. Burke. High resolution measurements of neutron energy spectra from ambe and amb neutron sources. *Nuclear Instruments and Methods in Physics Research Section A: Accelerators, Spectrometers, Detectors and Associated Equipment*, 366(2):340–348, 1995.

[77] Zhenzhou Liu et al. The 4.438 MeV gamma to neutron ratio for the Am–Be neutron source. *Applied Radiation and Isotopes*, 65(12):1318–1321, 2007.

[78] R. B. Owen. The decay times of organic scintillators and their application to the discrimination between particles of differing specific ionization. *IRE Transactions on Nuclear Science*, 5(3):198–201, 1958.

[79] F. D. Brooks et al. Pulse shape discrimination in a plastic scintillator. *IRE Transactions on Nuclear Science*, 7(2-3):35–38, 1960.

[80] F.D. Brooks. A scintillation counter with neutron and gamma-ray discriminators. *Nuclear Instruments and Methods*, 4(3):151–163, 1959.

[81] F. D. Brooks et al. Pulse shape discrimination in a plastic scintillator. *IRE Transactions on Nuclear Science*, 7(2-3):35–38, 1960.

[82] C. Coceva. Pulse-shape discrimination with a glass scintillator. *Nuclear Instruments and Methods*, 21:93–96, 1963.

[83] D.L. Smith et al. Measurement of the response of several organic scintillators to electrons, protons and deuterons. *Nuclear Instruments and Methods*, 64(2):157–166, 1968.

[84] A. Martin-Martin et al. Evaluation of CdZnTe as neutron detector around medical accelerators. *Radiation Protection Dosimetry*, 133(4):193–199, 03 2009.

[85] J. Glodo et al. Selected properties of Cs_2LiYCl_6, $Cs_2LiLaCl_6$, and $Cs_2LiLaBr_6$ scintillators. *IEEE Transactions on Nuclear Science*, 58(1):333–338, 2011.

[86] J. Glodo et al. Cs_2LiYCl_6:Ce neutron gamma detection system. In *2007 IEEE Nuclear Science Symposium Conference Record*, volume 2, pages 959–962, 2007.

[87] J. Glodo et al. Pulse shape discrimination with selected elpasolite crystals. *IEEE Transactions on Nuclear Science*, 59(5):2328–2333, 2012.

[88] H. Al Hamrashdi et al. Neutron/gamma pulse discrimination analysis of GS10 lithium glass and EJ-204 plastic scintillators. *Journal of Instrumentation*, 15(01):P01031–P01031, jan 2020.

[89] M.D. Aspinall et al. Verification of the digital discrimination of neutrons and gamma-rays using pulse gradient analysis by digital measurement of time of flight. *Nuclear Instruments and Methods in Physics Research Section A: Accelerators, Spectrometers, Detectors and Associated Equipment*, 583(2):432–438, 2007.

[90] Nakayama, M and others. Scintillation activated by nanoparticle formation in CsI:Na thin films. *Journal of Luminescence*, 108(1-4):359–363, jun 2004.

[91] Menefee, J and others. Sodium Activated Cesium Iodide as a Gamma Ray and Charged Particle Detector. *IEEE Transactions on Nuclear Science*, 14(1):464–467, jan 1967.

[92] Gobain, Saint. CsI(Tl), CsI(Na) Cesium Iodide Scintillation Material, Aug. 2016.

[93] Grodzicka-Kobylka, M and others. Comparison of SensL and Hamamatsu 4×4 channel SiPM arrays in gamma spectrometry with scintillators. *Nuclear Inst. and Methods in Physics Research, A*, 856:53–64, 2017.

[94] John D. Valentine et al. Temperature dependence of CsI(Tl) gamma-ray excited scintillation characteristics. *Nuclear Inst. and Methods in Physics Research, A*, 325(1-2):147–157, feb 1993.

Appendix A:

Journal Article [redacted]

Nuclear Inst. and Methods in Physics Research, A 997 (2021) 165161

Contents lists available at ScienceDirect

Nuclear Inst. and Methods in Physics Research, A

journal homepage: www.elsevier.com/locate/nima

Operation of scintillators and SiPMs at high temperatures and their application for borehole logging

A. Bala [a,b,*], J.R. Brown [a,**], D.G. Jenkins [a], P. Joshi [a]

[a] Department of Physics, University of York, YO10 5DD, York, UK
[b] Department of Physics, Usmanu Danfodiyo University, P.M.B. 2346, Sokoto, Nigeria

ARTICLE INFO

Keywords:
Borehole logging
Inorganic scintillators
Silicon photomultipliers
Gamma-ray spectrometry

ABSTRACT

Gamma-ray detection is extensively used in borehole logging — a technique widely employed in oil and gas, and mineral exploration. The workhorse of this detection application for many years has been traditional NaI(Tl) scintillators coupled to photo-multiplier tubes (PMTs) which can provide the performance and energy resolution required in this application. PMTs are a well proven technology which can operate in the high temperature conditions (typically of order 100 °C) and pressures (10 MPa) encountered during logging activities. PMTs are, however, fragile in that they incorporate an evacuated tube. They also have a large form factor and require ancillary electronics such as a high-voltage supply meaning they occupy significant space within the borehole probe. It would be advantageous to have a compact replacement to allow additional instruments to be included within the borehole probe. Silicon photo-multipliers (SiPMs) are an attractive PMT replacement since they are robust, compact and operate at low voltage. However, SiPMs suffer from dark current which increases rapidly with temperature leading to increased noise and degraded energy resolution. We have evaluated CsI(Tl) scintillators coupled to standard 6 × 6 mm^2 SiPMs from Hamamatsu and SensL as a function of temperature. We have shown that these prototypes operate effectively up to a temperature of 80 °C which could satisfy the requirements of some applications of borehole logging where the maximum temperature encountered is 75 °C.

1. Introduction

Borehole logging is a technique used for studying geological formations as an aid to mineral (or oil and gas) exploration. Boreholes can be several hundred metres to a few kilometres deep, yet only ~10 cm wide. At these depths, temperatures in excess of 100 °C and pressures of 10 MPa are typical, hence the instrumentation used in borehole logging must be able to operate satisfactorily in this environment, meet the strict form-factor requirements, as well as be sufficiently rugged for use in a heavy industrial setting.

Gamma-ray detection is a common and useful aspect of borehole logging and is principally used in two applications:

1. γ-ray detection from naturally occurring sources in minerals. This application can be achieved with modest energy resolution since it relies on identifying the high-energy gamma peak from the decay of ^{40}K and a few gamma ray peaks from the progenies of Uranium and Thorium which are well separated.
2. Detection of Compton-scattered photons from a ^{137}Cs source to determine the density of materials surrounding the borehole probe. Here, energy resolution is not especially important but it is advantageous to be able to detect lower energy (<100 keV) gamma rays to maximise efficiency and so that a ^{241}Am source (60 keV γ ray) can be employed for calibration.

The standard instrument used in both applications is a NaI(Tl) scintillator coupled to a photomultiplier tube (PMT). However, such devices, and their associated powersupplies, are rather bulky; a significant limitation given the very limited space available within a borehole probe. An alternative photosensor which is more compact would be of great interest in this application. An attractive replacement technology consists of silicon photomultipliers (SiPMs). These devices have been revolutionary in medical imaging applications [1–5] and are finding wider application in experimental nuclear physics as well as related societal applications. SiPMs are robust and have a small form factor and unlike PMTs, they do not need a high voltage. In recent years, a number of manufacturers have made advances in this technology resulting in higher gain, lower dark-count-rate (DCR), reduced cross-talk and after-pulsing, as well as reduced temperature sensitivity. These devices now present the possibility of creating a new generation of compact, low-voltage detectors for the borehole logging application.

* Corresponding author at: Department of Physics, University of York, YO10 5DD, York, UK.
** Corresponding author.
E-mail addresses: aliyu.bala@york.ac.uk (A. Bala), jamie.brown@york.ac.uk (J.R. Brown).

https://doi.org/10.1016/j.nima.2021.165161
Received 16 November 2020; Received in revised form 4 February 2021; Accepted 15 February 2021
Available online 19 February 2021

In this work, we report on efforts to develop a SiPM-based detector suitable for replacing PMT-based gamma-ray detectors which was motivated by the needs of Robertson Geologging (RG), an international company active in the field of borehole logging who are based in North Wales. From their perspective, and with their years of experience in this field, they were strongly motivated to reduce the form factor of the radiation detectors especially gamma-ray detectors used in their borehole logging probes to permit more instruments to be accommodated in the probe at the same time. This would provide an important differentiator for them from competitor's offerings. Furthermore, for the market which they access which focuses on mineral exploration, an upper temperature rating of 75 °C is compatible with the majority of applications which they support.

2. Choice of detector materials

Critical to this study is the choice of appropriate materials to form the prototype detector. Accordingly, we initially discuss the motivation for the selection of the scintillator crystals and SiPMs to be studied.

2.1. Choice of scintillator for high temperature operation

An ideal crystal should have good proportionality, strong scintillation emission and a suitable wavelength matching to typical SiPMs. $CeBr_3$ and $LaBr_3$:Ce are two options which have excellent proportionality and high light emission. Their cost as compared to the NaI:Tl makes them unsuitable for such an industrial application, particularly when energy resolution is not of utmost importance. A more practical choice are CsI:Tl and CsI:Na scintillators having peak emission wavelengths of 550 and 420 nm, respectively. They give very similar performance to NaI(Tl) and are only marginally more expensive, though with significantly longer decay times (1000 ns and 630 ns respectively, compared to 230 ns for NaI:Tl). However, they are a much better match to the performance of the SiPMs used in this work. Moreover, since they are only slightly hygroscopic, it is possible to dispense with canning, optical windows etc. and further save space.

As the detectors are to be operated at elevated temperature, the change in their light output as a function of temperature becomes a relevant consideration. If such crystals become brighter at the temperatures considered in this application then the improved photon statistics may at least partially offset the degradation of the SiPM performance at elevated temperature — an issue to be discussed in more detail below. Some authors have reported an increasing light output for CsI:Na [6,7] peaking at ∼80 °C. This would be of particular interest for the borehole logging application as 80°C is within the typical operating temperature range, however it should be noted that the data cited are at odds with contemporary data sheets from Saint Gobain Crystals which indicate that both CsI:Tl and CsI:Na exhibit maximum light output at ∼30 °C [8]. These considerations motivated the choice of CsI:Tl and CsI:Na as the crystals to be investigated in this study.

2.2. Choice of silicon photomultiplier

Silicon photomultipliers has spawned a number of new manufacturers, namely KeteK, AdvanSiD, First Sensor and Excelitas, in addition to the more established Hamamatsu and SensL. Compared to photodiodes and avalanche photodiodes (APDs), SiPM exhibit less temperature sensitivity, they are far from immune to temperature effects. The breakdown voltage of SiPM increases with temperature. Constant bias voltage manifests in peak height reduction due to the reduction in over-voltage (i.e. $V_{over} = V_{bias} - V_{breakdown}$) which leads to a reduction in gain with temperature. Small temperature changes results in photopeak broadening, leading to poor energy resolution. Peak shift will be observed for large temperature changes, adjusting the bias voltage will mitigate this effect. Additionally, dark-count rate (DCR) increases with temperature as characterised by the rule of thumb: *dark-count rate roughly doubles for every 10 °C increase*, i.e. $R(T) = R_0 \cdot 2^{(T-T_0)/10}$, where R is the dark-count rate at temperature T, and R_0 is the dark-count rate at temperature T_0.

In this study we focus on SiPMs from SensL and Hamamatsu, specifically SensL J-series and Hamamatsu S14160 (see Table 1), principally due to their maximum operating temperatures of 85 °C which is significantly higher than other manufacturers at the time of evaluation. Both manufacturers refer to reflow soldering conditions exceeding 200 °C, however this is very short time process compared to logging time, so it worth investigating the maximum temperature both SiPMs can be subjected to without permanent degradation of performance. A recent publication [9] performed a comparison of SensL J-series and an older generation of Hamamatsu SiPMs (S12642-0404PA) coupled to various scintillators including CsI:Tl and found very similar performance in terms of energy resolution, despite a number of different properties, e.g. breakdown voltage, micro-cell size, and photo-detection efficiency. However, the SensL device was found to be less sensitive to temperature and bias changes, and exhibited superior linearity due to the larger number of micro-cells.

3. Results

3.1. Light output of CsI:Tl and CsI:Na as a function of temperature

Due to the confusion in the available literature on their light output as a function of temperature, the relative light output from CsI:Na and CsI:Tl crystals was investigated in the range 20–80 °C. Both crystals were 1" × 1" cylinders supplied by Hilger Crystals, wrapped with reflective wrapping and packaged within aluminium cans with optical windows on one face. Though this canning was not strictly necessary for CsI:Tl due to its minimal hygroscopicity, getting identically packaged crystals allows for a direct comparison of the two materials.

Measurements were performed by coupling each of the crystals to a 2 × 2 array of Hamamatsu SiPMs (S13361-6050NE-02). The SiPMs were biased to a nominal voltage of 57 V at room temperature and varied with temperature so as to maintain a constant over-voltage and hence gain, based on the manufacturers specifications (54 mV/°C). The peak position of the 662 keV photopeak was measured at temperatures ranging from 20–80 °C and used as a measure of light output. It is expected that the linear relationship between breakdown voltage and temperature may not hold at the highest temperatures encountered in this experiment, however as both scintillators were treated the same way, any change in SiPM gain will affect both measurements identically, hence will not influence the results reported here. A short shaping time was used so as to achieve the best possible performance at high temperature (see Section 3.2).

The result of this investigation can be seen in Fig. 1, along with relative light outputs taken from [7] and [8]. In each case the light output has been normalised to the maximum to aid comparison. The results obtained here indicate that light output peaks at approximately 44 °C and 52 °C for CsI:Tl and CsI:Na respectively, as opposed to ∼80 °C as reported by Menefee et al. [7] or ∼30 °C as reported by Saint Gobain [8]. The result presented here is based on a single sample, and is not intended to refute the above values quoted by the manufacturer.

These measurements were performed by increasing the temperature of the chamber in stages and waiting until the temperature measured on the surface of the crystal became stable. It is possible that the wait time was not sufficient to allow the centre of the crystals to reach the measured temperature, in which case the temperatures reported in Fig. 1 would be artificially high. This effect could partially explain the discrepancy with the Saint Gobain data, however the Menefee et al. [7] result, indicating peak light output at ∼80 °C, is firmly refuted. Based on this result, (and bearing in mind that the absolute light output from CsI:Na is lower than that of CsI:Tl) we find no reason to favour CsI:Na over CsI:Tl for high temperature applications. Accordingly, unless otherwise stated, CsI:Tl is used throughout the remainder of this work.

Table 1
Characteristics of the SensL J-series and Hamamatsu S14160 SiPMs.

Characteristics	Hamamatsu	SensL
Technology	HWB (Hole Wire Bonding)	TSV (Through Silicon Via)
SiPM Type	S14160-6050HS	J-series
Effective area	6.0 × 6.0 mm^2	6.07 × 6.07 mm^2
Number of microcells	14,331	22,292
Breakdown voltage	37.0 V	24.5 V
Recommended overvoltage	2.7 V	2.5 V
Temperature coefficient	34 mV/°C	21.5 mV/°C
Gain	2.5 × 10^6	2.8 × 10^6
Crosstalk probability	7%	8%
Operating temperature	−40 to 85 °C	−40 to 85 °C

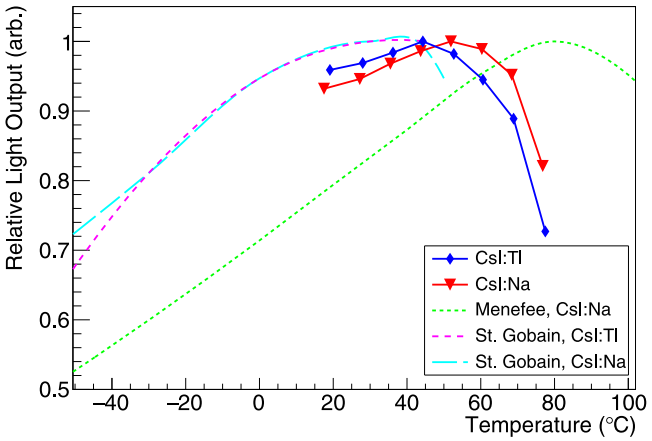

Fig. 1. Relative light output as a function of temperature for CsI:Tl and CsI:Na crystals, as measured in this work, and compared to that reported in Refs. [7] and [8].

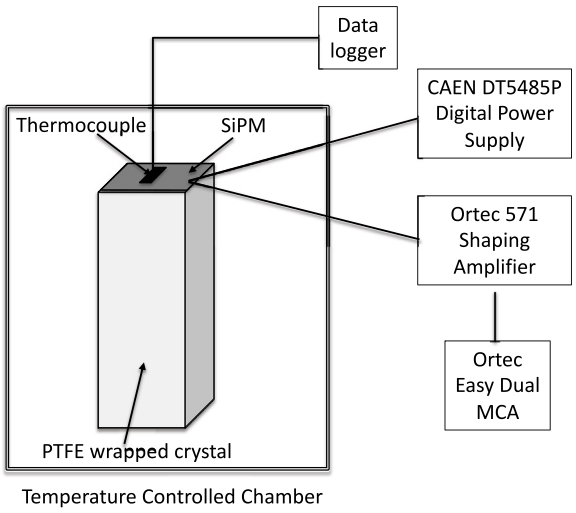

Fig. 2. Schematic of the experimental setup used throughout this work.

3.2. Energy resolution vs shaping time at room temperature and high temperature

In order to evaluate the performance of prototype detectors coupling CsI:Tl crystals to SiPMs, optimum operating parameters must be found, specifically bias and shaping time. The detector is ideally required to measure down to 60 keV so that it can be calibrated using a ^{241}Am source which is the standard procedure followed by Robertson Geologging, hence there is a risk of the noise floor increasing beyond this signal level. As such, signal-to-noise ratio is an important figure-of-merit. Accurate measurement of the noise level is not straightforward hence the FWHM of the 662 keV photopeak is used as a proxy for this, despite energy resolution not being of critical importance for this application. FWHM at 662 keV is calculated following a quadratic energy calibration based on fits to peaks from 121 to 1408 keV from a ^{152}Eu source, in order to correct for any non-linearity.

Prototype detector assemblies were produced coupling a 7 × 7 × 25 mm^3 CsI:Tl crystal to either a 6 × 6 mm^2 SensL J-series SiPM or a 6 × 6 mm^2 Hamamatsu S14160-6050HS series SiPM. The size of the crystal was chosen to match the dimensions of the SiPMs. In a real application a significantly larger, more efficient crystal would be required to measure the activities of interest. The scintillator crystals were wrapped with a minimum of eight layers of 0.2 mm PTFE tape and coupled to the photosensors using silicone-based optical grease (EJ-550). The nominal biases applied to the SensL J-series SiPM and Hamamatsu S14160-6050HS series SiPM were 29 V and 41 V, respectively. Detector readout was performed using an Ortec 571 shaping amplifier (with shaping times ranging from 0.5 to 10 μs) and a multi-channel analyser (Ortec EASY-MCA). Gamma-ray spectra were acquired using ^{137}Cs and ^{152}Eu sources to allow for energy calibration, linearity correction and measurement of energy resolution. Measurements were performed within a temperature controlled chamber, with a thermocouple placed in close proximity to the SiPM board to allow monitoring of the temperature. A schematic of this set up is shown in Fig. 2.

In Fig. 3, the linearity-corrected FWHM of the 662 keV photopeak is plotted as a function of shaping time. For all the measurements, the best resolution is observed at longer shaping times, which can be understood due to the long decay time of CsI:Tl. However, as can be seen from Fig. 4, when these measurements are repeated at high temperature (70 °C) this situation changes dramatically. This can be explained when we consider that the noise is the sum of series and parallel noise. The low temperature curves are consistent with a standard noise model with negligible current noise (the curve forms a shallow minimum, not reached within this range of shaping times). When the temperature is increased the dark-count rate increases, which can be treated as a source of current noise, thus is more significant for longer shaping times [10]. We should also note here that the decay time of CsI:Tl is known to reduce with increasing temperature [11], which may contribute to the shift to lower optimal shaping time at higher temperatures. Nevertheless, it is clear from Fig. 4 that shorter shaping times (2 μs or less) should be used at high temperature so as to minimise the contribution of this increased parallel noise. Accordingly, 2 μs shaping time is used as the optimum setting at high temperature with the standard electronics setup for the rest of this work.

3.3. Energy resolution vs bias at room temperature and high temperature

Figs. 5 and 6 show the bias optimisation of 6 × 6 mm^2 Hamamatsu S14160-6050HS and SensL J-series SiPMs respectively at room temperature and high temperature. The optimum operating voltages at room temperature are found to be 27.8 V and 41.0 V for SensL and Hamamatsu SiPMs: the corresponding ^{137}Cs and ^{152}Eu spectra can be seen in Figs. 7 and 8.

As was found for the shaping time, optimum operating conditions at high temperature differ significantly from those found at room

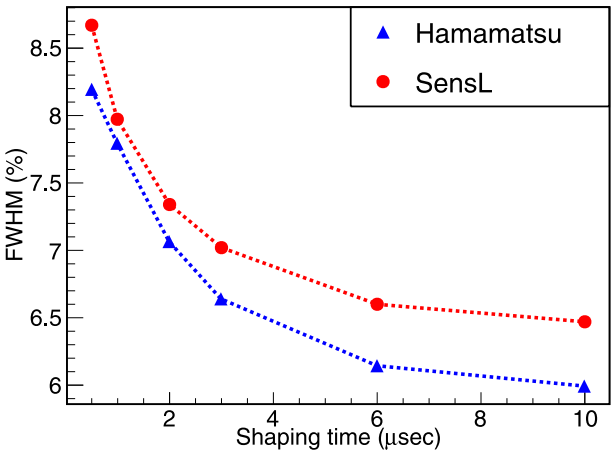

Fig. 3. Linearity corrected energy resolution (at 662 keV) as a function of shaping time for 6 × 6 mm^2 SensL J-series SiPM (red) and Hamamatsu S14160-6050HS (blue) each coupled to a 7 × 7 × 25 mm^3 CsI:Tl and operated at 29 V and 41 V respectively at room temperature.

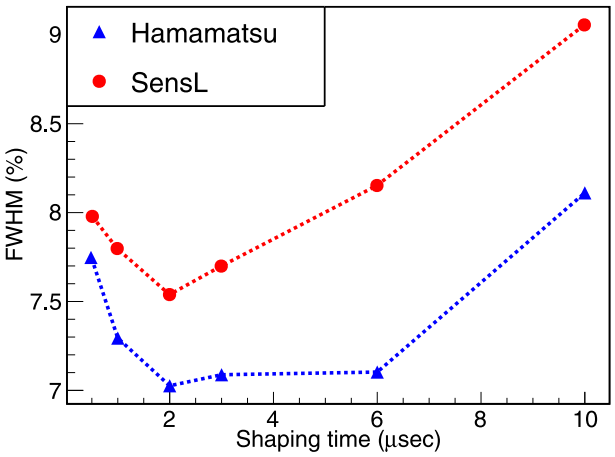

Fig. 4. Energy resolution as a function of shaping time for SensL J-series (red) and Hamamatsu S14160-6050HS (blue) SiPM at a bias voltage of 29 V and 41 V respectively, with temperature measured at 70 °C.

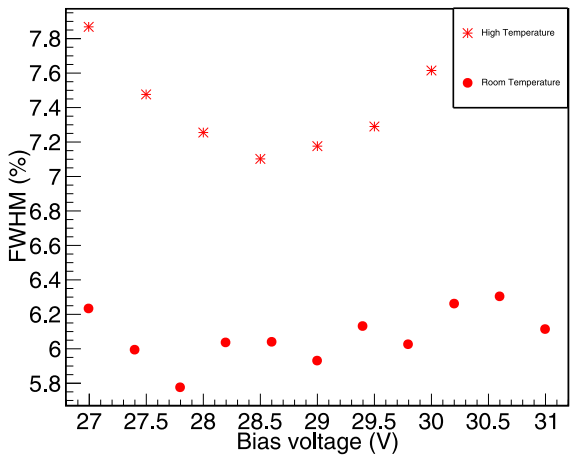

Fig. 5. Linearity corrected energy resolution (at 662 keV) as a function of bias voltage for 6 × 6 mm^2 SensL J-series SiPM coupled to a 7 × 7 × 25 mm^3 CsI:Tl, at room and high temperature (high temperature chamber set to 70 °C).

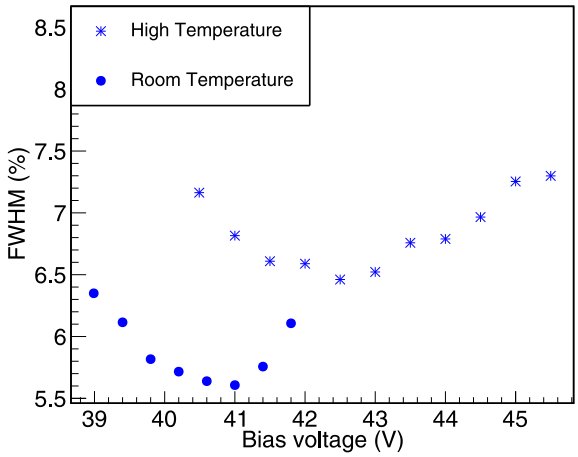

Fig. 6. Linearity corrected energy resolution (at 662 keV) as a function of bias voltage for 6 × 6 mm^2 Hamamatsu S14160-6050HS SiPM coupled to a 7 × 7 × 25 mm^3 CsI:Tl, at room and high temperature (high temperature chamber set to 70 °C).

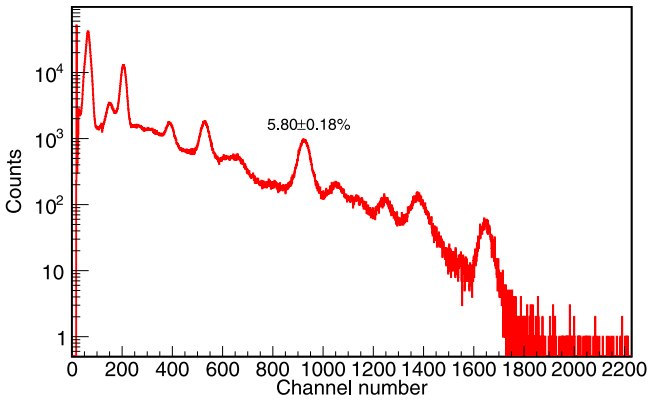

Fig. 7. Energy spectrum for ^{137}Cs and ^{152}Eu radioactive sources, measured with a 6 × 6 mm^2 SensL SiPM coupled to a 7 × 7 × 25 mm^3 CsI:Tl at room temperature using 10 μs shaping time and a bias voltage of 27.8 V. The FWHM of the 662 keV peak was 5.80(18)%.

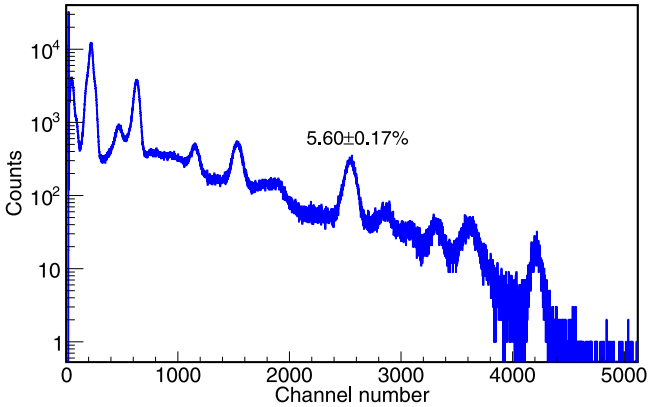

Fig. 8. Energy spectrum for ^{137}Cs and ^{152}Eu radioactive sources measured with a 6 × 6 mm^2 Hamamatsu SiPM coupled to a 7 × 7 × 25 mm^3 CsI:Tl at room temperature using 10 μs shaping time and a bias voltage of 41 V. The FWHM of the 662 keV peak was 5.60(17)%.

temperature. This can be explained via similar arguments to those used in Section 3.2. As the dark count rate (i.e. noise) increases exponentially with temperature, a bias voltage chosen to maximise the signal-to-noise ratio at room temperature will not be optimal at higher temperatures.

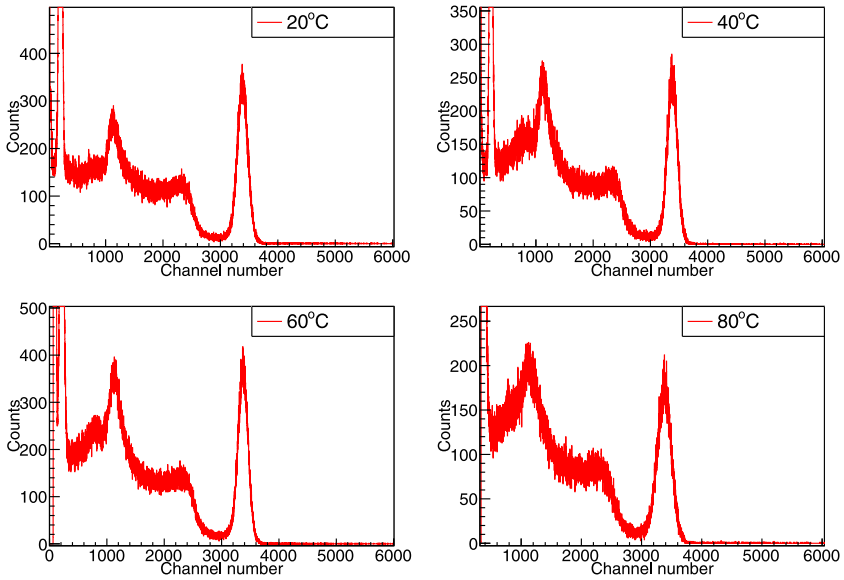

Fig. 9. Spectra obtained with the SensL SiPM at 20 °C (top left panel), 40 °C (top right panel), 60 °C (bottom left panel) and 80 °C (bottom right panel), manually adjusting the bias voltage to achieve the same 662 keV peak position (see text).

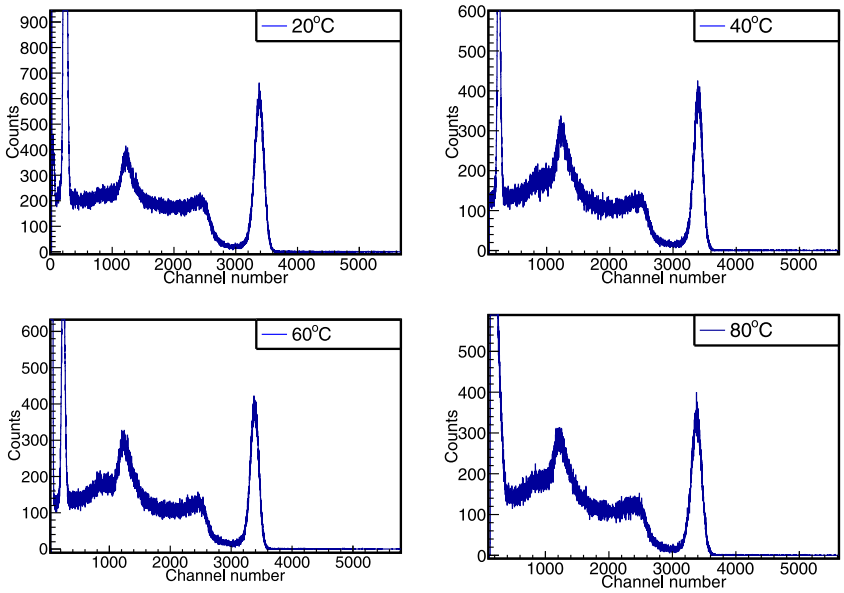

Fig. 10. Spectra obtained with the Hamamatsu SiPM at 20 °C (top left panel), 40 °C (top right panel), 60 °C (bottom left panel) and 80 °C (bottom right panel), manually adjusting the bias voltage to achieve the same 662 keV peak position (see text).

A summary of the results obtained in terms of energy resolution and the optimised detector parameters such as bias voltage and shaping time is presented in Table 2.

3.4. Temperature dependent gain stabilisation

In order to operate an SiPM over the large range of temperatures encountered during a well-logging measurement the bias must be adjusted to maintain a constant gain. This method is essential as going to higher temperatures will cause the breakdown voltage to increase beyond the nominal room temperature bias setting, leading to a complete loss of signal. Using the optimum settings found for our high temperature measurements, spectra were obtained at 80 °C with a ^{137}Cs source and the centroid of the 662 keV peak was noted. Spectra were then taken over a range of temperatures from 20 to 80 °C, at each point adjusting the bias to match the peak position at 80 °C. These spectra are shown in

Table 2
Optimum characteristics of the SiPMs tested.

Characteristics	6 × 6 mm^2 Ham.	6 × 6 mm^2 SensL
Optimum shaping time (22 °C)	10 μs	10 μs
Optimum shaping time (70 °C)	2 μs	2 μs
Optimum bias voltage (22 °C)	41.0 V	27.8 V
Optimum bias voltage (70 °C)	42.5 V	28.5 V
Breakdown voltage	38.2 V	25.3 V
Energy Resolution (662 keV) at (22 °C)	5.6%	5.8%
Energy Resolution (662 keV) at (70 °C)	6.5%	7.1%

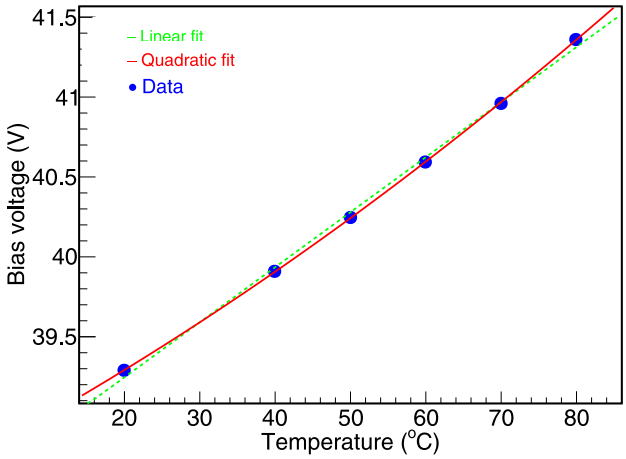

Fig. 11. Bias required to maintain a constant 662 keV peak position, as a function of temperature for Hamamatsu SiPM, along with linear and quadratic fits to the data.

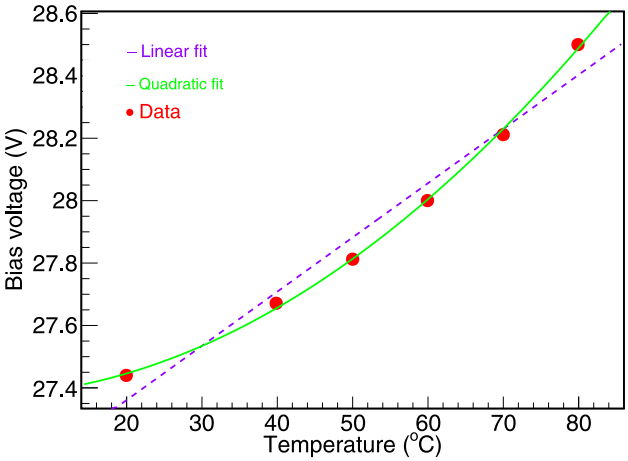

Fig. 12. Bias required to maintain a constant 662 keV peak position, as a function of temperature for SensL SiPM, along with linear and quadratic fits to the data.

Figs. 9 and 10. The increasing noise is evident on the left-hand-side of these spectra, with the 32 keV X-ray becoming obscured at the highest temperatures. In the case of the SensL SiPM at 80 °C, this noise is sufficient to conflict with the requirement to detect gamma rays below 100 keV.

The bias voltages required to maintain the 662 keV peak position are plotted as a function of temperature in Figs. 11 and 12 for the Hamamatsu and SensL SiPM respectively. From linear fits to these data we find average temperature compensation coefficients of 38.6 mV/°C and 27.4 mV/°C for the Hamamatsu and SensL SiPMs respectively, somewhat different to the values of 34 mV/°C and 21.5 mV/°C quoted in the respective data sheets as can be seen in Table 1 above. Furthermore, it is clear from the fits presented in Figs. 11 and 12 that a purely linear temperature compensation is not sufficient to stabilise the peak position over the large temperature range investigated here. Quadratic fits to these data were also performed and found to better reproduce the observed behaviour.

In Fig. 13, we present the energy resolution for the (linearity corrected) 662 keV peak, obtained from these spectra. Unsurprisingly, because the system has been optimised for the high temperature case, the resolution achieved at low temperatures is significantly worse than was achieved in Sections 3.2 and 3.3. Furthermore, although there is some variation of FWHM across the temperature range and, notably, the strong degradation of performance of the SensL SiPM at the highest

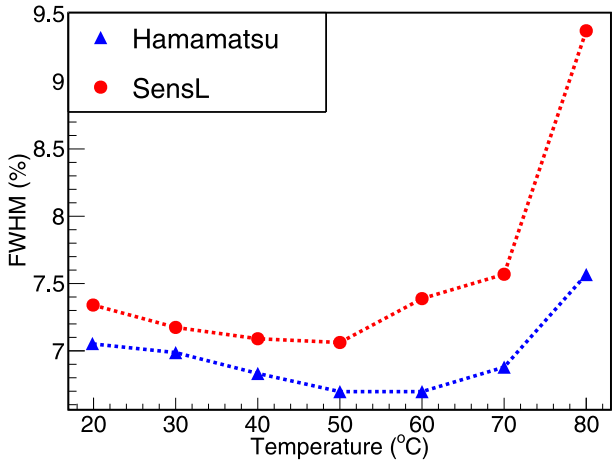

Fig. 13. Corrected energy resolution (at 662 keV) as a function of temperature for $7 \times 7 \times 25$ mm^3 CsI:Tl coupled to a 6×6 mm^2 Hamamatsu S14160-6050HS (blue) and SensL J series SiPMs (red) respectively, with varying bias voltage.

temperature considered, the variation is not large enough to conflict with the modest resolution requirements of this application.

4. Temperature compensation bias supply

In this section and in the continued project, our focus is to produce a bespoke, miniaturised temperature-compensated bias supply that would be appropriate to operate in the conditions experienced in borehole logging. This supply may well be different to what is available off the shelf. The device is controlled by an Arduino board, allowing it to be programmed to deliver the output voltage as any function of temperature. A circuit diagram of the device is shown in Fig. 14. The board interfaces with a daughter board which holds the SiPM array and a digital temperature sensing chip (ADT7310).

The performance of the power-supply module can be seen in Fig. 15, for a 2 × 2 SensL J-series array, characterised from 20 to 80 °C as described in Section 3.4. Using a quadratic temperature compensation function, the module successfully stabilises the gain maintaining the peak position throughout the energy range up to 70 °C. Beyond this temperature, the module was unable to deliver enough current to maintain the desired over-bias for this 2 × 2 array. A new version of the power-supply is being developed which will be able to deliver more current to allow gain stabilisation at higher temperature, as well as achieve higher bias voltages making it compatible with SiPMs from other manufacturers such as Hamamatsu.

5. Conclusion

Temperature sensitivity is a key parameter for photo-sensors which might be coupled to scintillators and used in borehole logging. We have demonstrated the suitability of modern SiPM technology to replace the current standard PMT based instruments, providing benefits such as reductions in form factor and low voltage requirements. The characterisation carried out provides an indication of the performance that can be expected from an SiPM based detector system for a well-logging application and it is seen to be comparable to that from a standard NaI:Tl plus PMT solution. While we have demonstrated that both the SensL and Hamamatsu SiPMs are suitable in such an application, the superior energy resolution, smaller temperature dependence, and crucially, the lower noise at high temperatures, would make the Hamamatsu SiPM the preferred choice for this challenging environment. Furthermore, we have presented results on the performance of a prototype temperature compensating SiPM power supply suitable for use in such an application.

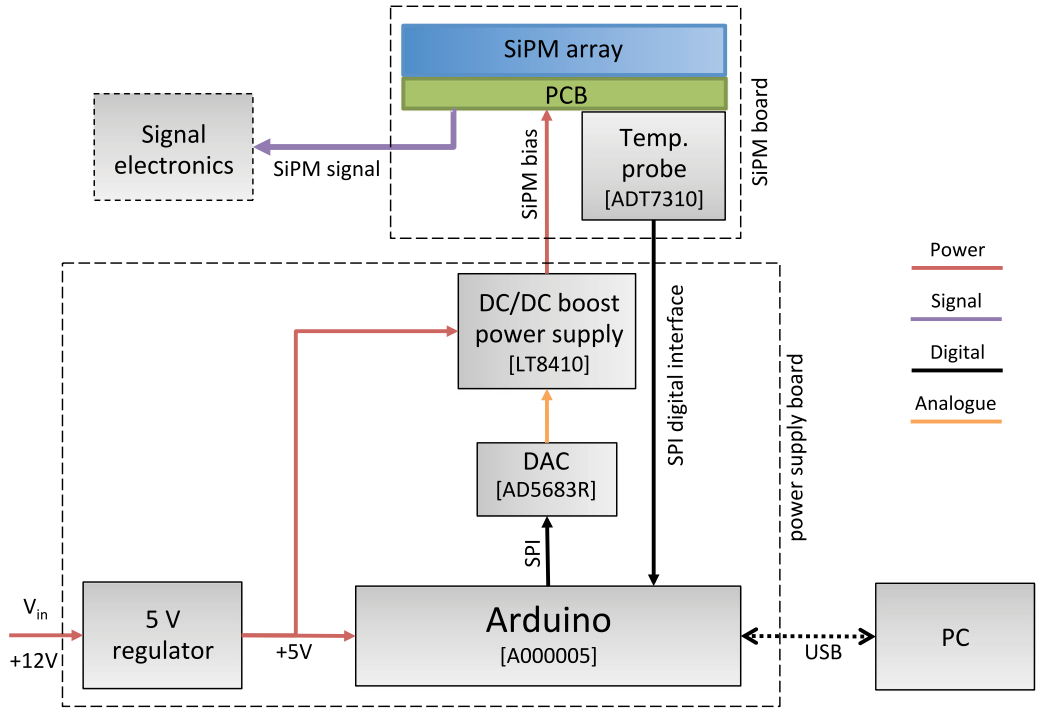

Fig. 14. Schematic diagram of the temperature compensation power supply. The PC connection is only required whilst programming the supply.

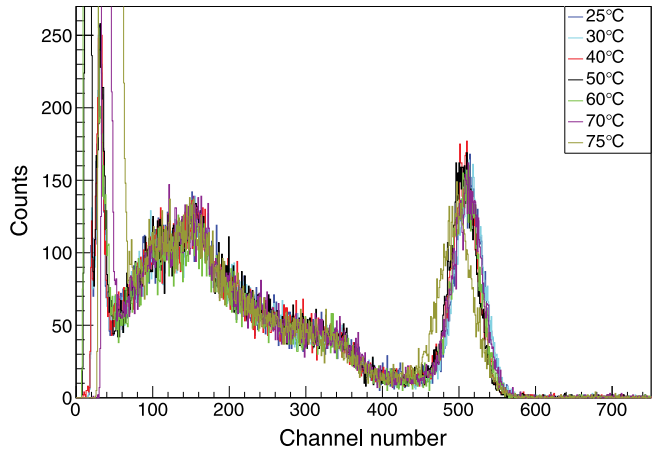

Fig. 15. ^{137}Cs spectra obtained with a range of temperatures, with a variable bias supplied by a temperature compensation power-supply module.

CRediT authorship contribution statement

A. Bala: Conceptualization, Methodology, Formal analysis, Validation, Software, Writing - original draft, Data curation, Validation. **J.R. Brown:** Software, Methodology, Writing - original draft, Writing - review & editing, Data curation, Validation. **D.G. Jenkins:** Conceptualization, Writing - review & editing, Supervision. **P. Joshi:** Resources, Supervision.

Declaration of competing interest

The authors declare that they have no known competing financial interests or personal relationships that could have appeared to influence the work reported in this paper.

Acknowledgements

Sincere gratitude to Petroleum Technology Development Fund (PTDF), Nigeria who fully funded this work. We acknowledge the support of Robertson Geologging, especially Paul Worthington who provided information on the context of gamma-ray detection in borehole logging. Aliyu Bala also acknowledges Robertson Geologging for hosting him at their headquarters for two weeks during 2018.

References

[1] M.G. Bisogni, A. Del Guerra, N. Belcari, Medical applications of silicon photomultipliers, Nucl. Instrum. Methods Phys. Res. A 926 (2019) 118–128.
[2] G. Llosá, SiPM-based compton cameras, Nucl. Instrum. Methods Phys. Res. 926 (2019) 148–152.
[3] H. Park, J.S. Lee, Highly multiplexed SiPM signal readout for brain-dedicated TOF-DOI PET detectors, Phys. Medica 68 (2019) 117–123.
[4] J. Jeon, H. Lee, J. Lee, Fabrication and testing of a 1024-pixel SiPM camera, Nucl. Instrum. Methods Phys. Res. 958 (2020) 162839.
[5] K. Shimazoe, M. Yoshino, Y. Ohshima, M. Uenomachi, K. Oogane, T. Orita, H. Takahashi, K. Kamada, A. Yoshikawa, M. Takahashi, Development of simultaneous PET and compton imaging using GAGG-SiPM based pixel detectors, Nucl. Instrum. Methods Phys. Res. A 954 (2020) 161499.
[6] M. Nakayama, N. Ando, J. Hirai, H. Nishimura, Scintillation activated by nanoparticle formation in CsI:Na thin films, J. Lumin. 108 (1-4) (2004) 359–363.
[7] J. Menefee, Y. Cho, C. Swinehart, Sodium activated cesium iodide as a gamma ray and charged particle detector, IEEE Trans. Nuclear Sci. 14 (1) (1967) 464–467.
[8] Gobain, Saint, CsI(Tl), CsI(Na) cesium iodide scintillation material, 2016, pp. 1–2.
[9] M. Grodzicka-Kobylka, T. Szczesniak, M. Moszynski, Comparison of sensl and hamamatsu 4x4 channel SiPM arrays in gamma spectrometry with scintillators, Nucl. Inst. Methods Phys. Res. A 856 (2017) 53–64.
[10] G.F. Knoll, Radiation Detection and Measurement, Wiley, New York, NY, 2010.
[11] J.D. Valentine, W.W. Moses, S.E. Derenzo, D.K. Wehe, G.F. Knoll, Temperature dependence of CsI(Tl) gamma-ray excited scintillation characteristics, Nucl. Instrum. Methods Phys. Res. A 325 (1–2) (1993) 147–157.

Appendix B:

Conference Paper

Monte Carlo Comparison of Alternatives to ^{3}He Thermal Neutron Detectors for Logging Applications

A. Bala, D. Jenkins, J. R. Brown, J. Bordes, P. Joshi and P. Worthington

***Abstract*—The survey of oil and gas often employs two radiation-based measurements in a rock formation: the electron density with γ-ray density tools; and the hydrogen content with neutron porosity tools. The former tools are composed of a γ-ray source and a γ-rays detector, such as NaI(Tl). The latter tools comprise a neutron source and a thermal neutron (25 meV) detector, such as ^{3}He tube. However, γ-ray density and neutron porosity tools must be used conjointly. Additionally, the demand for neutron detection technology is increasing while the supply of ^{3}He gas is extremely scarce. These issues have led to the development of alternative neutron detection technology based on ^{10}B and ^{6}Li. Here, the first aim was to review detectors belonging to ^{10}B and ^{6}Li families. The second aim was to compare ^{3}He tube and some ^{10}B and ^{6}Li detectors selected from the review. Their counting rates were calculated with Geant4 Monte Carlo simulations. In the tested configurations, it was shown that both ^{10}B and ^{6}Li families present counting rates similar to ^{3}He tubes. Furthermore, ^{6}Li detectors are capable of measuring both electron density and hydrogen content, eliminating the need for two separate tools.**

I. Introduction

THE oil and gas industries use nuclear logging techniques to search for the presence of hydrocarbons in a geological formation. This process necessitates the measurement of both the electron density (correlated to the rock density) and the hydrogen content (from hydrocarbons and other substance like water). The electron density is assessed with γ-ray density tools composed of a radioactive source and a γ-ray detector, such as NaI(Tl). The hydrogen content is evaluated by means of neutron porosity tools, that comprise a neutron source and a thermal neutron (25 meV) detector, such as a ^{3}He tube. However, none of these detectors are able to measure both the electron density and the hydrogen content.

As ^{3}He tubes have high efficiency for thermal neutrons and tolerance to γ-ray radiation, it is the conventional neutron detector used in oil and gas industries, and in other fields (e.g. homeland security, nuclear experiments). However, there is an increasing demand for neutron detection technology as well as a shortage of ^{3}He gas [1]. Given the high cost of ^{3}He tubes, a variety of alternative thermal neutron detectors based on ^{10}B or ^{6}Li were developed. Some of them have the added advantage of detecting γ-rays, allowing the measurement of the electron density.

In this work, we review ^{3}He based thermal neutron detectors along with alternative ^{10}B and ^{6}Li based technologies. In order to compare the capability of these different types of detectors, Monte Carlo simulations were carried out to measure the counting rates of ^{3}He tubes and three of the reviewed alternatives, namely ^{10}B-coated straws, Eu:LiCAF and ^{6}Li-loaded glass neutron detectors.

Manuscript received December 16, 2019. This work was supported in full by the Federal Republic of Nigeria through Petroleum Technology Development Fund (PTDF).

A. Bala is with the Department of Physics, University of York, York, YO10 4DD, United Kingdom, and with the Department of Physics, Usmanu Danfodiyo University, Sokoto, P.M.B 2346, Sokoto-Nigeria (emails: aliyu.bala@york.ac.uk, aliyu.bala@udusok.edu.ng).

D. Jenkins, J.R. Brown, J. Bordes, P. Joshi are with the Department of Physics, University of York, York, YO10 4DD, United Kingdom.

P. Worthington is with the Robertson Geologging Company, York Road, Deganwy, Conwy, LL31 9PX, United Kingdom.

II. Review of Some Alternative Thermal Neutron Detector Technologies

Boron and lithium are the two most widely used alternative neutron converting materials for thermal neutron detection. A description of some of these alternatives is given below. Their advantages and disadvantages are compared to one another.

A. ^{3}He Based Neutron Detectors

The detector utilizes the ^{3}He(n,p)^{3}H reaction which has a very high cross section at thermal neutron energies. ^{3}He proportional counters exploit the ^{3}He(n,p)^{3}H reaction to detect thermal neutrons, with a Q value of 0.764 MeV which is deposited within the gas in the form of the kinetic energies of the two decay products:

$$^3\mathrm{He} + \mathrm{n} \rightarrow {}^3\mathrm{H} + \mathrm{p} \tag{1}$$

The thermal neutron absorption cross section of ^{3}He is around 5327 barn. The standard ^{3}He tube is filled to 3.6 atm. From a safety point of view, ^{3}He gas is not toxic and non-flammable.

B. ^{10}B Based Neutron Detectors

^{10}B(n,α)^{7}Li is one of the most common reactions used in the conversion of slow neutrons into charged particles which can be detected directly. This reaction leaves ^{7}Li in either its ground state or an excited state, with Q values of 2.79 MeV and 2.30 MeV, respectively. These are illustrated in equations 2 and 3:

$$^{10}\mathrm{B} + \mathrm{n} \rightarrow {}^7\mathrm{Li} + {}^4\mathrm{He} \quad (ground\ state) \tag{2}$$

$$^{10}\mathrm{B} + \mathrm{n} \rightarrow {}^7\mathrm{Li}^* + {}^4\mathrm{He} \quad (excited\ state) \tag{3}$$

Below is a description of some of these ^{10}B based alternative technologies:

978-1-7281-4164-0/19/$31.00 ©2019 IEEE

1) Boron trifluoride (BF_3) filled proportional counters: This technology is a direct replacement of the conventional ^{3}He tube [2]. The hazardous nature of the gas combined with the need for high pressure tubes pose a great disadvantage compared to the conventional detector. Despite having lower thermal neutron absorption cross section (3840 barn) as compared to ^{3}He, these detectors offer good neutron/γ separation with very high count rate capabilities. It was reported that two BF_3 tubes filled to ≈ 1 atm each can perform better than one ^{3}He tube filled to 3 atm [2].

2) ^{10}B lined proportional counters: This is also a direct replacement of ^{3}He. Unlike BF_3 filled proportional counters, the safety-related limitation on high pressure tubes has been reduced. In this type of technology, ^{10}B is lined on the inner wall of the counter [3][4], thereby allowing to use a less or non hazardous fill gas. They are very similar to the BF_3 tubes in design. One limiting factor affecting this design is the inner surface area and the accurate determination of the ^{10}B thickness as well as the special requirement for a specific sputtering technology.

3) ^{10}B lined high surface area detectors: The surface area limitation can be overcome by using a modified geometry. One such geometry employs multiple coated straw tubes which can be made from cheap materials like aluminium. A ^{10}B-coated straws detector was reported to have better distribution of neutron converting material, improved γ-ray rejection and faster electronic signals. Furthermore, it provides safety advantages such as no requirement for pressurization and no toxicity or flammability[3].

This technology will be useful especially for applications that only require count rates. The detector counts were scaled to the size of a standard ^{252}Cf source that emits 2×10^4 neutrons per second. It was found to have 29 cps and 30 cps for a large and a small ^{252}Cf source with 85 straws respectively, the corresponding performance of ^{3}He based radiation portal monitor deployed by the US homeland security is at least 20 cps for design with single tube and 32 for design with two tubes. In a more recent experimental study of ^{10}B-coated straws with a neutron source for the China Spallation Neutron Source (CSNS) commissioned in 2018 [4], the detector was tested at IHEP, and the measured spectrum shows a clear distinction between the neutron and γ events.

4) ^{10}B doped scintillators: In this type of detector, a conventional plastic scintillator is coated with a ^{10}B containing compound. Plastic scintillators have a very fast decay time which allows high counting rates. These devices are economical to produce in large numbers or sizes. These detectors are suitable for fast neutron detection applications. The use of moderating material can also make them suitable for thermal neutron detection.

A work to test the efficiency of ^{10}B-lined NaI detectors [5] shows a good sensitivity to neutrons. In a more recent work, this technology showed a good sensitivity to changes in neutron flux [6]. The same work explains an added advantage of this technology, which is the ability to provide information about the γ-rays from the samples as well as from any nearby material emitting γ-rays. This is good news for applications needing to have a detector that is sensitive to both neutrons and γ-rays.

III. ^{6}Li Based Neutron Detectors

Neutron detection using ^{6}Li as a converting material is based on the following reaction:

$$^6\mathrm{Li} + \mathrm{n} \rightarrow {}^3\mathrm{H} + {}^4\mathrm{He} \tag{4}$$

with a Q value of 4.78 MeV. ^{6}Li has an absorption cross section of 940 barn. It has 1/v dependence except at the resonance region between around 0.15 MeV and 0.3 MeV. At this region, the cross section of ^{6}Li is quite high. Below 0.1 MeV, the reaction probability for ^{6}Li becomes low. This effect is compensated though with its high Q value. Just like ^{3}He tube, the decay products from this reaction are easier to detect as only one decay channel is possible.

Below are some ^{6}Li based alternative neutron detectors:

1) ^{6}Li foil scintillator sandwich: In this type of detection method, multiple layers of reactive film together with light guides are stacked together in a sandwich pattern. A work that adopted this type of technology reported an intrinsic efficiency per layer between approximately 20% and 35% [7]. The detector also shows high efficiency compared to ^{3}He and up to about three times shorter die-away time.

Another form of this alternative is based on commercial solid state silicon detectors coupled with thin neutron converter layers of ^{6}LiF deposited onto carbon fiber substrates. In a recent work [8], ^{6}LiF was obtained as a powder and then evaporated under vacuum into substrates forming layers of different thicknesses. Measurements from such a detector showed a reasonable detection efficiency of $\approx 5.2\%$. Similar technology was adopted by [9], the detection efficiency for this detector is around 8%. This efficiency, the γ rejection performance and the rather low cost as compared to ^{3}He tubes makes these detectors quite interesting for several applications.

2) ^{6}Li-loaded glass neutron detectors: ^{6}Li has also been incorporated into glass matrix to measure thermal neutrons. This method has comparable sensitivity to ^{3}He. Its short die-away time makes it suitable for high count rate applications. A ^{6}Li glass based composite neutron detector was fabricated and characterized to have a good neutron/γ event separation when exposed to a ^{252}Cf source [10]. In another work [11], a similar detector was fabricated which utilizes a combination of pulse height and pulse shape discrimination to achieve high rejection of γ-rays. The results from this detector also shows an intrinsic neutron efficiency of 0.005% for unmoderated spontaneous fission neutrons from ^{252}Cf.

3) CLYC Scintillators: This type of detection technology allows for both neutron and γ-rays detection [12][13]. It relies on the fact neutrons and γ-rays produce light with different time profiles making it easier for electron pulse shape discrimination. CLYC samples enriched with ^{6}Li have over two times the cross section of ^{3}He. This property makes it suitable for two in one applications. The emission in this type of technology consist of core-valence luminescence and cerium emission. In a work to find some selected properties of elpasolites, this detector was found to have an energy resolution of 3.9% for 0.662 MeV γ-rays [14].

4) CLLB Scintillators: This is also another class of elpasolite that also permit dual measurement with improved energy resolution [15][16]. The only difference it has is emission process, which unlike CLYC, doesn't exhibit core-valence luminescence, which could be due to its low band gap. Its light yield has been measured to be as high as 6×10^4 photons/MeV. This leads to an excellent 2.9% energy resolution for 0.662 MeV γ-rays [14]. In terms of detector geometry, this is almost if not smaller than ^{3}He tube.

5) LiCAF Scintillator: Lithium calcium aluminium flouride (LiCAF) scintillator is a new form of ^{6}Li-based thermal neutron detector. It is available in two common known dopants, Ce:LiCAF and Eu:LiCAF. Depending on the area of application, both dopants have their pros and cons. Overall, all of them are known to have great neutron detection efficiency. Ce:LiCAF scintillator has a very fast decay time (40 ns) as compared to Eu:LiCAF scintillator (above 1000 ns). Ce:LiCAF has low effective Z of 15, which also makes it less sensitive to γ-rays [17][18]. On the other hand, the luminescent wavelength of Eu:LiCAF as compared to Ce:LiCAF is 360-390 nm and 280-320 nm respectively. While Ce:LiCAF is pulse shape discrimination compatible, Eu:LiCAF has high light yield. Both scintillators are transparent and non-hygroscopic. In either dopant, the ratio of the scintillation efficiency for alphas to that for electrons is low. They therefore also suffer from γ-rays interference. One therefore has to be careful in choosing the size of the scintillator. In a recent experiment, Eu:LiCAF/rubber [18] was evaluated and found to have excellent discrimination ability.

The Monte Carlo comparative study focused on ^{3}He tube, ^{10}B-coated straw and Eu:LiCAF and ^{6}Li-loaded glass neutron detectors.

IV. Detectors Characterization with Monte Carlo Simulations

A. General Settings

Detector counting efficiencies were calculated with Monte Carlo simulation toolkit Geant4 10.5. This code was verified for the transport of neutrons from GeV down to thermal energies [19]. To describe neutrons and γ-rays interactions, QGSP_BERT_HP_EMZ physics model were adopted. QGSP_BERT_HP are considered as the reference for neutrons below 20 MeV [19]. The extension EMZ allows simulation of electromagnetic processes.

B. Detector Design

For a valid comparison of ^{3}He, ^{10}B and ^{6}Li based detectors, a standard logging tool was simulated, as shown in figure 1. For each tool, two detector volumes were defined, referred to as *near* and *far* detectors. The near detector measured 2.54 cm in diameter and 12.62 cm in length and had its center placed at 40 cm from the Am/Be neutron source. The far neutron detector center was placed at 60 cm from the source and measured 2.54 cm in diameter and 18.52 cm in length. Simulations were performed for four detector types 12.62 cm in length,other detector descriptions are given in table I:

TABLE I
Detectors geometry description and materials

	^{3}He tube	^{10}B-coated straw	^{6}Li-loaded glass	Eu:LiCAF
Diameter (cm)	2.54	2.54	2.54	2.54
Tube thickness (cm)	2.54	0.1	2.54	2.54
Converting material	^{3}He	B	Li	Li
Enrichment	100%	78% B 95% ^{10}B	6.6% Li 95% ^{6}Li	6.6% Li 95% ^{6}Li

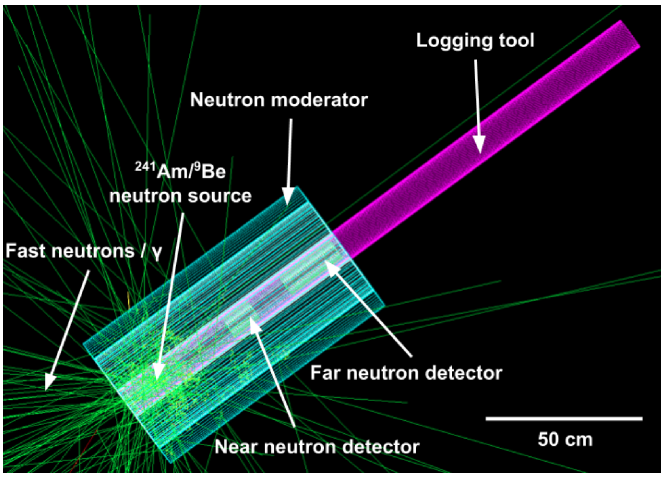

Fig. 1. Visulalization of the simulation of a neutron logging tool comprising an Am/Be neutron source and two ^{3}He tubes, labeled near and far neutron detectors, in a cylindrical moderator.

C. Neutron Source

An Am/Be neutron is reported to emit 2.2×10^6 neutrons per second per curie [20]. Each simulation considered the emission of 5×10^6 neutrons, corresponding to a 92 GBq AmBe source. This neutrons were emitted isotropically into the calibration block. The thermalized neutrons eventually backscattered into one of the the detectors.

V. Results and Discussion

A. Detectors Thermal Energy Count Rates

To understand the detectors response to hydrogen rich materials, detectors were placed in a block of a high-density polyethylene material. This material is commonly used as a calibration block.

Figure 2 shows the count rates for the near neutron detectors for ^{3}He tube (green line), ^{6}Li-loaded glass neutron detectors (black line), Eu:LiCAF (magenta line), and ^{10}B-coated straw tube (blue line). A well defined neutron induced peak is clearly visible in all four detectors, and count rates are comparable to the ^{3}He tube.

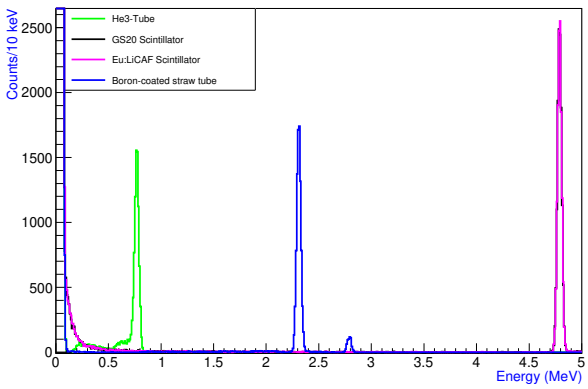

Fig. 2. Count rates for ^{3}He tube (green), Eu:LiCAF (pink), ^{6}Li-loaded glass neutron detectors (referred to as GS20) (black) and ^{10}B-coated straw tube (blue). Note that, due to having the same reaction mechanism, the GS20 data is partially obscured by the Eu:LiCAF.

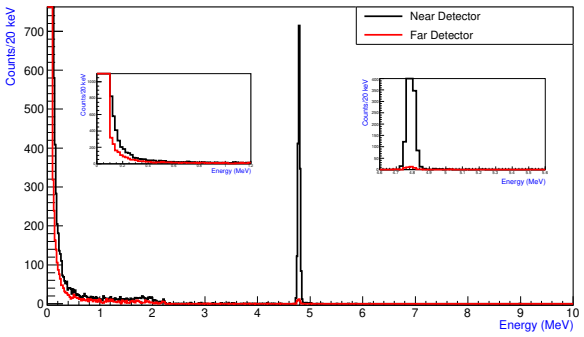

Fig. 3. Count rates for Eu:LiCAF neutron detector with a polyethylene moderator for the near neutron detector (red line) and the far neutron detector (black line).

B. Eu:LiCAF Detector in Hydrogen Rich and Non-Hydrogen Moderators

In a first step, to investigate the response of Eu:LiCAF detector in hydrogen rich materials, simulation were proceed with a polyethylene moderator. In a second step, to study its response in non-hydrogen material, simulation considered a sandstone moderator.

Figure 3 presents the count rate for the near (black line) and far (red line) neutron detectors in polyethylene. The energy peak observed corresponds to the reaction Q value (4.78 MeV) of ^{6}Li(n,α)^{3}H reaction. Thus it is only due to thermal neutrons contribution.

Figure 4 presents the count rate for the near (black line) and far (red line) neutron detectors in sandstone. The right inset shows a second peak around 5 MeV that was not predicted by the simulation in polyethylene. This means that more energetic neutrons were detected. This difference comes from non-hydrogenous materials not fully moderating the fast neutrons. Thus, more energetic neutrons (epithermal neutrons) reached the detectors. However, it is yet to be established if this 5 MeV energy peak could be resolved in real measurement.

^{3}He tube is mainly sensitive to thermal neutrons, therefore will not provide much information in rock formation with less hydrogen content. The ^{6}Li based detector on the other hand are sensitive to these epithermal neutrons and therefore information can still be obtained even in logging formation with less hydrogen content. Figure 4 shows this contribution by epithermal neutrons.

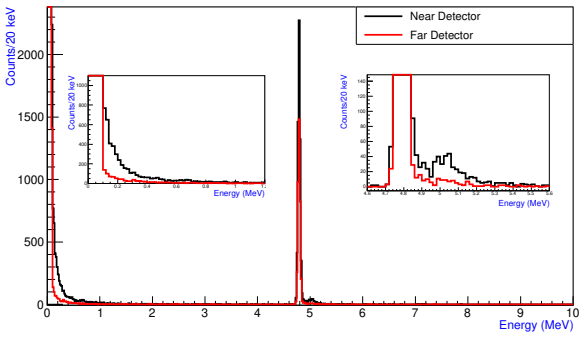

Fig. 4. Count rates for Eu:LiCAF neutron detector with a sandstone moderator for the near neutron detector (red line) and the far neutron detector (black line).

VI. γ-Rays Measurements

Compared to^{3}He tubes, one great advantage of ^{6}Li based detectors is their sensitivity to γ-rays. When the logging environment is bombarded with fast neutrons, they lose their energy to form a cloud of thermal and epithermal neutrons. These neutrons are eventually absorbed by the nuclei of different elements present in the logging formation and around the logging tool. These nuclei are then in a excited state. Upon de-excitation, they release γ-rays with specific energies. Characteristic γ-rays are also released when energetic neutrons, normally greater than 1 MeV undergo inelastic scattering with the atomic nucleus in the formation.

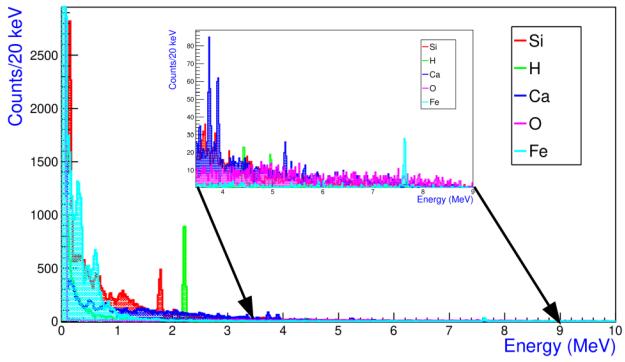

Fig. 5. Captured and inelastic γ-ray energy spectra from different elements surrounding the ^{6}Li-loaded glass detectors.

Simulations were performed with silicon, hydrogen, calcium, oxygen and iron as the moderating material, and the captured and inelastic spectra recorded. The energy spectra in figure 5 show key characteristic peaks corresponding to each element.

Eu:LiCAF was used to measure the captured γ-rays spectra in the presence of polyethylene material which is rich in hydrogen and carbon. Characteristic γ-rays like the 2.22 MeV emitted by hydrogen after absorbing a thermal neutron and the 1.781 MeV γ-rays from the de-excitation of ^{28}Si are both very obvious as can be seen from figures 5 and 6. The 7.7 MeV γ-ray peak and the 0.511 MeV pair production from iron in the logging tool are also seen clearly.

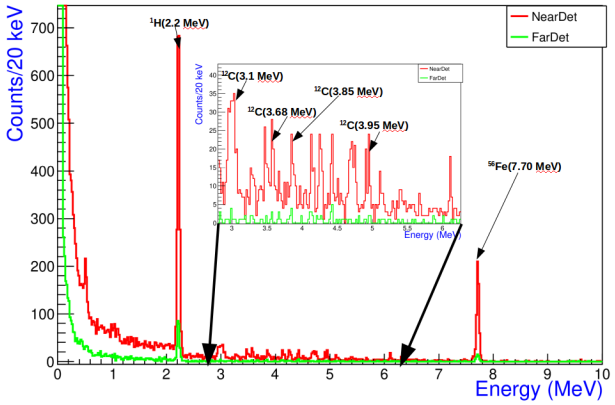

Fig. 6. Captured γ-rays energy spectra from the moderating material (high density polyethylene) around the detector and the logging tool (iron).

VII. Conclusion And Future Work

The capability demonstrated by ^{6}Li based neutron detectors to be measure both neutrons and γ-rays could be useful in nucleqr logging application. This has the potential to eliminate the need for using both a neutron porosity tool and a density logging. A single tool can then be built with neutron/γ discrimination capability in real time measurements.

The big challenge now will be to identify each characteristic γ-rays peak out of the γ-rays discriminated from the neutrons. If this can be achieved, logging cost and time will be reduced significantly.

Acknowledgment

Special gratitude to Robertson Geologging who provided some useful information on the performance of a typical logging tool, this information guided our simulation a lot.

References

[1] Richard T. Kouzes et al. Progress in alternative neutron detection to address the helium-3 shortage. *Nuclear Instruments and Methods in Physics Research Section A: Accelerators, Spectrometers, Detectors and Associated Equipment*, 784:172 – 175, 2015. Symposium on Radiation Measurements and Applications 2014 (SORMA XV).

[2] Richard T. Kouzes et al. Neutron detection alternatives to 3he for national security applications. *Nuclear Instruments and Methods in Physics Research Section A: Accelerators, Spectrometers, Detectors and Associated Equipment*, 623(3):1035 – 1045, 2010.

[3] Jeffrey L. Lacy et al. Boron-coated straws as a replacement for 3he-based neutron detectors. *Nuclear Instruments and Methods in Physics Research Section A: Accelerators, Spectrometers, Detectors and Associated Equipment*, 652(1):359 – 363, 2011. Symposium on Radiation Measurements and Applications (SORMA) XII 2010.

[4] Zhaoyang Xie et al. Experimental study of boron-coated straws with a neutron source. *Nuclear Instruments and Methods in Physics Research Section A: Accelerators, Spectrometers, Detectors and Associated Equipment*, 888:235 – 239, 2018.

[5] Walid A. Metwally. Existing nai detectors; an efficient alternative to he-3 detectors. *Nuclear Instruments and Methods in Physics Research Section B: Beam Interactions with Materials and Atoms*, 338:48 – 51, 2014.

[6] Walid A. Metwally and Amira G. Emam. Experimental validation and testing of a nai boron-lined neutron detector. *Nuclear Instruments and Methods in Physics Research Section B: Beam Interactions with Materials and Atoms*, 422:7 – 11, 2018.

[7] K.D. Ianakiev et al. 6li foil scintillation sandwich thermal neutron detector. *Nuclear Instruments and Methods in Physics Research Section A: Accelerators, Spectrometers, Detectors and Associated Equipment*, 652(1):417 – 420, 2011. Symposium on Radiation Measurements and Applications (SORMA) XII 2010.

[8] A. Pappalardo et al. Characterization of the silicon+6lif thermal neutron detection technique. *Nuclear Instruments and Methods in Physics Research Section A: Accelerators, Spectrometers, Detectors and Associated Equipment*, 810:6 – 13, 2016.

[9] Paolo Finocchiaro et al. Absolute efficiency calibration of 6lif-based solid state thermal neutron detectors. *Nuclear Instruments and Methods in Physics Research Section A: Accelerators, Spectrometers, Detectors and Associated Equipment*, 885:86 – 90, 2018.

[10] G.C. Rich et al. Fabrication and characterization of a lithium-glass-based composite neutron detector. *Nuclear Instruments and Methods in Physics Research Section A: Accelerators, Spectrometers, Detectors and Associated Equipment*, 794:15 – 24, 2015.

[11] M. Mayer et al. Development and characterization of a neutron detector based on a lithium glass–polymer composite. *Nuclear Instruments and Methods in Physics Research Section A: Accelerators, Spectrometers, Detectors and Associated Equipment*, 785:117 – 122, 2015.

[12] M.M. Bourne et al. Characterization of the clyc detector for neutron and photon detection. *Nuclear Instruments and Methods in Physics Research Section A: Accelerators, Spectrometers, Detectors and Associated Equipment*, 736:124 – 127, 2014.

[13] A Mentana et al. Measurement of fast neutron detection efficiency with 6Li and 7Li enriched CLYC scintillators. *Journal of Physics: Conference Series*, 763:012006, 2016.

[14] Urmila Shirwadkar. Scintillation properties of cs2lilabr6 (cllb) crystals with varying ce3+ concentration. *Nuclear Instruments and Methods in Physics Research Section A: Accelerators, Spectrometers, Detectors and Associated Equipment*, 652(1):268 – 270, 2011. Symposium on Radiation Measurements and Applications (SORMA) XII 2010.

[15] Richard S. et al. Characterization of the internal background for thermal and fast neutron detection with cllb. *Nuclear Instruments and Methods in Physics Research*, 838:147 – 153, 2016.

[16] K.E. Mesick et al. Pulse-shape discrimination and energy quenching of alpha particles in cs2lilabr6:ce3+. *Nuclear Instruments and Methods in Physics Research Section A: Accelerators, Spectrometers, Detectors and Associated Equipment*, 841:139 – 143, 2017.

[17] T. Fujiwara et al. Study on ce:licaf scintillator for 3he alternative detector. *Neutron News*, 23(4):31–34, 2012.

[18] Michael A. Ford et al. Evaluation of eu:licaf for neutron detection utilizing sipms and portable electronics. *Nuclear Instruments and Methods in Physics Research Section A: Accelerators, Spectrometers, Detectors and Associated Equipment*, 908:110 – 116, 2018.

[19] B.M. van der Ende et al. Use of geant4 vs. mcnpx for the characterization of a boron-lined neutron detector. *Nuclear Instruments and Methods in Physics Research Section A: Accelerators, Spectrometers, Detectors and Associated Equipment*, 820:40 – 47, 2016.

[20] H Basiri and H Tavakoli-Anbaran. Investigation of some possible changes in am-be neutron source configuration in order to increase the thermal neutron flux using monte carlo code. *Journal of Physics: Conference Series*, 956:012010, jan 2018.